ELECTRONIC STRUCTURE AND BONDING IN ENERGY STORAGE MATERIALS

Thesis by

Shu Miao

In Partial Fulfillment of the Requirements for the

degree of

Doctor of Philosophy

CALIFORNIA INSTITUTE OF TECHNOLOGY

Pasadena, California

2007

(Defended January 30, 2007)

Acknowledgements

I am especially grateful to my advisor, Prof. Brent Fultz, for his guidance, understanding, and insight over the years.

I thank Dr. Channing Ahn for a lot of enlightening conversations.

I am grateful to Prof. Rachid Yazami for his ceaseless encouragement and for sharing his vast knowledge of electrochemical systems.

I would like to thank Prof. Peter Rez and Michael Kocher at ASU for their help with the computational physics of electronic structure.

Thank Dr. Yasunori Ozawa, Dr. Olivier Delaire, Dr. Yvan Reynier and Dr. Jason Graetz for very helpful discussions.

Thank Joanna Dodd for help with sample preparation and XRD measurements.

Thank Carol Garland for help in using the transmission electron microscope.

Thank Dr. Jiao Lin and Max Kresch for their help with the Linux cluster.

Thank my pure-French team of officemates who accompanied me through these years in the small office.

Thank Pamela Albertson and Tara Scott, our cheerful secretaries, for their countless helps in administrative trivia.

Thank Zhipu Jin, Wuan Luo, Lixiu Tian, Xinwei Yu, Chengzhong Zhang, Wei Liu, Jiantao Wang and Jian Wu for helping me to explore the life in California when I arrived at Caltech four years ago.

Thank the grand shopping team including George Ouyang, Xinkai Wu, Guodong Wang *et al.*, which brought a lot of convenience and fun to my life.

Thank Hsin-Ying Chiu for so many cares and helps as being a great neighbor as well as a friend, and special thanks goes to her excellent work in decorating the PowerPoint file for my defense presentation.

Thank everyone who has extended me their friendship, Mo Li, Changlin Pang, Hao Jiang, Yong Hao, Xin Guo, Yu Liu, Xiao Lu, Gang Duan, Bo Li, Jian Lu, Chih-Kai

Ko, Xiaojie Gao, Tingwei Mu, Ao Tang, I-Ren Lee, Bolin Lin, Tao Liu, Ling Shi, Liang-Meng Lee (Singapore), Peigen Cao, etc.

Special thanks to all members of the CaltechC dance team, Ru He, Yajuan Wang, Lu Tian, Lin Han, Xin-An Xiu, Fei Wang, Yi Shen, Yan Chen, Xi Yu, Haiying Qi, Ling Zheng, Fan Yang, Ying Wang, Jing Yang. Thanks these pretty ladies for upholding me as the leader of the team to pursue a success in the art of dancing besides the scientific researches at Caltech.

Thank my cousin Pengzi Miao and his family for their hospitality every time I visited them.

Thank Ying Guo, Tong Liu and Fei Fang for their oversea cares for me over these years.

Thank my friends Bing Dai, Wenfeng Liu, Pu Wang, Xiangyang Wang, Peng Xue, Haijiao Li, Ruikai Mai, Lei Guo for taking care of my parents in my hometown.

I am eternally grateful to my family for their unceasing support. It goes without saying that none of this would have been possible without them.

Finally, thank her inly.

Abstract

Previous work at Caltech and MIT discovered that oxygen plays an important role in the charge compensation mechanism during lithium insertion and extraction in the layered $LiCoO_2$ cathode material. The Co-O bond becomes more covalent during delithiation because O donates electrons. Nevertheless, some of those groups proposed that the situations were different for $LiNi_{0.5}Mn_{0.5}O_2$ and $LiNi_{1/3}Mn_{1/3}Co_{1/3}O_2$ than for $LiCoO_2$, though all have same layered cyrstal structure. The Ni^{2+}/Ni^{4+} redox couple was proposed to dominate the charge compensation during lithium insertion and extraction.

We investigated this topic by employing electron energy loss spectrometry (EELS) measurements with computational support. Our results indicate that most of the compensation for charge during the removal of Li ions from $Li_xNi_{1/3}Mn_{1/3}Co_{1/3}O_2$ and $Li_xNi_{0.5}Mn_{0.5}O_2$ occurs at hybridized 2p-like levels with local weight near oxygen atoms, much as is the case in Li_xCoO_2. All experimental and computational results are inconsistent with the hypothesis of a Ni^{2+} to Ni^{4+} transition during lithium extraction. Although the results on L_3 edge shifts allow for a Ni^{2+} to Ni^{3+} transition, the intensity results do not, and the Ni^{2+} to Ni^{3+} transition is not supported by computational work. We therefore conclude that the $Ni^{2+} \rightarrow Ni^{4+}$ oxidation does not occur during lithium removal.

Continuing with the method we developed in investigating the charge transfer in cathode materials, we studied the olivine phases Li_xFePO_4 with different lithium contents, x. The emergence of a pre-peak at O K-edge with delithiation indicates O donates its 2p electrons. The shift of Fe L_3 peak and the total intensity of Fe white lines were measured and compared with computational results. Good agreement was obtained. The increased Fe white lines intensity and upward shift of Fe L_3 peak are evidence of Fe oxidation. However,

the charge contributed by Fe is less than 0.5 electron per lithium atom removed. The rest of charge compensation is provided by O 2p states.

Mg_2Si is of interest both as an anode material in Li-ion batteries and as a hydrogen storage material for fuel cells. Although Mg_2Si has been studied for tens of years, the ionicity of its Mg-Si bond is controversial. The reported data ranges from less than 10% ionicity to fully ionic. We used EELS to measure the valence electron occupancy in Mg 3p states. We also performed first-principle calculations to explore its valence electron density distribution. We also investigated the typically ionic compound, MgO, and the pure covalent compound, crystalline Si, for comparison. Our results show that the Mg-Si bond has a very covalent character. The integrated atomic charge indicates 1.48 electrons are transferred from Mg to Si, resulting in a bond of 74% ionicity.

Contents

1 Basics of Li-ion Batteries 1

1.1 Introduction 1

1.2 Classification of batteries 2

1.3 The theoretical potential of a cell 2

1.4 The Gibbs' phase rule and voltage profile 4

1.5 Li-ion batteries 6

1.5.1 Cathodes for Li-ion batteries 8

1.5.2 Anodes for Li-ion batteries 13

2 Electron Scattering and EELS 18

2.1 Introduction to electron scattering 18

2.2 The theory of inelastic electron scattering 19

2.2.1 The Born approximation 19

2.2.2 The inelastic scattering cross-section 21

2.2.3 The Bethe surface 26

2.2.4 The dipole selection rule 27

2.3 Electron energy loss spectrometry (EELS) 29

2.3.1 Instrumentation 30

2.3.2 Features of an EELS spectrum 33

2.4 Spectrum processing for quantitative analysis 37

2.4.1 Extracting the single scattering distribution 37

2.4.2 Background subtraction 41

3 Local Electronic Structure of $Li_xNi_{0.5}Mn_{0.5}O_2$ and $Li_xNi_{1/3}Mn_{1/3}Co_{1/3}O_2$ 46

3.1 Introduction 46

3.2 Experimental 49

3.3 Computational 53

3.4 Results 55

3.4.1 EELS 55

3.4.2 Electronic structure calculations 60

3.5 Discussion 65

3.6 Conclusion 68

4 Local Electronic Structure of the Olivine Phases of Li_xFePO_4 74

4.1 Introduction 74

4.2 Experimental 76

4.3 Computational 77

4.4 Results 80

4.5 Discussion 87

4.6 Conclusion 90

5 Bonding in Mg_2Si 95

5.1 Introduction 95

5.2 Experimental 98

5.3 Computational 98

5.4 Results and discussion 100

5.5 Conclusion 108

6 Future Work **111**

6.1 Electronic structure of CF_x 111

6.2 Phase distribution in cathode and anode materials 113

6.2.1 Introduction 113

6.2.2 Elemental mapping 113

6.2.3 Valence electron density analysis 115

I Electron Density Plots for $LiFePO_4$ and $FePO_4$ **118**

List of Figures

1.1 Voltage profile of Madagascar natural graphite during charge and discharge with multiple plateaus corresponding to two-phase regions. 6

1.2 Schematic illustration of the charge/discharge process in a Li-ion battery using $LiCoO_2$ and C as cathode and anode, respectively. 7

1.3 The layered structure of $LiMO_2$. The unit cell is outlined by the wire frame. The long side is the c-axis. 9

1.4 The unit cell of spinel $LiMn_2O_4$ in symmetry $Fd\bar{3}m$ 10

1.5 The unit cell of olivine phase $LiFePO_4$. The long side is the a-axis. 12

2.1 Illustration of the wave vectors and particle positions for electronic scattering from an atom. 20

2.2 A schematic explanation of the differential cross-section $d\sigma/d\Omega$. 22

2.3 The Bethe surface for carbon K-edge showing the dependence of the GOS on both energy loss and scattering angle. 26

2.4 A schematic diagram showing the arrangement of an EELS spectrometer mounted on a TEM. 30

2.5 A schematic diagram showing the electron trajectories and energy dispersion in a 90˚ magnetic sector spectrometer. 32

2.6 A schematic diagram of a Gatan Model 666 PEELS system. 32

2.7 A rescaled spectrum of Si showing the components in an EELS spectrum. 33

2.8 The O K-edge in Fe_2O_3 showing the ample fine features in the ELNES region due to solid state effects. 36

2.9 (a) The power-law background model (dashed line) used to remove the background under Si L-edge (solid line). The pre-edge fitting window is shaded in gray. (b) The Si L-edge after background removal. 43

3.1 Indexed X-ray powder diffraction patterns from samples of different states of lithiation (a) $Li_xNi_{0.5}Mn_{0.5}O_2$ (with Si as an internal standard) and (b) $Li_xNi_{1/3}Mn_{1/3}Co_{1/3}O_2$. 50

3.2 Mn $L_{2,3}$ white lines from (a) $Li_xNi_{0.5}Mn_{0.5}O_2$ and (b) $Li_xNi_{1/3}Mn_{1/3}Co_{1/3}O_2$ with different x values. The spectra were normalized with a 50 eV window after the L_2 peak. 56

3.3 Co $L_{2,3}$ white lines from $Li_xNi_{1/3}Mn_{1/3}Co_{1/3}O_2$ with different *x* values. The spectra were normalized with a 40 eV window after the L_2 peak. 57

3.4 Ni $L_{2,3}$ white lines from (a) $Li_xNi_{0.5}Mn_{0.5}O_2$ and (b) $Li_xNi_{1/3}Mn_{1/3}Co_{1/3}O_2$ with different x values. The spectra were normalized with a 40 eV window after the L_2 peak. 58

3.5 Ni white line L_3 positions of $Li_xNi_{0.5}Mn_{0.5}O_2$ and $Li_xNi_{1/3}Mn_{1/3}Co_{1/3}O_2$ with different Li content, x. 59

3.6 Ni $L_{2,3}$ white line intensities of $Li_xNi_{0.5}Mn_{0.5}O_2$ and $Li_xNi_{1/3}Mn_{1/3}Co_{1/3}O_2$ with different Li content, x. The intensity is normalized to the fully lithiated sample with x = 1. 59

3.7 O K-edge from (a) $Li_xNi_{0.5}Mn_{0.5}O_2$ and (b) $Li_xNi_{1/3}Mn_{1/3}Co_{1/3}O_2$ with different x values. The spectra were normalized with the main peak (532-543 eV) to show the intensity of the pre-peak. 60

3.8 Normalized intensity of pre-peak at O K-edge of Li_xCoO_2, $Li_xNi_{0.8}Co_{0.2}O_2$, and $Li_xNi_{1/3}Mn_{1/3}Co_{1/3}O_2$, showing trends with delithiation. The pre-peak intensity (524-532 eV) is normalized to the main peak intensity (532-543 eV). The atomic cross sections were divided out of the experimental data.....61

3.9 Spin contained within spheres of radius about the Ni atom in $LiNi_{0.5}Mn_{0.5}O_2$ and $Li_{0.5}Ni_{0.5}Mn_{0.5}O_2$. 62

3.10 Valence charge contained within spheres of radius about the Ni atom in $LiNi_{0.5}Mn_{0.5}O_2$ and $Li_{0.5}Ni_{0.5}Mn_{0.5}O_2$. 63

3.11 Atomic multiplet calculation of Ni $L_{2,3}$ white lines using crystal field information from VASP. Compared to Ni^{2+}, the shift of the average L_3 white line is 3 eV for Ni^{4+}, inconsistent with the experimental result of Fig. 3.4. 64

3.12 VASP calculation of of oxygen p partial density of states of $Li_xNi_{0.5}Mn_{0.5}O_2$. The intensity from 0 to 4 eV above the Fermi level (E_f) corresponds to the intensity in the experimental pre-peak. The integrated DOS from the Fermi level is 30% more for x = 0.5. 64

4.1 Indexed X-ray powder diffraction patterns from samples of Li_xFePO_4 with different states of lithiation, with Si as an internal standard. 81

4.2 P $L_{2,3}$-edge from Li_xFePO_4. The spectra were normalized with a 50 eV window after the L_2 peak. 81

4.3 Li K-edge and Fe $M_{2,3}$-edge from Li_xFePO_4. The spectra were normalized with a 50 eV window after the peak. 83

4.4 O K-edge from Li_xFePO_4. The spectra were normalized with a 40 eV window after the main peak. 84

4.5 (a) Fe $L_{2,3}$-edges from Li_xFePO_4. The spectra were normalized with a 40 eV window after the L_2 peak. The measured shift of the L_3 centroid and the normalized white line intensities are plotted in (b) and (c), respectively. 85

4.6 The VASP calculation of Fe 3d partial density of states per formula unit. The intensity above the Fermi level corresponds to the intensity of white lines in EELS spectra. A 14% increase of the unoccupied states from $LiFePO_4$ to $FePO_4$ is predicted. 86

4.7 The VASP calculation of the O 2p partial density of states per formula unit. The intensity from 0 to 3 eV above the Fermi level corresponds to the intensity of the experimental pre-peak. 86

4.8 Atomic multiplet calculation of Fe $L_{2,3}$ white lines. 87

5.1 The antifluorite structure of Mg_2Si unit cell. 97

5.2 The Si $L_{2,3}$-edge of c-Si and Mg_2Si, respectively. The spectra were normalized with a 30 eV window 50 eV after the edge threshold. 100

5.3 The Mg $L_{2,3}$-edge of MgO and Mg_2Si, respectively. The spectra were normalized with a window from 80 - 100eV. 102

5.4 The calculated 2-D and 3-D valence electron density of c-Si on {110} type plane. The corresponding lattice plane is shown. 104

5.5 The calculated 2-D and 3-D valence electron density of MgO on {100} type plane. The corresponding lattice plane is shown. 105

5.6 The calculated 2-D and 3-D valence electron density of Mg_2Si on {110} type plane. The corresponding lattice plane is shown. 106

6.1 The layered structure of C_2F and CF prepared by using graphite as precursor. ..111

6.2 The C K-edge of graphite-based CF and pristine graphite. The spectra are normalized with a 50 eV window 40 eV beyond the σ^* peak. 112

6.3 (a) TEM bright field image of alumina with additions of barium silicate. (b) Elemental map using Ba $M_{4,5}$-edge shows the high concentration of Ba at grain boundary and triple pocket.....114

6.4 Contour and surface plot of lithium concentration in an Al-10.5at% alloy determined by shifts in the plasmon peak position. 115

I.1 Electron densities on the {010}-type lattice plane cutting through (0, 1/4, 0) for $LiFePO_4$ and $FePO_4$, respectively. 120

I.2 Electron densities on the (110) lattice plane for $LiFePO_4$ and $FePO_4$, respectively. 121

I.3 Electron densities on the $\{01\bar{1}\}$–type lattice plane cutting through (0, 1/2, 0) for LiFePO4 and FePO4, respectively. 122

List of Tables

3.1 Lattice constants of Li_xTMO_2 51

4.1 Bader analysis of the number of electrons surrounding O and Fe atoms per Li_xFePO_4 (x = 0, 1).....87

5.1 The equilibrium structures for c-Si, MgO and Mg_2Si.....99

5.2 Bader analysis of the number of electrons surrounding each atom 107

Chapter 1

Basics of Li-ion Batteries

1.1 Introduction

By the law of energy conservation, energy can be stored in various forms, e.g. chemical energy, electric energy, dynamic energy, gravity potential, etc. Under favorable conditions, energy can convert from one form to another. A battery is such a device that converts the chemical energy stored in its active materials into electric energy via electrochemical oxidation-reaction (redox) reactions.

The fundamental electrochemical unit accomplishing such energy conversion is called a “cell”. A battery can consist of one or more cells to achieve the desired capacity and voltage. In this work, our batteries contain only one cell, and we will interchange these two words for simplicity. A cell contains three major components: the cathode, the anode and the electrolyte [1]. When a cell discharges, the cathode accepts electrons and is reduced by the electrochemical reaction, while the anode gives out electrons and is oxidized. The electrolyte is an ionicly-conductive medium, either in liquid or in solid state, allowing ions to move from the anode to the cathode. Electric neutrality is maintained, when electrons move from the anode to the cathode via external electric circuit during discharge.

1.2 Classification of batteries

Based on their rechargeability, cells can be identified as primary or secondary cells. Primary cells generally have good shelf life and are easy to use, but they can not be easily or effectively recharged electrically and are discarded after use. On the contrary, secondary cells can restore their power, after discharge, by an external current flowing in the opposite direction to that of the discharge current. The advantages of secondary cells include reusability, high power density, high discharge rate, flat discharge curves and good low-temperature performance. They tend to have poorer charge retention than most primary cells. The most common secondary batteries include lead-acid batteries, nickel-cadmium batteries, nickel-metal hydride batteries and lithium ion (Li-ion) batteries [1].

1.3 The theoretical potential of a cell

When a cell discharges, the electrochemical reactions actually occur separately on both electrodes. The reduction on the cathode can be expressed, in generalized terms, as

$$aA + ne \rightarrow cC\,, \tag{1.1}$$

i.e. a moles of A accept n moles of electron e to form c moles of C. Likewise, the oxidation on the anode can be expressed as

$$bB - ne \rightarrow dD\,. \tag{1.2}$$

Combining above two equations, we have the overall reaction equation for the discharge process,

$$aA + bB \rightarrow cC + dD\,. \tag{1.3}$$

Under isothermal and isobaric conditions, the maximum non-volumetric work that can be done by an isolated system is determined by the decrease of its Gibbs free energy, ΔG. Assuming an ideal cell with quasi-static discharge, there is no dissipative work and the process is reversible. The only work done by the cell is the electrical work, W. By electrostatics,

$$W = Q \cdot V = nFV\,, \tag{1.4}$$

where V is the voltage of the cell and F is the Faraday constant (the number of Coulombs in one mole of electrons). If the process occurs under isothermal and isobaric conditions, and the system is isolated from its environment with no volumetric work, then the electrical work should equal the change of the Gibbs free energy of the cell. We have

$$\Delta G = -nFV\,. \tag{1.5}$$

Here, a negative sign is used because the cell is doing positive work.

In a system containing multiple phases, the chemical potential of the i^{th} component, μ_i, is defined as the partial differential of the Gibbs free energy G to n_i, the moles of component i,

$$\left(\frac{\partial G}{\partial n_i}\right)_{T,P,n_{j\neq i}} = \mu_i\,, \tag{1.6}$$

where T is temperature, P is pressure and n_j is the quantity of component j. In a system with constant temperature and pressure, Eq. (1.6) can be reorganized as

$$dG = \sum_i \mu_i dn_i \tag{1.7}$$

with

$$dn_i = \nu_i d\xi \,, \tag{1.8}$$

where ξ is the extent of reaction in one mole, a quantity equal for all reactants at a certain stage of a reaction [2]. For simplicity, we use v_i as the universal symbol for the coefficient of the i^{th} reactants in the reaction equation. It is positive for substances formed and negative for substances consumed. When a reaction proceeds with v_i moles of reactant i involved as shown in the chemical equation, $d\xi$ equals 1 mole and we have

$$\Delta G = \sum_i \mu_i \nu_i \,. \tag{1.9}$$

Comparing Eq. (1.9) with Eq. (1.5), the voltage V is obtained as

$$V = -\frac{1}{nF} \sum_i \mu_i \nu_i \,. \tag{1.10}$$

This equation is often used to calculate the theoretical potential.

1.4 The Gibbs' phase rule and voltage profile

The charge/discharge process of an electrochemical cell is always accompanied by the transport of matter (ions and electrons). When the amount of the transported matter exceeds a certain threshold, a phase transition may happen either in the cathode or in the

anode material. Such crystallographic changes can be observed by monitoring the cell potential, because variables in this thermodynamic system are governed by the Gibbs' phase rule. The Gibbs' phase rule states that the relation among the number of degrees of freedom *f*, the number of separate phases *p*, and the number of independent components *c*, in a closed system at equilibrium is given by

$$f = c - p + n, \tag{1.11}$$

where *n* is the number of the intensive variables necessary to describe the system except the mole fractions of the components in each phase [2]. In electrochemical studies, the intensive variables are only temperature and pressure. Hence, Gibbs' phase rule has the simplified form

$$f = c - p + 2. \tag{1.12}$$

In a Li-ion cell, the electrode can be treated as a binary system ($c = 2$) consisting of lithium and the corresponding delithiated phase. If we keep temperature and pressure fixed (which is usually assumed in battery reactions), the degrees of freedom reduces to

$$f = (2 - p + 2) - 2 = 2 - p. \tag{1.13}$$

If only one phase exists ($p = 1$), f equals 1. The potential of the cell varies with lithium concentration. However, if phase separation occurs and the electrode contains two phases ($p = 2$), f equals 0 and therefore no intensive variable (e.g. potential) can change. The potential remains fixed for all compositions. The voltage profile of Madagascar natural

graphite is shown in Fig. 1.1 as an example [3]. Each two-phase region can be clearly identified as a plateau in the curve.

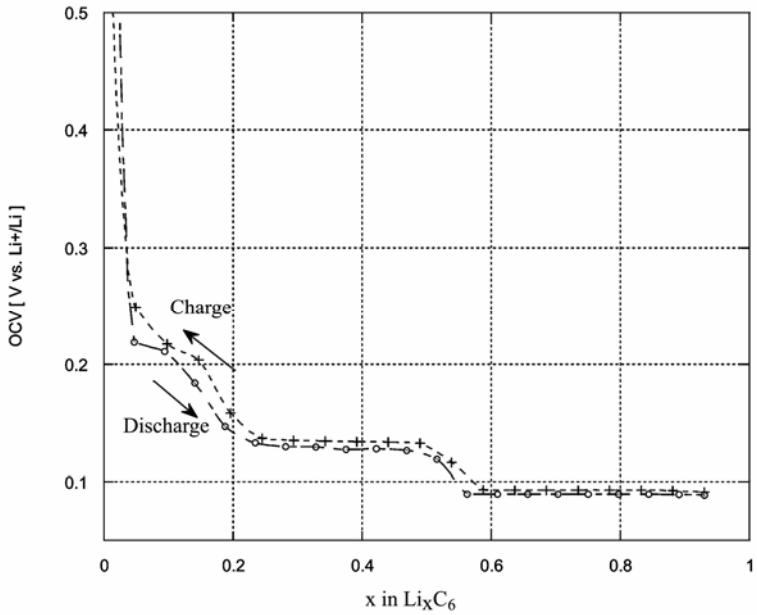

Fig. 1.1 Voltage profile of Madagascar natural graphite during charge and discharge with multiple plateaus corresponding to two-phase regions [3].

1.5 Li-ion batteries

Compared to other rechargeable battery systems such as lead-acid, nickel-cadmium and nickel-metal hydride batteries, lithium ion batteries provide higher volumetric and gravimetric energy density. They are very appealing for applications in portable electronic devices such as cellular phones, laptops and camcorders. The first attempt to construct a rechargeable lithium battery was by Whittingham in mid-1970s [4]. The cell used TiS_2 as the cathode, metallic lithium as the anode, and a non-aqueous electrolyte. However, metallic lithium is not a practical anode in rechargeable, liquid electrolyte batteries. During

charging, as lithium metal deposits onto the anode surface, dentrites are formed. The lithium dentrites eventually reach the positive electrode and cause an internal short-circuit [5]. Modern commercial lithium ion batteries use lithium-transition metal oxides, e.g. $LiCoO_2$, as the cathodes, and carbon-based materials, e.g. graphite, as hosts to store lithium at the anodes. As shown in Fig. 1.2, lithium ions move from the $LiCoO_2$ cathode to the Li_xC_6 anode through the electrolyte, and electrons move through the external circuit from the cathode to the anode during a charging process [6]. Replacing the lithium metal by carbon avoids the presence of metallic lithium in the whole charge/discharge process and therefore has significant advantages in terms of safety and cycle life. Unfortunately, it sacrifices energy density (3860 mAh/g for lithium vs. 372 mAh/g for carbon) [6].

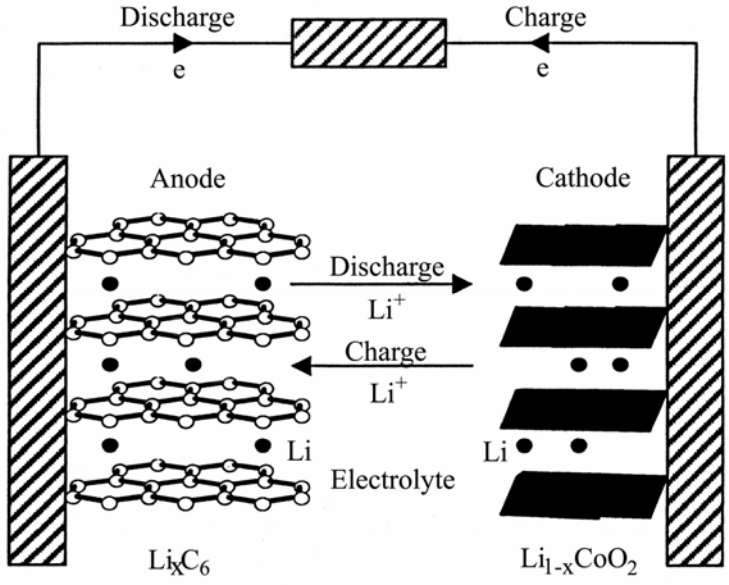

Fig. 1.2 Schematic illustration of the charge/discharge process in a Li-ion battery using $LiCoO_2$ and C as cathode and anode, respectively [6].

1.5.1 Cathodes for Li-ion batteries

A good cathode material for Li-ion batteries needs to fulfill several requirements:

1. The material is capable of allowing a large amount of lithium insertion and extraction to maximize the capacity of battery. This is determined by the number of available lithium sites and the achievable oxidation states of the remaining elements inside the material during lithium exchange. Some lithium-containing compounds can undergo a few different oxidation states, from low to high, during charging. These materials exhibit high energy density.
2. To improve the energy density, a high cell voltage is preferable. This requires that the cation M in compound LiMX, where X is the anion, has a high oxidation state. However, a high oxidation state often means a higher potential. Interfacial side-reactions and electrolyte oxidation can occur, causing cell failure.
3. To provide good cycle life for the cell, the material should have good tolerance for structural changes during the reversible lithium insertion and extraction process.
4. The material should have good electronic conductivity and ionic conductivity for lithium ions. This depends on many factors such as crystal structure, particle size and crystallization of the material. Poor conductivity can cause considerable polarization losses during the charge/discharge process, and prevents the cell

from being used in applications where high current density and power density are desired.

5. The material should be inexpensive for commercialization. It should also be lightweight to achieve high specific capacity.
6. Safe and environment friendly.

In modern Li-ion battery researches, cathode materials attracting the most attention fall into three main crystallographic categories: layered trigonal structure, spinel-type structure and channeled olivine-type structure [6].

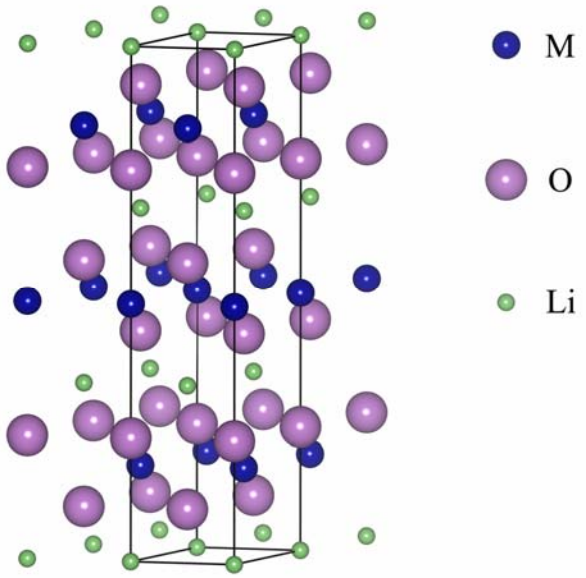

Fig. 1.3 The layered structure of $LiMO_2$. The unit cell is outlined by the wire frame. The long side is the c-axis.

The general formula for layered trigonal cathodes can be expressed as $LiMO_2$, where M is a 3d transition metal element or a mixture of several 3d transition metals. The structure of these compounds is shown in Fig. 1.3. This structure belongs to the trigonal

system with space group $R\bar{3}m$ (#166). Oxygen layers form the unit cell frame by stacking along the c-axis in a ···ABCABC··· sequence. Li and M atoms occupy the octahedral interstitial sites between oxygen atoms [7, 8]. This layered structure has good tolerance to structural changes during the extraction and insertion of lithium ions, and is therefore favorable for good cycle life [9]. The Li layer facilitates fast two-dimensional diffusion of Li^+. The edge-shared MO_6 octahedral arrangement with direct M-M interaction is believed to provide good electronic conductivity [6]. Unfortunately, the commercialization of these material is hindered by difficult synthesis, cation disorder (mixed occupancy between Li and M sites), and symmetry degradation caused by the Jahn-Teller distortion of M atoms [10, 11].

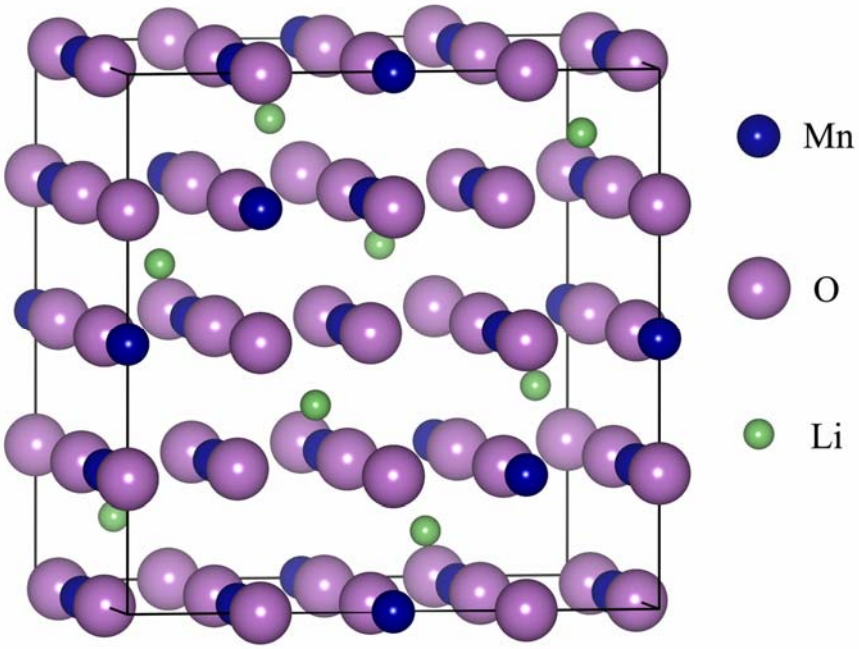

Fig. 1.4 The unit cell of spinel $LiMn_2O_4$ in symmetry $Fd\bar{3}m$.

The spinel phases with the general formula LiM_2O_4 are also of interest as cathodes in rechargeable Li-ion batteries. The structure of $LiMn_2O_4$ is shown in Fig. 1.4 as an example. These materials belong to cubic system with space group either $Fd\bar{3}m$ (#227) or $P4_332$ (#212) [12-14]. In $Fd\bar{3}m$ symmetry, M atoms occupy the 16d octahedral sites, while these sites split into 4a and 12c sites in $P4_332$ symmetry. In both cases, lithium atoms occupy the 8a tetrahedral sites. The edge-shared MO_6 octahedra framework provides good electrical conductivity, as in the layered $LiMO_2$ oxides. The interconnected lithium sites assure good ionic conductivity of Li^+. However, a cubic-to-tetragonal transition readily occurs during lithium extraction or insertion because of the difference between the energies of 8a and 16c sites, both of which can accommodate Li^+ [11, 15, 16]. This structural transition is accompanied by an intolerable volumetric change during charge/discharge cycling, and causes structural deterioration and fast capacity fade.

The idea to develop cathodes containing polyanions was motivated by the eagerness to utilize Fe in Li-ion batteries. Fe is the most available transition metal in the lithosphere. It is also less toxic than Co, Ni and Mn, which are currently used extensively. Unfortunately, layered $LiFeO_2$ is not a practical cathode material because of its structural instability caused by Fe migration from octahedral sites to tetrahedral sites [6]. However, this problem does not occur in complex iron oxides containing poly ions such as $(SO_4)^{2-}$

and $(MoO_4)^{2-}$ [17, 18]. For example, $Fe_2(SO_4)_3$ exhibited a capacity of 110 mAh/g with a flat discharge voltage of 3.6 V.

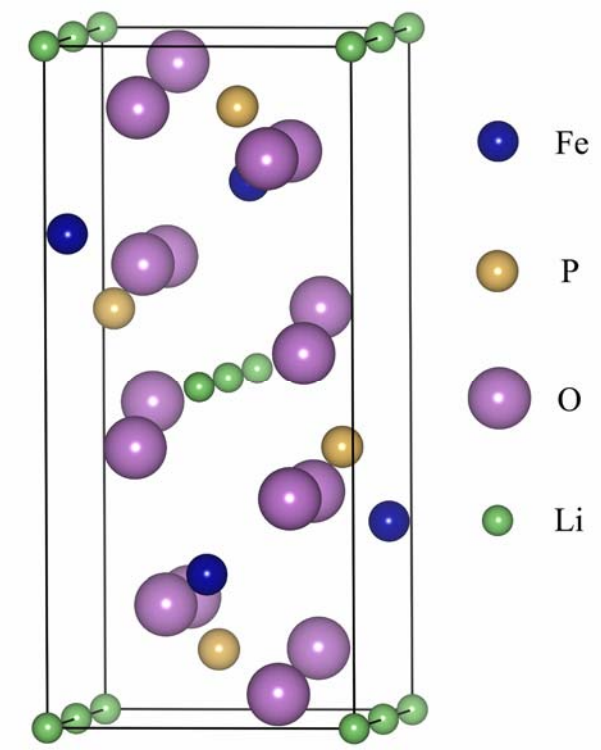

Fig. 1.5 The unit cell of olivine phase $LiFePO_4$. The long side is the a-axis.

The most promising material in this family is the olivine phase $LiFePO_4$ [19]. It has orthorhombic symmetry with space group *Pnma* (#62). The framework of the unit cell is constructed by FeO_6 octahedra and PO_4 tetrahedra. Lithium atoms are present as chains in the channels along the b-axis, as shown in Fig. 1.5. $LiFePO_4$ has a good theoretical capacity of 170 mAh/g and a reasonably high voltage [19]. It also has good structural and chemical stabilities resulting in satisfactory cycle life [20]. The main problem of this material is its poor conductivity [21]. Several techniques have been developed to overcome this

shortcoming, e.g., doping with supervalent cations, coating with carbon and reducing particle size [21-24].

1.5.2 Anodes for Li-ion batteries

The most widely used anode in Li-ion batteries is carbon. It exhibits a capacity as high as 372 mAh/g with a stable phase LiC_6. Its low chemical potential is favorable for a high cell voltage.

Some low-voltage lithium transition metal nitrides and intermetallic compounds have been investigated as anodes in rechargeable Li-ion batteries [6, 25]. $Li_{2.6-x}Co_{0.4}N$, $Li_{2.6-x}Cu_{0.4}N$ and $Li_{2.7-x}Fe_{0.3}N$ showed high capacities around 500 mAh/g at 0.2-1.3 V. Li_2CuSn demonstrated the capability of reversible extraction of two lithium atoms per formula unit [26]. One of the advantages of these materials is that they can be coupled with cathodes free of lithium. This brings more flexibility in designing a Li-ion cell.

Recently, nano-sized and amorphous Ge and Si were proposed to be appealing candidates as anodes. Nanocrystalline Ge showed a reversible capacity of 1400 mAh/g with 60% capacity retained after 50 cycles, and amorphous Ge showed a stable capacity of 1700 mAh/g after 60 cycles [27]. Nanocrystalline Si exhibited a capacity of 1100 mAh/g with a 50% retention after 50 cycles, and amorphous Si exhibited a stable capacity of 2000 mAh/g over 50 cycles [28]. The high capacity benefits from the light weight and high solubilities of lithium in Ge and Si. The short diffusion distance in these nano-sized and

amorphous materials is suggested to be favorable fast relaxation of the strain field and therefore suppresses structural damage during cycling.

References

[1] Linden, D.; Reddy, T.B. *Handbook of Batteries (3rd edition)*; McGraw-Hill: New York, 2001.

[2] Fu, X. C.; Shen, W. X.; Yao, T. Y. *Physical Chemistry (4th edition)*; Advanced Education Press: Beijing, 1990.

[3] Reynier, Y. *Ph.D thesis*; Grenoble University, 2005.

[4] Whittingham, M. S. *Science* 1976, 192, 1126.

[5] Besenhard, J. O. *Handbook of Battery Materials*; WILEY-VCH: New York, 1999.

[6] Nazri, G. A. *Lithium Batteries Science and Technology*; Kluwer Academic: Norwell, 2004.

[7] Johnston, W. D.; Heikes, R. R.; Sestrich, D. *J. Phys. Chem. Solids* 1958, 7, 1.

[8] Orman, H. J.; Wiseman, P. J. *Acta Cryst.* 1984, C40, 12.

[9] Ohzuku, T.; Ueda, A. *Solid State Ionics* 1994, 69, 201.

[10] Rougier, A.; Delmas, C. *Solid State Commun.* 1995, 94, 123.

[11] Gummow, R. J.; Liles, D. C.; Thackeray, M. M. *Mater. Res. Bull.* 1993, 28, 1249.

[12] Kim, J. H.; Myung, S. T.; Yoon, C. S.; Kang, S. G.; Sun, Y. K. *Chem. Mater.* 2004, 16, 906.

[13] Gryffroy, D.; Vandenberghe, R. E.; Legrand, E. *Mater. Sci. Forum* 1991, 79-82, 785.

[14] Lee, Y. J.; Eng. C.; Grey, C. P. *J. Electrochem. Soc.* 2001, 148, A249.

[15] Aydinol, M. K.; Ceder, G. *J. Electrochem. Soc.* 1997, 144, 3832.

[16] Thackeray, M. M.; David, W. I. F.; Bruce, P. G.; Goodenough, J. B. *Mater. Res. Bull.* 1983, 18, 461.

[17] Manthiram, A.; Goodenough, J. B. *J. Power Sources* 1989, 26, 403.

[18] Manthiram, A.; Goodenough, J. B. *J. Solid State chem.* 1987, 71, 349.

[19] Padhi, A. K.; Nanjundaswamy, K. S.; Goodenough, J. B. *J. Electrochem. Soc.* 1997, 144, 1188.

[20] Deb, A.; Bergmann, U.; Cramer, S. P.; Cairns, E. J. *Electrochimica Acta* 2005, 50, 5200.

[21] Chung, S. Y.; Bloking, J. T.; Chiang, Y. M. *Nature Materials* 2002, 1, 123.

[22] Huang, H.; Yin, S. C.; Nazar, L. F. *Electrochem. Solid-State Lett.* 2001, 4, A170.

[23] Chen, Z; Dahn, J. R. *J. Electrochem. Soc.* 2002, 149, A1184.

[24] Yamada, A; Chung, S. C.; Hinokuma, K. *J. Electrochem. Soc.* 2001, 148, A224.

[25] Rowsell, J. L. C.; Pralong, V.; Nazar, L. F. *J. Am. Chem. Soc.* 2001, 123, 8598.

[26] Vaughey, J. T.; Kepler, K. D.; Benedek, R.; Thackeray, M. M. *Electrochem. Commun.* 1999, 1, 517.

[27] Graetz, J.; Ahn, C. C.; Yazami, R.; Fultz, B. *J. Electrochem. Soc.* 2004, 151, A698.

[28] Graetz, J.; Ahn, C. C.; Yazami, R.; Fultz, B. *Electrochem. Solid State Lett.* 2003, 6, A194.

Chapter 2

Electron Scattering and EELS

2.1 Introduction to electron scattering

In a transmission electron microscope (TEM), high-energy primary electrons (also known as incident electrons or fast electrons) interact with the specimen and are scattered. In terms of energy loss of the primary electrons, the scattering of the incident electrons can be divided into two categories: elastic scattering and inelastic scattering.

Elastic scattering involves no change in the energy of the primary electrons. It is the major mechanism that deflects the primary electrons in TEM, and makes the main contribution to diffraction patterns and image contrast. When a primary electron is scattered elastically, there are two basic types of events [1].

1. Large-angle elastic scattering, also known as Rutherford scattering, in which the incident electron often undergoes a change greater than 5° in direction. This process represents the interaction of the fast electrons with the Coulomb potential of an atomic nucleus. It only happens when the incident electron travels very close to the nucleus.
2. Small-angle elastic scattering, in which the change in the direction of the

incident electron is typically less than a few degrees. Classically, this process occurs when the fast electron travels farther from the nucleus and is scattered by the electron cloud of the atom.

In inelastic scattering, a part of the kinetic energy of the incident electron is transferred to the electrons or atoms of the specimen. The main types of inelastic processes include phonon excitation, plasmon excitation, single electron excitation and bremsstrahlung radiation [2]. Analysis of the energy of the inelastically scattered electrons forms the basis for electron energy loss spectrometry (EELS).

2.2 The theory of inelastic electron scattering

2.2.1 The Born approximation

In developing the scattering formalism, it is convenient to describe the primary electrons as electron waves. In solving the scattered wavefunction, an approximation is required to obtain an explicit solution. The one often used is the Born approximation. The Born approximation assumes that the kinetic energy of the incident electrons is much greater than the energy of the excited atomic states. In its first-order form (known as the first Born approximation), this approximation is equivalent to assuming that the wave is undiminished and scattered only once [3]. This is valid for weak scattering. A more quantitative criterion is that $Z<<137(v/c)$ [4], where Z is the atomic number; v is the speed

of the fast electron and *c* is the speed of light in vacuum. For most elements of interest for materials science and the operating voltage in a TEM, this condition is readily satisfied.

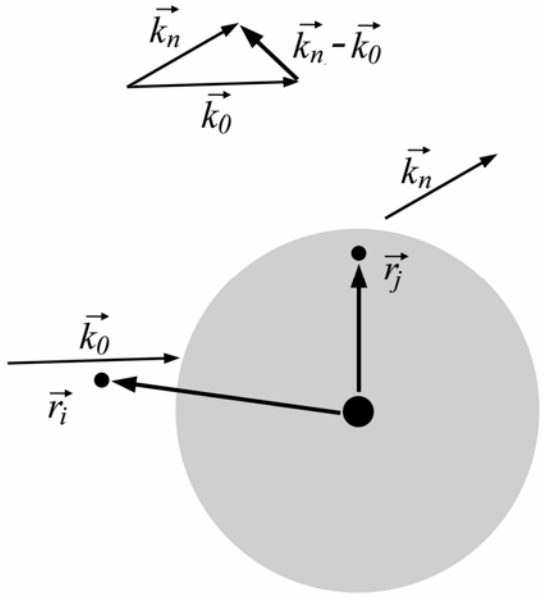

Fig. 2.1 Illustration of the wave vectors and particle positions for electronic scattering from an atom.

It is accurate to write the incident electron before scattering as a plane wave

$$\Phi_0 = \exp(2\pi i \mathbf{k}_0 \cdot \mathbf{r}), \tag{2.1}$$

where $\mathbf{k}_0$ is the wave vector and $\mathbf{r}$ is the vector coordinate for the position of the incident electron. Within the first Born approximation, the scattered wave is also in the form of a plane wave,

$$\Phi_n = \exp(2\pi i \mathbf{k}_n \cdot \mathbf{r}'), \tag{2.2}$$

where $\boldsymbol{k}_n$ and $\boldsymbol{r}'$ are the wave vector and vector coordinate of the scattered electron, respectively. The total wavefunction of the system of an incident electron and an atomic electron is therefore a product of the atomic states and plane wave states

$$\begin{aligned} \Psi_0 &= a_0(\boldsymbol{r}_j)\Phi_0 = a_0(\boldsymbol{r}_j)\exp(2\pi i\boldsymbol{k}_0 \cdot \boldsymbol{r}_i) \\ \Psi_n &= a_n(\boldsymbol{r}_j)\Phi_n = a_n(\boldsymbol{r}_j)\exp(2\pi i\boldsymbol{k}_n \cdot \boldsymbol{r}_i) \end{aligned} \tag{2.3}$$

where $a_0(\boldsymbol{r}_j)$ and $a_n(\boldsymbol{r}_j)$ are the wavefunctions of the atomic states; $\boldsymbol{r}_i$ and $\boldsymbol{r}_j$ are the coordinates for the incident and atomic electrons, respectively. The scattering geometry is shown in Fig. 2.1 with the origin at the nucleus.

2.2.2 The inelastic scattering cross-section

An important quantity in scattering theory is the cross-section σ, which represents the probability of an incident electron being scattered by a given atom. As an example, the scattering of an electron by the Coulomb potential of a nucleus is illustrated in Fig. 2.2 [5]. The electrons travel on hyperbolic trajectories due to the attractive Coulomb force. If there were no interaction between the electron and the nucleus, the electron would travel straight and past the nucleus, and the shortest distance between them is defined as the impact parameter a. The change in the direction of the electron is described by the scattering angle θ. This θ decreases with increasing a. Electrons that pass through an element of area $d\sigma$ of the incident beam will be scattered into a cone of solid angle $d\Omega$. The ratio $d\sigma/d\Omega$ is known as the differential cross-section, and is a function of θ. The differential cross-section describes the angular distribution of the scattered electrons.

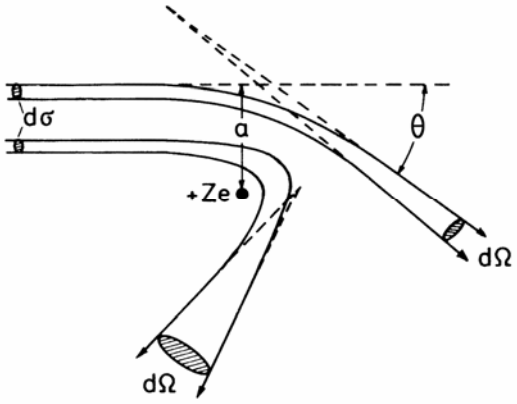

Fig. 2.2 A schematic explanation of the differential cross-section $d\sigma/d\Omega$.

By treating the presence of the incident electron as a perturbation to the Hamiltonian of the system, the inelastic scattering differential cross-section can be obtained [6] by Fermi's golden rule

$$\frac{d\sigma_{0n}}{d\Omega} = \frac{4\pi^2 m^2}{h^4}\frac{k_n}{k_0}\left|\left\langle \Psi_n \middle| V(\mathbf{r}_i, \mathbf{r}_j) \middle| \Psi_0 \right\rangle\right|^2, \tag{2.4}$$

where Ψ_0 and Ψ_n are the initial and final wavefunctions as described in Eq. (2.3); $V(\mathbf{r}_i,\mathbf{r}_j)$ is the perturbing Hamiltonian; m is the rest mass of a electron and h is Plank's constant. The perturbing Hamiltonian has the form

$$V(\mathbf{r}_i, \mathbf{r}_j) = -\frac{e^2 Z}{4\pi\varepsilon_0 r_i} + \sum_{j=1}^{Z}\frac{e^2}{4\pi\varepsilon_0\left|\mathbf{r}_i - \mathbf{r}_j\right|}, \tag{2.5}$$

where e is the elementary charge; Z is the atomic number of the atom, and ε_0 is the permittivity of free space. The first term represents the interaction between the incident electron and the nucleus. The second term is the repulsive Coulombic interaction between

the incident and the atomic electrons. Substituting Eq. (2.3) and Eq. (2.4) into Eq. (2.5), the differential cross-section becomes

$$\frac{d\sigma_{0n}}{d\Omega}$$

$$= \frac{4\pi^2 m^2}{h^4}\frac{k_n}{k_0}\left|\left\langle a_n\Phi_n\left|-\frac{e^2 Z}{4\pi\varepsilon_0 r_i}\right|a_0\Phi_0\right\rangle + \left\langle a_n\Phi_n\left|\sum_{j=1}^{Z}\frac{e^2}{4\pi\varepsilon_0\left|\boldsymbol{r}_i-\boldsymbol{r}_j\right|}\right|a_0\Phi_0\right\rangle\right|^2 \quad . \quad (2.6)$$

$$= \frac{4\pi^2 m^2}{h^4}\frac{k_n}{k_0}\left|\left\langle \Phi_n\left|-\frac{e^2 Z}{4\pi\varepsilon_0 r_i}\right|\Phi_0\right\rangle\left\langle a_n|a_0\right\rangle + \left\langle a_n\Phi_n\left|\sum_{j=1}^{Z}\frac{e^2}{4\pi\varepsilon_0\left|\boldsymbol{r}_i-\boldsymbol{r}_j\right|}\right|a_0\Phi_0\right\rangle\right|^2$$

In Eq. (2.6), the first term in the modulus cancels because of the orthogonality of the atomic wavefunctions

$$\left\langle a_n|a_0\right\rangle = \delta_{n0} . \quad (2.7)$$

The second term is

$$\left\langle a_n\Phi_n\left|\sum_{j=1}^{Z}\frac{e^2}{4\pi\varepsilon_0\left|\boldsymbol{r}_i-\boldsymbol{r}_j\right|}\right|a_0\Phi_0\right\rangle$$

$$= \iint \exp(-2\pi i\boldsymbol{k}_n\cdot\boldsymbol{r}_i)a_n^*\left(\sum_{j=1}^{Z}\frac{e^2}{4\pi\varepsilon_0\left|\boldsymbol{r}_i-\boldsymbol{r}_j\right|}\right)a_0\exp(2\pi i\boldsymbol{k}_0\cdot\boldsymbol{r}_i)d^3\boldsymbol{r}_i d^3\boldsymbol{r}_j \quad . \quad (2.8)$$

Making the variable substitution $\boldsymbol{q} = 2\pi(\boldsymbol{k}_n - \boldsymbol{k}_0)$, and noting the integral

$$\int\frac{\exp(-i\boldsymbol{q}\cdot(\boldsymbol{r}_i-\boldsymbol{r}_j))}{\left|\boldsymbol{r}_i-\boldsymbol{r}_j\right|}d^3\boldsymbol{r}_i = \frac{4\pi}{q^2}, \quad (2.9)$$

Eq. (2.6) becomes

$$\frac{d\sigma_{0n}}{d\Omega} = \frac{k_n}{k_0}\left(\frac{me^2}{2\pi\varepsilon_0 h^2}\right)^2\left(\frac{2\pi}{q}\right)^4\left|\sum_{j=1}^{Z}\int a_n^* a_0 \exp(-i\boldsymbol{q}\cdot\boldsymbol{r}_j)d^3\boldsymbol{r}_j\right|^2$$
$$= \frac{k_n}{k_0}\frac{4}{a_b^2 q^4}\left|\sum_{j=1}^{Z}\int a_n^* a_0 \exp(-i\boldsymbol{q}\cdot\boldsymbol{r}_j)d^3\boldsymbol{r}_j\right|^2, \quad (2.10)$$

where

$$a_b = \frac{\varepsilon_0 h^2}{\pi me^2} \quad (2.11)$$

is the Bohr radius. Considering the relativistic effect on electron mass [7], Eq. (2.11) is corrected as

$$\frac{d\sigma_{0n}}{d\Omega} = \frac{k_n}{k_0}\frac{4\gamma^2}{a_b^2 q^4}\left|\sum_{j=1}^{Z}\int a_n^* a_0 \exp(-i\boldsymbol{q}\cdot\boldsymbol{r}_j)d^3\boldsymbol{r}_j\right|^2, \quad (2.12)$$

where γ is the relativistic correction factor for mass, $\gamma = 1\Big/\sqrt{1-v^2/c^2}$; v and c are the speed of the incident electron and the speed of light in vacuum, respectively.

A quantity known as the generalized oscillator strength (GOS) [7] is defined as

$$f(q) = \frac{\Delta E}{R(a_b q)^2}\left|\sum_{j=1}^{Z}\int a_n^* a_0 \exp(-i\boldsymbol{q}\cdot\boldsymbol{r}_j)d^3\boldsymbol{r}_j\right|^2, \quad (2.13)$$

where

$$R = \frac{me^4}{8\varepsilon_0^2 h^2} \quad (2.14)$$

is the Rydberg energy, and ΔE is the excitation energy that promotes the atom from state a_0 to a_n. By the conservation of energy, ΔE equals the loss of the kinetic energy of the

scattered incident electron. The differential cross-section is expressed in terms of the GOS as

$$\frac{d\sigma_{0n}}{d\Omega} = \frac{k_n}{k_0}\frac{4\gamma^2 R}{q^2 \Delta E} f(q). \tag{2.15}$$

In studying scattering events with continuous energy loss (e.g., ionization of an atom where the final states form a continuum), it is more convenient to use a GOS per unit energy loss, $df(q,\Delta E)/d\Delta E$. Then, we obtain the double differential cross-section for inelastic electron scattering

$$\frac{d^2\sigma_{0n}}{d\Omega d\Delta E} = \frac{k_n}{k_0}\frac{4\gamma^2 R}{q^2 \Delta E}\frac{df(q,\Delta E)}{d\Delta E}. \tag{2.16}$$

Eq. (2.16) describes the angular and energetic dependence of inelastic scattering. To relate the double differential cross-section to experimental data which contain considerable details arising from bondings in solids, Eq. (2.16) must be weighted by the density of unoccupied states, $\rho(E_n)$ [8-10]. The final expression of the double differential cross-section for inelastic electron scattering in solids is

$$\frac{d^2\sigma_{0n}}{d\Omega d\Delta E} = \frac{4\gamma^2 R}{q^2 \Delta E}\frac{df(q,\Delta E)}{d\Delta E}\rho(E_n). \tag{2.17}$$

Here, we take the approximation $k_n/k_0 \approx 1$, because ΔE is very small compared to the kinetic energy of the incident electron and therefore the k_n is very close to k_0.

2.2.3 The Bethe surface

A plot of $df(q,\Delta E)/d\Delta E$ is called the Bethe surface [2]. Fig. 2.3 shows the calculated Bethe surface for the carbon K-shell ionization. The GOS exhibits a maximum (Bethe ridge) at larger q (equivalently, larger scattering angle θ). This area corresponds to "hard-sphere" collisions with large momentum transfer as if the atomic electron was at rest [2]. Both core electrons and valence electrons can be involved in this process. The more stationary valence electrons contribute to the central region of the ridge, while the core electrons broaden the ridge due to their larger kinetic energies [7].

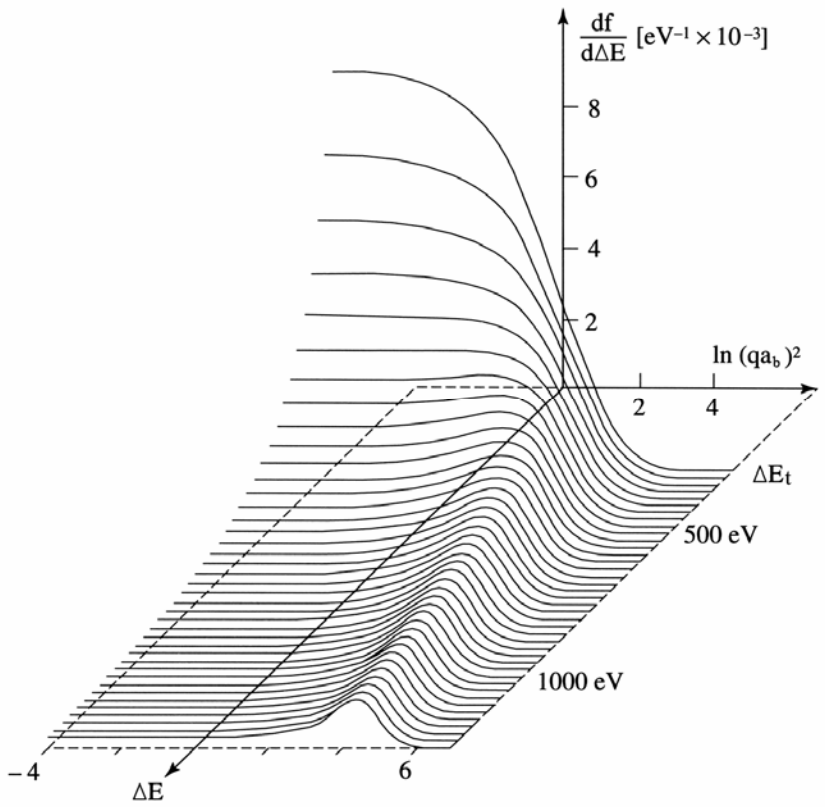

Fig. 2.3 The Bethe surface for carbon K-edge showing the dependence of the GOS on both energy loss and scattering angle.

Experimentally, the measured intensity in an EELS spectrum is the total number of scatterings within a certain scattering angle θ_a, which is selected by using a collection aperture. A small aperture will collect most of the intensity at energies just above the ionization energy, ΔE_t in Fig. 2.3. This small aperture is also useful for improving the signal-to-background ratio (SBR) by suppressing the background intensity at large q that originates from the tails of other features with lower energy loss. However, at energies well above ΔE_t, a large aperture is necessary to obtain enough counts before radiation damage occurs in the specimen [3]. For some specific studies, e.g. electron-Compton measurements, an even larger aperture must be used to include a significant portion of the Bethe ridge [7].

2.2.4 The dipole selection rule

During an inelastic scattering event, the atom is excited from the initial state with a wavefunction a_0 to the final states with a wavefunction a_n by absorbing energy ΔE. The probability of such a transition with a given scattering angle is governed by the double differential cross-section, as shown in Eq. (2.13) and Eq. (2.17). The exponential terms in the Eq. (2.13) can be expanded as Taylor series

$$\exp(-i\boldsymbol{q}\cdot\boldsymbol{r}_j) = 1 - i\boldsymbol{q}\cdot\boldsymbol{r}_j - \frac{(\boldsymbol{q}\cdot\boldsymbol{r}_j)^2}{2!} + i\frac{(\boldsymbol{q}\cdot\boldsymbol{r}_j)^3}{3!}\cdots. \tag{2.18}$$

For small q, higher power terms can be neglected. The integral becomes

$$\int a_n^* a_0 \exp(-i\boldsymbol{q}\cdot\boldsymbol{r}_j) d^3\boldsymbol{r}_j \approx \int a_n^* a_0 d^3\boldsymbol{r}_j + \int a_n^* a_0 (-i\boldsymbol{q}\cdot\boldsymbol{r}_j) d^3\boldsymbol{r}_j \,. \tag{2.19}$$

The first integral on the right side vanishes due to the orthogonality of the atomic wavefunctions. As discussed in section 2.2.3, the EELS spectrum is collected up to a certain scattering angle θ_a. Therefore, the spectral intensity represents the integrated double differential cross-section within the corresponding solid angle Ω_a

$$\begin{aligned} I_{\Delta E} &\propto \frac{d\sigma_0}{d\Delta E} \\ &= \sum_n \int_0^{\Omega_a} \frac{d^2\sigma_{0n}}{d\Omega d\Delta E} d\Omega \\ &\propto \sum_n \left(\int_0^{\Omega_a} \rho(E_n) \left| \sum_{j=1}^{Z} \int a_n^* a_0 \exp(-i\boldsymbol{q}\cdot\boldsymbol{r}_j) d^3\boldsymbol{r}_j \right|^2 d\Omega \right) \end{aligned} \,. \tag{2.20}$$

Here we sum over all possible final states because all transitions make contributions to the spectral intensity [2]. By substituting Eq. (2.19) into Eq. (2.20), we have

$$I_{\Delta E} \propto \sum_n \left(\int_0^{\Omega_a} \rho(E_n) \left| \sum_{j=1}^{Z} \int a_n^* a_0 (-i\boldsymbol{q}\cdot\boldsymbol{r}_j) d^3\boldsymbol{r}_j \right|^2 d\Omega \right). \tag{2.21}$$

This is known as the dipole approximation. The squared term can be further simplified

$$\begin{aligned} \left| \sum_{j=1}^{Z} \int a_n^* a_0 (-i\boldsymbol{q}\cdot\boldsymbol{r}_j) d^3\boldsymbol{r}_j \right|^2 &= \left| \sum_{j=1}^{Z} \int a_n^* a_0 (q_x x + q_y y + q_z z) d^3\boldsymbol{r}_j \right|^2 \\ &= \left| q^2 \sum_{j=1}^{Z} \int a_n^* a_0 \boldsymbol{r}_j d^3\boldsymbol{r}_j \right|^2 \end{aligned} \,, \tag{2.22}$$

because the circular symmetry of the collection aperture will cause all cross term (involving $q_x q_y$, etc.) to vanish [2], when integrated over the solid angle. Now, we have the spectral intensity as

$$I_{\Delta E} \propto \sum_n \left(\int_0^{\Omega_a} \rho(E_n) \left| q^2 \sum_{j=1}^{Z} \int a_n^* a_0 \mathbf{r}_j d^3 \mathbf{r}_j \right|^2 d\Omega \right). \tag{2.23}$$

Quantum mechanics shows that the integral in Eq. (2.23) is nonzero only when $\Delta l = \pm 1$, where l is the angular momentum of the atomic state. This is known as the dipole selection rule. Only those transitions allowed by this rule can contribute to the spectrum. The dipole selection is valid for small scattering angle, $\boldsymbol{q} \cdot \boldsymbol{r} << 1$. At large scattering angles, contributions from higher order terms in Eq. (2.18) may be significant.

2.3 Electron energy loss spectrometry (EELS)

Electron energy loss spectrometry (EELS) refers to the techniques which use monoenergetic electrons to probe a specimen, and analyze the energy distribution of the scattered primary electrons after interaction. A few variants have been developed and each has its unique instrumentation, advantages and disadvantages. In the present work, we employ the EELS technique conducted in the environment of a transmission electron microscope (TEM).

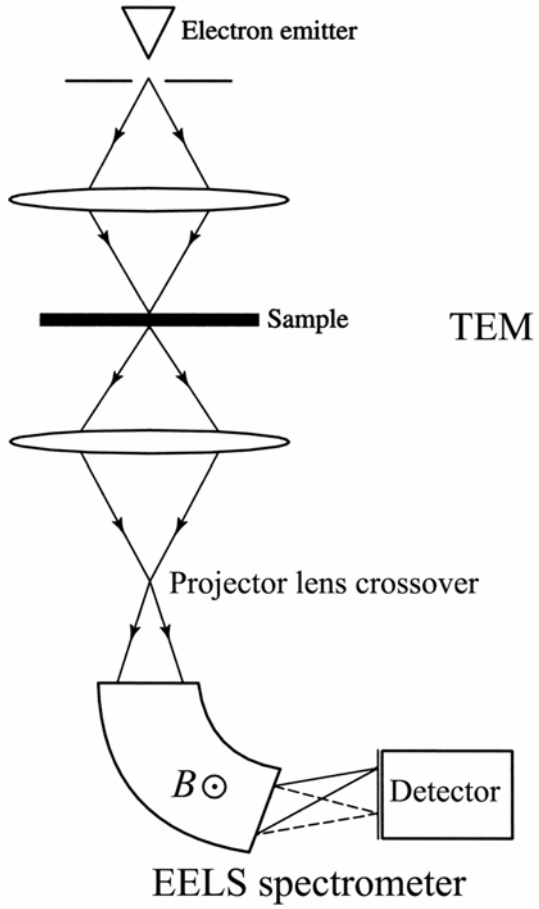

Fig. 2.4 A schematic diagram showing the arrangement of an EELS spectrometer mounted on a TEM.

2.3.1 Instrumentation

For TEM-based EELS, high-energy electrons are focused on a thin specimen and the transmitted primary electrons are collected by the EELS spectrometer mounted at the bottom of the TEM column. This arrangement is shown schematically in Fig. 2.4. There are different designs of EELS spectrometers. However, all of them use a static-magnetic field to separate electrons with different energies [2]. Fig. 2.5 shows how the electrons are dispersed by a 90˚ magnetic sector spectrometer. The spectrometer is focused on the

crossover of the projector lens of the TEM. Electrons with a velocity v enter the magnetic field $\boldsymbol{B}$ produced by the pair of magnets and travel along a circular trajectory due to the Lorentz force $\boldsymbol{F} = -e\boldsymbol{v} \times \boldsymbol{B}$. The radius of curvature R is given by

$$R = \frac{\gamma v m}{eB}. \tag{2.24}$$

where γ, v and m have same meanings as in section 2.2.2. The dependence of R on v implies that electrons with different energies will travel along different trajectories even if they initially enter the magnetic field at the same point. On the other hand, the trajectories of electrons with the same energy can cross at a single point on the dispersion plane if the lens is well designed. Thus, all electrons are aligned according to their energies and an EELS spectrum is formed. A real spectrometer, as shown in Fig. 2.6, has more components for better functionality. QX and QY are quadrupole magnetic lenses to correct the first-order aberration of the sector magnets. The second-order aberration is corrected by the sextupole lenses SX and SY. Q1-Q4 are quadrupole lenses to increase the energy dispersion by enlarging the spectrum. Finally, the spectrum is recorded by a photodiode array fiber-optically coupled to a thin YAG (yttrium aluminum garnet) scintillator [7].

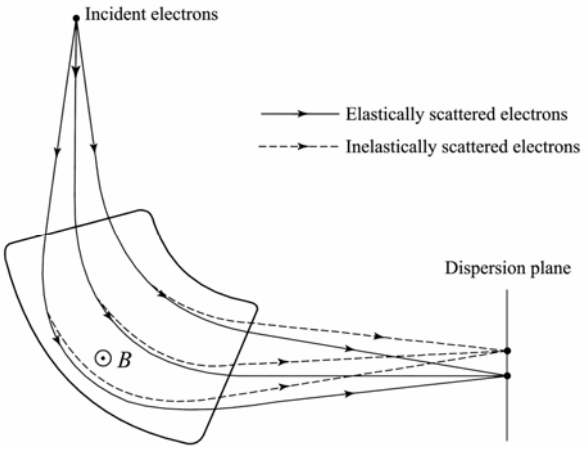

Fig. 2.5 A schematic diagram showing the electron trajectories and energy dispersion in a 90˚ magnetic sector spectrometer.

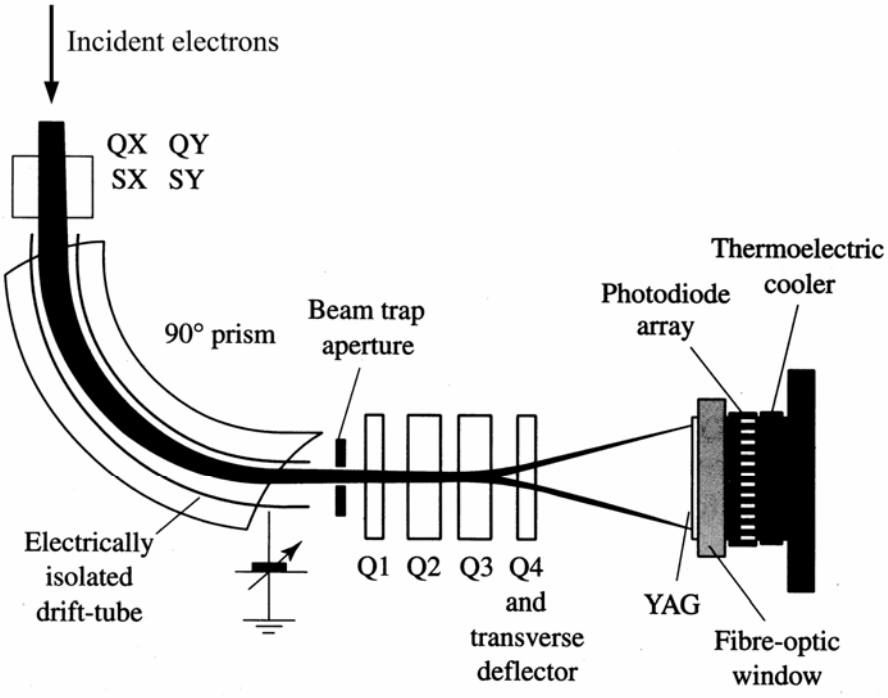

Fig. 2.6 A schematic diagram of a Gatan Model 666 PEELS system.

2.3.2 Features of an EELS spectrum

A typical transmission EELS spectrum is shown schematically in Fig. 2.7 with the x-axis being the energy loss of the primary electron. The first part from the left side is the zero loss peak (ZLP) around 0 eV. It contains all the elastically and quasi-elastically scattered electrons [2]. The energy spread of the ZLP mainly originates from the non-monochromaticity of the electron source in the TEM. The quasi-elastically scattered electrons experience very small energy (e.g. excitation of phonons) which can not be resolved by conventional TEM-EELS. However, this quasi-elastic component may become relatively significant and eventually be separated from the ZLP if a highly monochromatized electron emitter is used. The full width at half maximum (FWHM) of the ZLP determines the overall resolution of the spectrum [2].

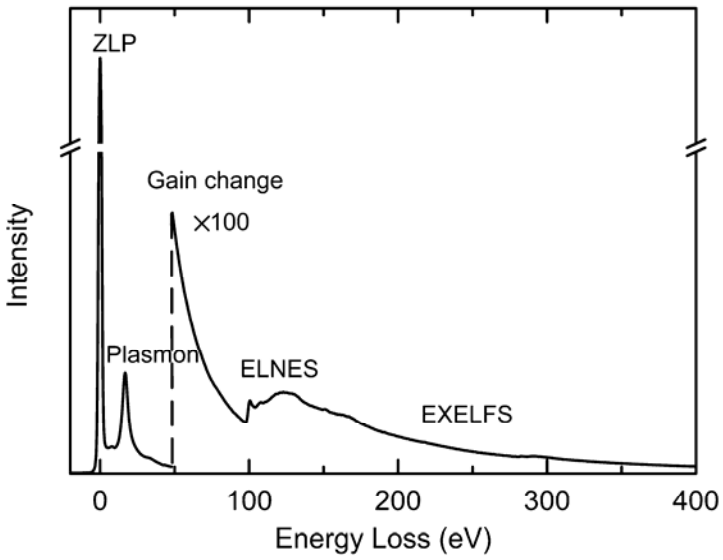

Fig. 2.7 A rescaled spectrum of Si showing the components in an EELS spectrum.

From the ZLP to about 50 eV is the “low-loss region.” It corresponds to interactions between the primary electrons and the atomic valence electrons which are often delocalized due to interatomic bonding. The transferred energy triggers collective, resonant oscillations of the valence electrons known as “plasmons.” The plasmon peak position is a function of valence electron density in the material. Analysis of the plasmon peak can provide useful information about properties such as phase distribution, degree of solid solution formation, electrical conductivity, thermal conductivity, etc., which are largely determined by valence electrons. For insulators or semiconductors, there may also appear relatively small peaks superimposed on the big plasmon peak [2]. These are single electron excitations from the valence band to the conduction band. They represent a convolution between the density of states (DOS) of the valence and conduction bands. Hence, analysis of the details of the whole low-loss region, both plasmon and interband transitions, can give information on band structure which is of particular interest to semiconductor investigations, and sometimes is referred as “valence electron energy loss spectrometry” (VEELS) [11].

Beyond the low-loss part of the spectrum is the high-loss part, which can extend to several thousand eV. This region exhibits distinct peaks superimposed on a monotonically decreasing background. These peaks correspond to excitations of well-localized core electrons of atoms and are known as ionization edges. The edge

threshold is determined by the binding energy of the core electron, which is a characteristic quantity of an element. Hence, the edge position can be used to identify the atomic species. It should be kept in mind that the energy threshold of an ionization edge can be affected by the chemical environment of the atom. Variation up to a few eV can occur for same atoms in different compounds. This is known as the "chemical shift." The intensity of the edge is proportional to the number of atoms in the material, so the intensity can be used for the measurement of composition.

For free atoms, the shapes of the absorption edges are determined by the overlap between the initial and final states. The calculated edge shapes are simple and structureless [12]. However, ample details are observed on experimentally measured edges, as shown in Fig. 2.8. This is known as the energy loss near-edge structure (ELNES). The ELNES normally exists within ~50 eV above the edge threshold and is a solid-state effect. In solids, the unoccupied electronic states near the Fermi level are modified by chemical bonding, which creates a complicated density of states (DOS). A correct calculation of the ELNES requires incorporating the DOS of the corresponding final states $\beta(E_n)$ into the atomic differential cross-section, as we did in Eq. (2.17). Since the tight-bound initial core state is essentially an energy delta function, the ELNES directly reflects the DOS of the unoccupied states around the Fermi level, as allowed by the transition selection rule.

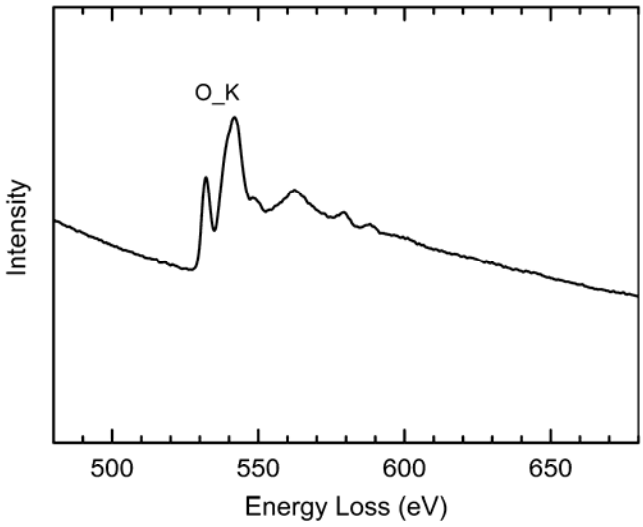

Fig. 2.8 The O K-edge in Fe_2O_3 showing the ample fine features in the ELNES region due to solid state effects.

Beyond the ELNES, there may also be weak extended oscillations. These are known as the extended energy loss fine structure (EXELFS). For an inelastic scattering event in this region, the ejected core electron has a high kinetic energy and can be considered as a free electron. The electron wavefunction is an outgoing spherical wave originating from the excited atom. This outgoing wave will be reflected by neighboring atoms. The interference between the outgoing and backscattered waves, being either constructive or destructive, perturbs the core state wavefunction of the central atom and gives rise to the EXELFS [3]. The EXELFS is a useful tool to measure bond lengths and short-range ordering in solids. The ionization edges, including both the ELNES and EXELFS, are the most useful parts in an EELS spectrum to retrieve information of local

chemistry in a material, such as composition, valences of atoms, coordinations and bond lengths.

If a sufficiently large collection aperture is used, the Compton profile can present, as we discussed in section 2.2.3. The Compton profile can also be used for bonding determination [13].

2.4 Spectrum processing for quantitative analysis

2.4.1 Extracting the single scattering distribution

Despite how thin the specimen is, plural scattering is always possible. The primary electron can undergo a series of inelastic scatterings before it is recorded in the spectrometer and its total energy loss may be equal to the loss of energy in several single inelastic scattering events. This creates artifacts and prevents direct interpretation of spectral features and must be removed [5].

The most reliable and versatile techniques to remove the plural scattering from experimental EELS data involve deconvolution of a spectrum by using Fourier transform. There are two methods, the Fourier-log method and the Fourier-ratio method, and both are widely used.

The possibility of an incident electron experiencing n inelastic scattering events obeys the Poisson statistics. Assuming the total incident beam intensity is I, the intensity I_0 of n-fold inelastically scattered electrons is

$$I_n = I\left(\frac{t}{\lambda}\right)^n \frac{\exp\left(-\frac{t}{\lambda}\right)}{n!}, \tag{2.25}$$

where t is the sample thickness and λ is the total mean free path for all inelastic scattering processes. For $n = 0$,

$$I_0 = I\exp\left(-\frac{t}{\lambda}\right) \tag{2.26}$$

which represents the absence of inelastic scattering and corresponds to the ZLP in the spectrum. For $n = 1$,

$$I_1 = I\left(\frac{t}{\lambda}\right)\exp\left(-\frac{t}{\lambda}\right) = I_0\left(\frac{t}{\lambda}\right). \tag{2.27}$$

I_1 can also be obtained by integrating the intensity distribution of single inelastic scatterings $s_1(\Delta E)$ over all energy loss,

$$I_1 = \int s_1(\Delta E)d\Delta E\,. \tag{2.28}$$

Similarly, for $n = 2$,

$$I_2 = \int s_2(\Delta E)d\Delta E\,. \tag{2.29}$$

The intensity distribution of double scattering $s_2(\Delta E)$ has an energy dependence of

$$\mathrm{s}_2(\Delta E) = K\cdot \mathrm{s}_1(\Delta E) * \mathrm{s}_1(\Delta E)\,, \tag{2.30}$$

where K is a constant. By Eq. (2.28)-Eq. (2.30), we have the double inelastic scattering intensity as

$$
\begin{aligned}
I_2 &= \int K \cdot \mathrm{s}_1(\Delta E) * \mathrm{s}_1(\Delta E) d\Delta E \\
&= K\left(\int \mathrm{s}_1(\Delta E) d\Delta E\right)\left(\int \mathrm{s}_1(\Delta E) d\Delta E\right). \\
&= K \cdot I_0^2 \left(\frac{t}{\lambda}\right)^2
\end{aligned}
\tag{2.31}
$$

By Eq. (2.25) and Eq. (2.26),

$$
I_2 = I\left(\frac{t}{\lambda}\right)^2 \frac{\exp\left(-\frac{t}{\lambda}\right)}{2!} = I_0\left(\frac{t}{\lambda}\right)^2 \frac{1}{2!}. \tag{2.32}
$$

Equating Eq. (2.31) and Eq. (2.32), we have

$$
K = \frac{1}{2! I_0}. \tag{2.33}
$$

Hence,

$$
\mathrm{s}_2(\Delta E) = \frac{1}{2! I_0} \mathrm{s}_1(\Delta E) * \mathrm{s}_1(\Delta E). \tag{2.34}
$$

Similarly, $s_n(\Delta E)$ is obtained as

$$
s_n = \frac{1}{n! I_0^{n-1}} \underbrace{s_1(\Delta E) * s_1(\Delta E) \cdots * s_1(\Delta E)}_{n \text{ terms}}. \tag{2.35}
$$

The recorded spectrum $s_T(\Delta E)$ is the sum of all n-fold scattering distributions,

$$
\begin{aligned}
s_T(\Delta E) &= \sum_n s_n(\Delta E) \\
&= I_0 + s_1(\Delta E) + \frac{1}{2! I_0} \mathrm{s}_1(\Delta E) * \mathrm{s}_1(\Delta E) \cdots \\
&= I_0 \left(1 + \frac{1}{I_0} s_1(\Delta E) + \frac{1}{2! I_0^2} \mathrm{s}_1(\Delta E) * \mathrm{s}_1(\Delta E) \cdots\right)
\end{aligned}
\tag{2.36}
$$

Applying a Fourier transformation to both sides,

$$S_T(\omega) = I_0\left(1 + \frac{1}{I_0}S_1(\omega) + \frac{1}{2!I_0^2}S_1^2(\omega) + \cdots\right)$$
$$= I_0\sum_n \frac{1}{n!}\left(\frac{S_1(\omega)}{I_0}\right)^n \quad . \tag{2.37}$$
$$= I_0 \exp\left(\frac{S_1(\omega)}{I_0}\right)$$

We have,

$$S_1(\omega) = I_0 \ln\left(\frac{S_T(\omega)}{I_0}\right). \tag{2.38}$$

where the upper-case symbols represent the Fourier transform of the corresponding terms in energy space, and the frequency ω is in units of eV^{-1}.

The above derivation assumes an energy resolution of a δ function. A real EELS spectrum contains energy spreading. The recorded data is the sum of all plural scattering distributions convoluted with a instrument broadening function $r(\Delta E)$ [7]. Eq. (2.36) should be corrected as

$$s_T(\Delta E) = I_0 r(\Delta E) * \left(1 + \frac{1}{I_0}s_1(\Delta E) + \frac{1}{2!I_0^2}s_1(\Delta E) * s_1(\Delta E)\cdots\right)$$
$$= s_0(\Delta E) * \left(1 + \frac{1}{I_0}s_1(\Delta E) + \frac{1}{2!I_0^2}s_1(\Delta E) * s_1(\Delta E)\cdots\right) \tag{2.39}$$

where $s_0(\Delta E)$ is the elastic scattering distribution and is essentially the ZLP. Consequently, Eq. (2.38) is modified as

$$S_1(\omega) = I_0 \ln\left(\frac{S_T(\omega)}{S_0(\omega)}\right). \tag{2.40}$$

I_0 is unknown, but it is not of importance because it is just a coefficient and will not affect the shape of the spectrum. The factors, $S_T(\omega)$ and $S_0(\omega)$ are readily obtainable from the experimental data. By applying an inverse Fourier transform on Eq. (2.40), the single scattering distribution $s_1(\Delta E)$ can be retrieved. This procedure to remove the plural scattering is the so-called "Fourier-log method."

The simpler "Fourier-ratio method" is only used to remove the influence of low loss processes from the high loss region. The recorded high loss region is distorted by the low loss part as

$$s_T(\Delta E_{high}) = s_1(\Delta E_{high}) * s_T(\Delta E_{low}), \tag{2.41}$$

where $s_T(\Delta E_{high})$ and $s_T(\Delta E_{low})$ are the experimental high-loss and low-loss regions, respectively. Applying a Fourier transformation to both sides, we have

$$S_T(\omega_{high}) = S_1(\omega_{high}) \cdot S_T(\omega_{low}). \tag{2.42}$$

The single scattering distribution of the high loss region is given by applying inverse Fourier transform on the following equation,

$$S_1(\omega_{high}) = \frac{S_T(\omega_{high})}{S_T(\omega_{low})}. \tag{2.43}$$

2.4.2 Background subtraction

The background under an edge in an EELS spectrum comes mainly from the tails of plasmon excitations and ionization edges with lower threshold energies. In the high

loss region, the background intensity I_b exhibits approximately a power-law energy dependence [7],

$$I_b = A\Delta E^{-r}, \tag{2.44}$$

where A and r are constants. A is not of importance as it is the amplitude and can be chosen arbitrarily to match the experimental data. The optimal value of r, which determines the behavior of the function, is critical for a reliable background fitting. The determination of r is largely an empirical procedure. A reasonable fitting should closely approximate the region before the edge and should extend well beyond the edge without intersecting the spectrum, as shown in Fig. 2.9.

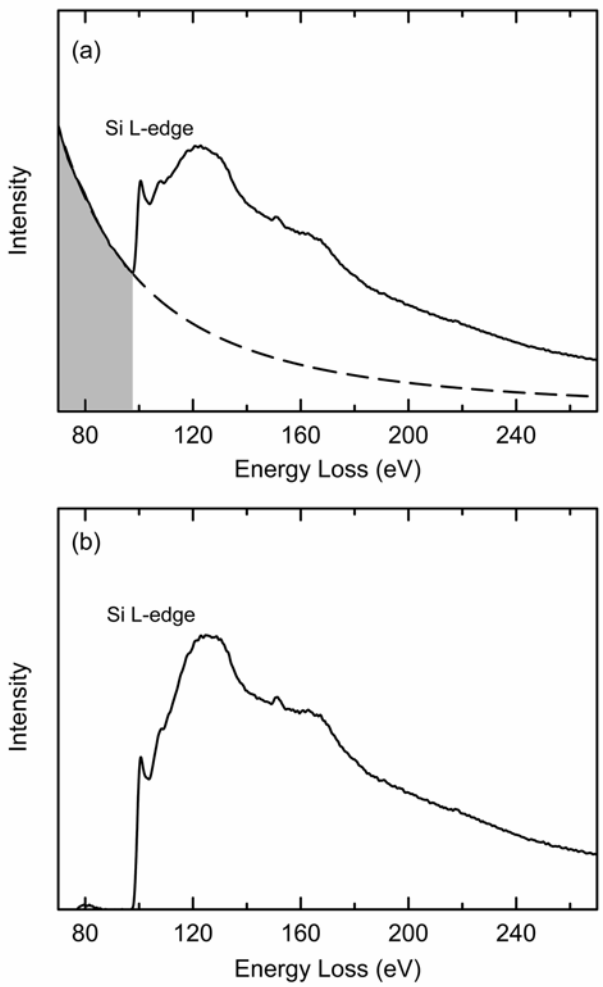

Fig. 2.9 (a) The power-law background model (dashed line) used to remove the background under Si L-edge (solid line). The pre-edge fitting window is shaded in gray. (b) The Si L-edge after background removal.

References

[1] Hammond, C. *The Basics of Crystallography and Diffraction*; Oxford Science: Oxford, 1997.

[2] Brydson, R. *Electron Energy Loss Spectroscopy*; BIOS Scientific: Oxford, 2001.

[3] Fultz, B.; Howe, J. *Transmission Electron Microscopy and Diffractometry of Materials*; Springer-Verlag: New York, 2002.

[4] Rez, P. "Elastic scattering of electrons by atoms." In *Electron-Beam Interactions with Solids*; SEM Inc.: Chicago, 1984.

[5] Reimer, L. *Transmission Electron Microscopy: Physics of Image Formation and Microanalysis*; Springer-Verlag: New York, 1997.

[6] Inokuti, M. *Rev. Mod. Phys.* 1971, 43, 297.

[7] Egerton, R. F. *Electron Energy-Loss Spectroscopy in the Electron Microscope*; Plenum Press: New York, 1996.

[8] Brydson, R. *EMSA Bull.* 1991, 21, 2.

[9] Rez, P.; Weng, X. D.; Hong, M. *Microsc. Microanal. M.* 1991, 2, 143.

[10] Ahn, C. C. *Transmission Electron Energy Loss Spectrometry in Materials Science and the EELS Atlas*; WILEY-VCH: Hoboken, 2004.

[11] Schamm, S.; Zanchi, G. *Ultramicroscopy* 2003, 96, 559.

[12] Leapman, R. D.; Rez, P.; Mayers, D. F. *J. Chem. Phys.* 1980, 75, 1232.

[13] Williams, B. G.; Sparrow, T. G.; Egerton, R. F. *Proc. R. Soc. Lond.* 1984, A393, 409.

Chapter 3

Local Electronic Structure of $Li_xNi_{0.5}Mn_{0.5}O_2$ and $Li_xNi_{1/3}Mn_{1/3}Co_{1/3}O_2$

3.1 Introduction

Cathodes of $LiCoO_2$ with a layered structure have been most successful for service in rechargeable Li-ion batteries [1]. The insertion of Li between CoO_2 layers allows the composition, x, in Li_xCoO_2 to vary reversibly from 1.0 to approximately 0.5 for many cycles [2]. Cycling to lower values of x, corresponding to increased charge of the cell, causes a loss of reversible capacity, perhaps associated with the formation of a monoclinic phase near x = 0.55 [3-5]. The substitution of other transition metals for Co atoms has proved a useful approach for increasing the electrochemical capacity by allowing a larger compositional range for the reversible insertion and extraction of Li [6-8]. Additional benefits of Ni or Mn substitutions for Co include reduced cost of the material, improved thermal stability, and environmental friendliness [9, 10].

The lithiation reaction in layered Li_xCoO_2,

$$(1-x)Li^+ + Li_x^+(CoO_2)^{-x} \rightarrow Li^+(CoO_2)^- - (1-x)e^-, \qquad (3.1)$$

requires the host framework to compensate the charge of the Li^+ ion as it is inserted or extracted. It is tempting to assume that the oxygen remains as O^{2-} and ascribe the charge compensation to the reduction of Co^{4+} to Co^{3+} during lithium insertion. Recent work has shown, however, that the O atoms themselves play the dominant role in charge compensation during Li^+ insertion and extraction [11-13]. The Co atoms undergo little change in valence. A similar behavior was found for the layered form of $LiNi_{0.8}Co_{0.2}O_2$, although there was a suggestion that the Ni atoms may also accommodate some of the charge associated with lithiation [14].

Recently it has been argued that the situation is quite different for $LiNi_{0.5}Mn_{0.5}O_2$ and $LiNi_{1/3}Mn_{1/3}Co_{1/3}O_2$ with the same layered structure as $LiCoO_2$. The charging behavior of cells with $LiNi_{0.5}Mn_{0.5}O_2$ was interpreted as evidence for Ni^{2+} to Ni^{4+} oxidation [7], and peaks in cyclic voltammetry measurements at 3.7-4.0 V were interpreted as evidence for a Ni^{2+}/Ni^{4+} redox process [15]. Changes in the spin density obtained from electronic structure calculations were used to deduce a Ni^{2+} to Ni^{4+} transition during lithium extraction [16, 17]. A clear shift of the Ni K-edge was observed in X-ray absorption near-edge spectra (XANES). This shift and the change in the Ni-O bond lengths were attributed to the oxidation from Ni^{2+} to Ni^{4+} during delithiation [18-20]. Due to the dipole selection rules, the Ni K-edge is not the optimum edge to investigate the occupancy of Ni 3d and O 2p states; transition metal L-edges are more informative. The sharp white lines

that appear at the $L_{2,3}$ absorption edges have proved to be useful as experimental probes of changes of Ni valence [14, 21, 22]. White lines originate primarily with the excitation of inner 2p electrons to unoccupied 3d states at the same atom (alternatively stated as the 3d character of the lowest unoccupied molecular orbitals or the projected density of 3d states at the transition metal atom). The intensity of the white lines increases with the number of unoccupied 3d states, and the central energies of the white lines undergo shifts with changes in the energy levels of 2p or 3d electrons. Recent experimental results from X-ray near-edge structure and transmission electron energy loss spectrometry reported changes in the shape and positions of the white lines at the $L_{2,3}$ absorption edges of Ni, and none at Mn atoms, during lithiation of the material [23, 24]. These results were presented as evidence for the Ni^{2+} to Ni^{4+} transition during delithiation. Similar work and interpretations were reported for the Co-doped variant, $LiNi_{1/3}Mn_{1/3}Co_{1/3}O_2$ [25-27]. On the basis of cyclic voltammetry measurements, the redox process around 3.8 V was assigned to the Ni^{2+}/Ni^{4+} redox couple [25]. Band structure and electron density calculations also supported a Ni^{2+}/Ni^{4+} redox reaction during the lithium insertion and extraction process [26, 27].

Despite this substantial literature arguing for the Ni^{2+} to Ni^{4+} redox process during Li extraction from $LiNi_{1/3}Mn_{1/3}Co_{1/3}O_2$, some inconsistencies remain [7, 15-20, 23-27]. First, during delithiation, only small changes in the intensities and positions of the white lines at the Ni $L_{2,3}$ edges are measured. Larger changes are generally observed during

oxidation of transition metals [28]. Second, the electrochemical capacity and voltage do not scale as expected with the amount of Ni in the material. Finally, the electronic structure calculations relied on an integrated spin density around the Ni atoms, but changes in spin density do not necessarily correlate with changes in charge density.

Here we report results from a new computational effort to assess the effects of the Ni^{2+} to Ni^{4+} transition on the white lines at the Ni L-edges that we measured in a new experimental effort using electron energy loss spectrometry. The experimental spectra were consistent with the results reported by others, but the atomic multiplet calculations showed that the shifts at the Ni L-edges were too small to be associated with the formation of Ni^{4+}. Changes in white lines intensities during delithiation were also too small to account for Ni^{4+}. We conclude that the Ni^{2+} to Ni^{4+} redox process does not occur during delithiation. This is consistent with our charge density calculations showing that ionic charge cannot be inferred from calculated spin densities. Charge compensation during lithiation occurs primarily at hybridized 2p states associated with O atoms.

3.2 Experimental

To prepare the compound $LiNi_{0.5}Mn_{0.5}O_2$, $Ni_{0.5}Mn_{0.5}(OH)_2$ (by Tanaka Chemicals Inc.) was fired at 400 °C for 5 h in air to obtain $Ni_{0.5}Mn_{0.5}O$. The $Ni_{0.5}Mn_{0.5}O$ was well mixed with $Li(OH)\cdot(H_2O)$ in a stoichiometric ratio, and $LiNi_{0.5}Mn_{0.5}O_2$ was obtained by

firing this mixture at 1000 °C for 24 h in air. The $LiNi_{1/3}Mn_{1/3}Co_{1/3}O_2$ powder was provided by Enax Inc.

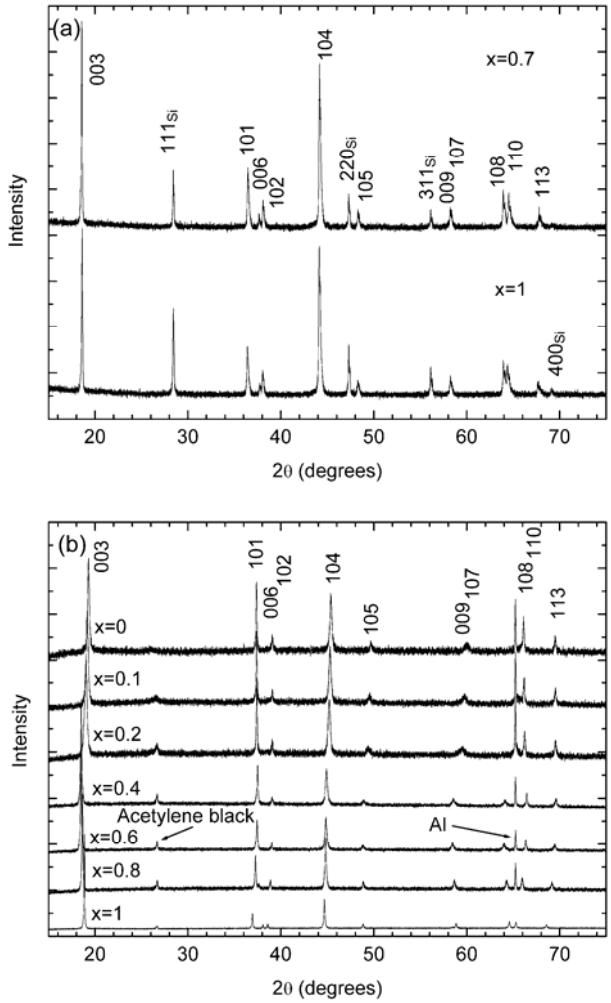

Fig. 3.1 Indexed X-ray powder diffraction patterns from samples of different states of lithiation (a) $Li_xNi_{0.5}Mn_{0.5}O_2$ (with Si as an internal standard) and (b) $Li_xNi_{1/3}Mn_{1/3}Co_{1/3}O_2$.

An acetone solution containing 80 wt % $LiNi_{0.5}Mn_{0.5}O_2$ (or $LiNi_{1/3}Mn_{1/3}Co_{1/3}O_2$), 12 wt % acetylene black, and 8 wt % PVDF (polyvinylidene fluoride) was deposited on an aluminum foil and dried for 1 day in air to make electrodes for 2016 coin cells. The cells

used Li metal counter electrodes, 1 mol $LiPF_6$/EC-DMC (ethylene carbonate – dimethyl carbonate) as the electrolyte and microporous polypropylene Celgard 3401 as the separator. Lithium extraction was achieved by charging the cell until the charging capacity equaled (1-x), where $x \leq 1$, of the theoretical capacity. Hence, the general formulas for the materials can be expressed as $Li_xNi_{0.5}Mn_{0.5}O_2$ (x = 0.7 and 1) and $Li_xNi_{1/3}Mn_{1/3}Co_{1/3}O_2$ (x = 0, 0.1, 0.2, 0.4, 0.6, 0.8, and 1), respectively. We refer to samples with x = 1 as "lithiated", and all other samples as "partially delithiated".

The structures of all samples were determined by X-ray diffraction (XRD) performed with a Philips X'Pert powder diffractometer using Cu Kα radiation (λ = 0.15046nm). Indexed X-ray diffraction patterns are presented in Fig. 3.1. All patterns are indexed well with space group $R\bar{3}m$, and the measured lattice constants are summarized in Table 3.1.

Table 3.1 Lattice constants of Li_xMO_2

	a (nm)	c (nm)	c/a
$Li_1Ni_{1/3}Mn_{1/3}Co_{1/3}O_2$	0.2861	1.4094	4.926
$Li_{0.8}Ni_{1/3}Mn_{1/3}Co_{1/3}O_2$	0.2834	1.4259	5.031
$Li_{0.6}Ni_{1/3}Mn_{1/3}Co_{1/3}O_2$	0.2820	1.4381	5.100
$Li_{0.4}Ni_{1/3}Mn_{1/3}Co_{1/3}O_2$	0.2816	1.4366	5.101
$Li_{0.2}Ni_{1/3}Mn_{1/3}Co_{1/3}O_2$	0.2824	1.3991	4.955
$Li_{0.1}Ni_{1/3}Mn_{1/3}Co_{1/3}O_2$	0.2830	1.3873	4.903
$Li_0Ni_{1/3}Mn_{1/3}Co_{1/3}O_2$	0.2832	1.3776	4.864
$Li_1Ni_{0.5}Mn_{0.5}O_2$	0.2892	1.4286	4.940
$Li_{0.7}Ni_{0.5}Mn_{0.5}O_2$	0.2887	1.4317	4.960

Electrochemical cells were cycled two to three times between 3 and 4.5 V and held at a fixed state of charge for 5 h before they were disassembled in an Ar glovebox. The cathodes were removed and crushed with a mortar and pestle in 1-methyl-2-pyrrolidinone. Fine particles were then dispersed onto holey carbon grids for transmission electron microscopy (TEM) analysis. In selected regions of the sample, beam damage to the specimen was monitored in image, diffraction, and spectroscopy modes. Under the most intense electron illumination conditions, there was no observable change in image contrast, diffuseness of diffraction pattern, and spectral features for at least 10 min, sufficiently long to acquire electron energy loss spectrometry (EELS) data. The EELS spectra were acquired with a Philips EM420 transmission electron microscope operated at 100 kV with a Gatan 666 parallel EELS spectrometer. The spectra were acquired in image mode (diffraction coupling), with a typical area of analysis of 104 nm^2.

Approximately a half-dozen particles were analyzed for each sample to assess the effect of compositional heterogeneity during charging. The statistical variations in their spectral results were used to obtain error bars in the figures below. The energy resolution was approximately 1.5 eV with an energy dispersion of 0.5 eV per channel. A large collection angle of ~100 mrad was used to include the spectral contributions from the entire Bethe ridge [29]. Since 1024 channels in the spectrometer cannot cover an energy range 0-950 eV in a single acquisition, the low-loss and high loss-parts were collected

separately. The two parts were then spliced with an overlapping portion. This manipulation could introduce a small spectral shift of high-loss part. All spectra were therefore aligned with the Mn L-edges for which no change occurred during delithiation [7, 15-20, 23, 25-27]. The experimental spectra were deconvoluted using a Fourier-log method to remove the plural scattering [30]. A power-law fit to the pre-edge background was performed for each ionization edge, and the estimated background was then subtracted from the data [31].

3.3 Computational

Calculations of the electronic structure were performed for a two-formula unit cell for both $Li_2(NiMn)O_4$ (x = 1) and $Li(NiMn)O_4$ (x = 0.5). The initial structure was taken from the $R\bar{3}m$ layered structure transformed to a monoclinic cell with symmetry *C2/m*. The VASP [32, 33] (Vienna ab initio simulation program) code was used with projector augmented wave (PAW) potentials in the generalized gradient approximation (GGA). The calculations were based on the local spin density approximation, and the magnetic moments were initially set to three unpaired electrons for Mn and two for Ni in an antiferrimagnetic arrangement. A dense $5\times10\times5$ k point grid was used (convergence having been checked using larger grids), which gave 78 k points in the irreducible wedge. Full relaxation of both the unit cell and the atomic positions was allowed, and the energy was converged to 0.001 eV/atom. For density of states calculations, the atom positions

were taken from a converged calculation and the k point grid was increased to $6 \times 12 \times 6$, which gave 140 k points in the irreducible wedge.

The shapes of transition metal $L_{2,3}$ edges are altered significantly by atomic multiplet effects because there is significant overlap of the radial wave functions for the 2p hole and the holes in the partially filled 3d band. Final states must be calculated by vector coupling the 2p and 3d wave functions. This strong, purely atomic, effect is only partly screened in the solid state, meaning that features in spectra are comparable for solids and isolated atoms. The initial and final states are specified as a sum of terms in the LS coupling scheme. For example for Ni^{2+} the initial state configuration would be $2p^6 3d^8$ and the final state $2p^5 3d^9$. The initial ground state $^3F_4$ is given by Hund's rule. Transitions calculated with a dipole selection rule give ΔJ as -1, 0, 1. In this case there are 12 terms allowed for the final state. The strengths of the various transitions are calculated from the appropriate matrix elements from the Hamiltonian

$$H = \sum_N \frac{p_i^2}{2m} + \sum_N \frac{-Ze^2}{r_i} + \sum_{pairs} \frac{e^2}{r_{ij}} + \sum_N \xi(r_i) l_i s_i \,. \tag{3.2}$$

Since the first two terms of this Hamiltonian are the same for all electrons in a configuration, only the last two terms, the electron-electron interaction and the spin-orbit coupling, need to be considered. In practice for transition element ions it has been found

necessary to reduce the pd exchange integrals by 20% from the values calculated using the Hartree-Fock wave functions.

The oxygen atoms neighboring the transition metal ion add a crystal field that is represented as a sum of spherical harmonics and can be treated as a perturbation to the atomic multiplet calculation. The main effect is to change the local symmetry from spherical to octahedral. Calculations of some transition metal white line intensities in octahedral and tetrahedral symmetry are given by Van der Laan and Kirkman [34]. Following this approach, we determined the crystal field parameter 10 Dq from the splitting of the t_{2g} and e_g parts of the electronic density of states. For a detailed description of multiplet theory applied to inner shell spectroscopy, see the recent review by de Groot [35], whose codes were used in the present work.

3.4 Results

3.4.1 EELS

White lines at transition metal L-edges originate from electronic transitions from core 2p states to unoccupied states that differ by 1 in angular momentum quantum number. Their intensity is dominated by the presence of unoccupied 3d states projected at Ni, Mn, and Co atoms. Fig. 3.2 and Fig. 3.3 show pairs of prominent white lines at the Mn and Co $L_{2,3}$ edges. For Mn and Co, there is essentially no difference in the white lines for the

lithiated and partially delithiated samples. Intensity variations of less than 3% for Mn and less than 5% for Co were observed, but these did not correlate well to the state of lithiation. We therefore cannot detect any change in valence at Mn or Co atoms during delithiation.

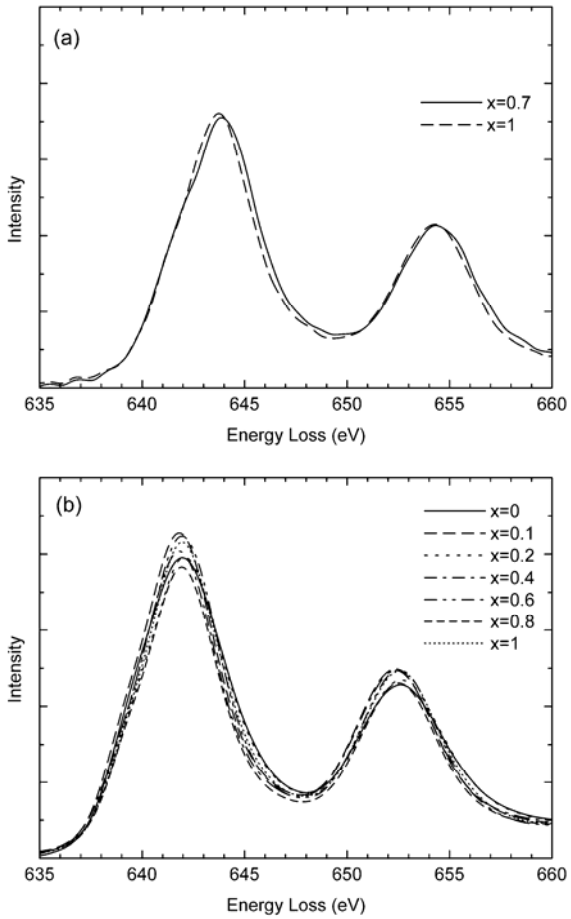

Fig. 3.2 Mn $L_{2,3}$ white lines from (a) $Li_xNi_{0.5}Mn_{0.5}O_2$ and (b) $Li_xNi_{1/3}Mn_{1/3}Co_{1/3}O_2$ with different x values. The spectra were normalized with a 50 eV window after the L_2 peak.

Fig. 3.4 shows the white lines at the Ni $L_{2,3}$ edges. There are changes in white line shape, position, and intensity with changes in lithium concentration. With delithiation, there is a broadening and upward shift of the white lines and a small variation in intensity. These changes are very similar to the results on layered $LiNi_{0.5}Mn_{0.5}O_2$ reported by Yoon *et*

al. [23] from soft X-ray absorption spectra and by Koyama *et al.* [24] from electron energy loss spectra of Ni L-edges. Fig. 3.5 shows the positions of the Ni L_3 white line from the $Li_xNi_{1/3}Mn_{1/3}Co_{1/3}O_2$ samples. A linear fit shows that the L_3 peak shifts upward less than 1.2 eV when x changes from 1 to 0. Fig. 3.6 shows the change in intensity of the Ni white lines versus Li concentration. The changes in intensity show no obvious trend, indicating no obvious trend in the valence of the Ni atom upon delithiation.

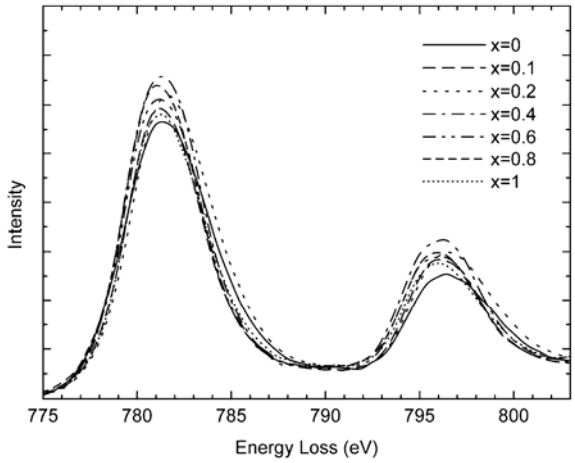

Fig. 3.3 Co $L_{2,3}$ white lines from $Li_xNi_{1/3}Mn_{1/3}Co_{1/3}O_2$ with different x values. The spectra were normalized with a 40 eV window after the L_2 peak.

Fig. 3.7 shows a large change at the O K-edge upon delithiation. The pre-peak at 528 eV (labeled "A") increases in intensity upon delithiation. This pre-peak is dominated by the dipole-allowed 1s to 2p electronic transition and is indicative of the number of unoccupied 2p states projected at the O atom. Lithiation causes a filling of these states. A graph of the normalized O K-edge pre-peak intensities versus Li concentration is shown in Fig. 3.8 for samples of $Li_xNi_{1/3}Mn_{1/3}Co_{1/3}O_2$. A linear fit was made to the delithiated

samples with $x \geq 0.4$ to compare with previous results for $LiCoO_2$ and $LiNi_{0.8}Co_{0.2}O_2$ [13,14]. Although the linear fit is an empirical correlation, the slopes for the three systems, $LiCoO_2$, $LiNi_{0.8}Co_{0.2}O_2$, and $Li_xNi_{1/3}Mn_{1/3}Co_{1/3}O_2$, are very similar, being approximately -0.27, -0.26, and -0.27, respectively. The range of analysis from $0.4 \leq x \leq 1.0$ was selected because the crystal structure of $LiCoO_2$ is known to be stable over this range.

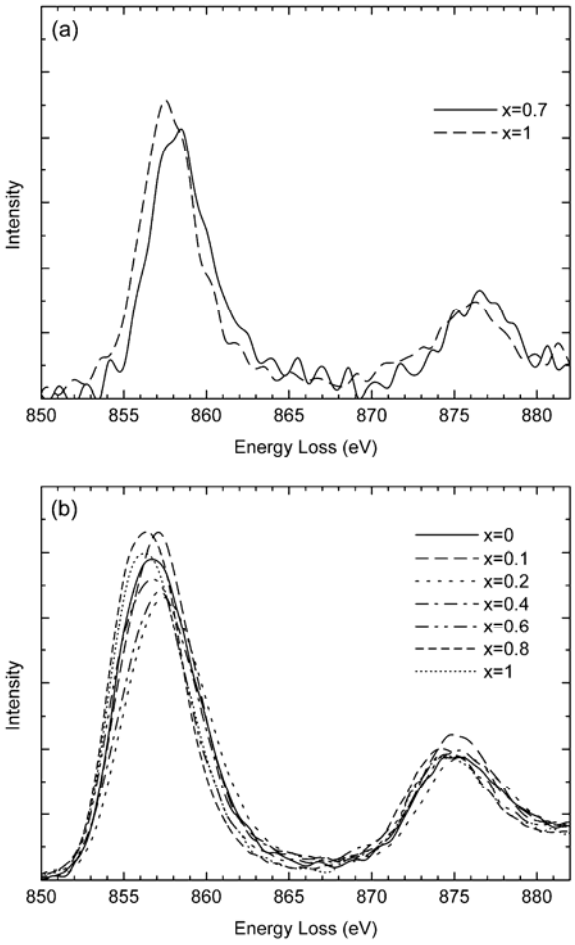

Fig. 3.4 Ni $L_{2,3}$ white lines from (a) $Li_xNi_{0.5}Mn_{0.5}O_2$ and (b) $Li_xNi_{1/3}Mn_{1/3}Co_{1/3}O_2$ with different x values. The spectra were normalized with a 40 eV window after the L_2 peak.

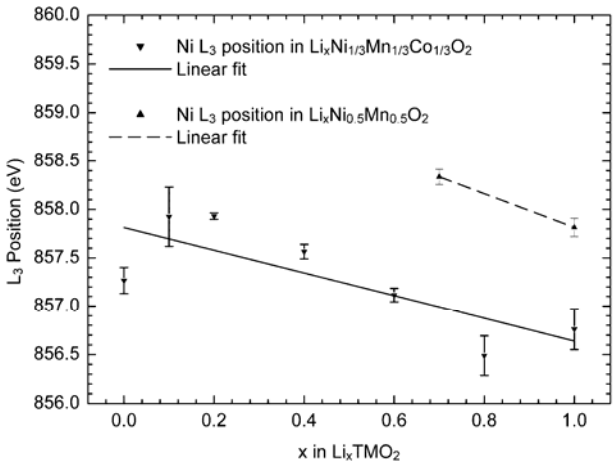

Fig. 3.5 Ni white line L_3 positions of $Li_xNi_{0.5}Mn_{0.5}O_2$ and $Li_xNi_{1/3}Mn_{1/3}Co_{1/3}O_2$ with different Li content, x.

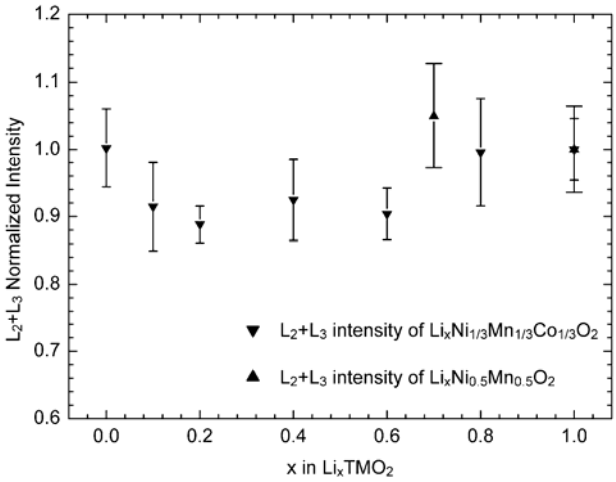

Fig. 3.6 Ni $L_{2,3}$ white line intensities of $Li_xNi_{0.5}Mn_{0.5}O_2$ and $Li_xNi_{1/3}Mn_{1/3}Co_{1/3}O_2$ with different Li content, x. The intensity is normalized to the fully lithiated sample with x = 1.

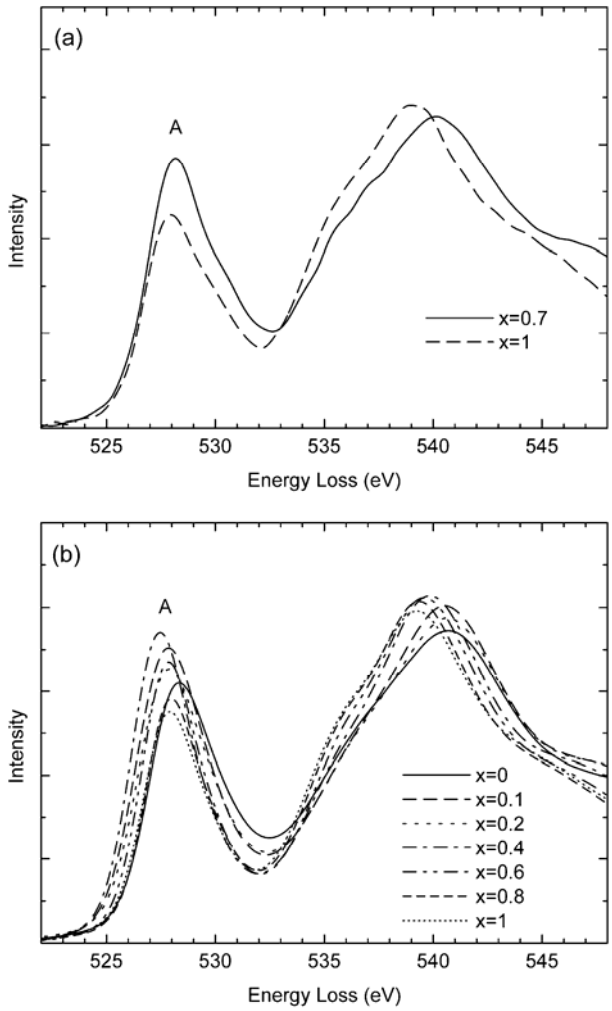

Fig. 3.7 O K-edge from (a) $Li_xNi_{0.5}Mn_{0.5}O_2$ and (b) $Li_xNi_{1/3}Mn_{1/3}Co_{1/3}O_2$ with different x values. The spectra were normalized with the main peak (532-543 eV) to show the intensity of the pre-peak.

3.4.2 Electronic structure calculations

For the fully lithiated $LiNi_{0.5}Mn_{0.5}O_2$ compound, the unit cell was found to be monoclinic (*P2/m*) with a = 5.119 Å, b= 2.876 Å, c = 5.067 Å and $\gamma = 110.42°$ with a net magnetic moment corresponding to one unpaired electron. The fully relaxed half-lithiated cell was also monoclinic (*P2/m*) with a = 4.907 Å, b = 2.89 Å, c = 5.253 Å and $\gamma = 109.26°$

with a net magnetic moment corresponding to two unpaired electrons. The reduction in symmetry from that of the starting configuration is due to the Jahn-Teller distortion [17,36].

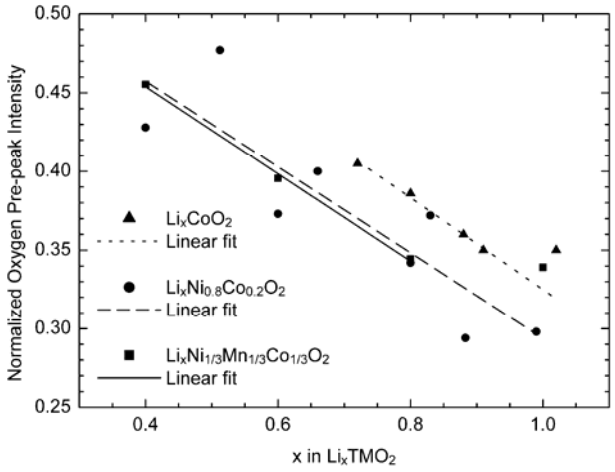

Fig. 3.8 Normalized intensity of pre-peak at O K-edge of Li_xCoO_2, $Li_xNi_{0.8}Co_{0.2}O_2$, and $Li_xNi_{1/3}Mn_{1/3}Co_{1/3}O_2$, showing trends with delithiation. The pre-peak intensity (524-532 eV) is normalized to the main peak intensity (532-543 eV). The atomic cross sections were divided out of the experimental data.

Fig. 3.9 shows the spin density contained within spheres of different radii around Ni and Mn atoms at two states of lithiation. The results are similar to those obtained by Reed and Ceder [16], but the signs of the spins are plotted here to show the antiferrimagnetism of the structure. With delithiation there is a decrease in the spin density around Ni atoms of about 0.75 μ_B over a wide range of radii in Fig. 3.9. The spin density reaches a maximum at a distance of less than 1 Å, indicating that the loss of spin occurs on the Ni atom. There is no such change at Mn atoms.

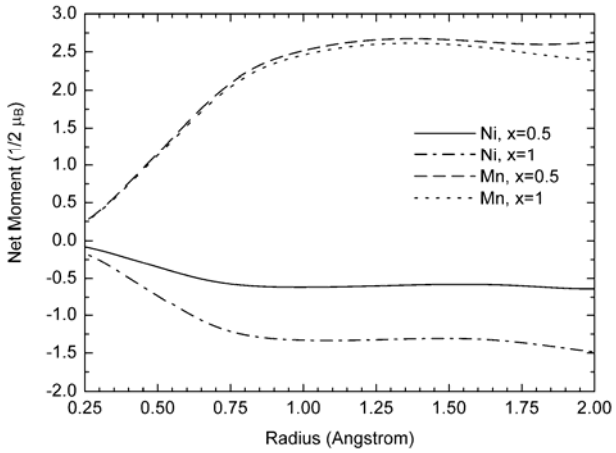

Fig. 3.9 Spin contained within spheres of radius about the Ni atom in $LiNi_{0.5}Mn_{0.5}O_2$ and $Li_{0.5}Ni_{0.5}Mn_{0.5}O_2$.

The charge density within spheres of different radii around Ni and Mn atoms is presented in Fig. 3.10. As expected, the charge density increases with sphere radius. Even if the absolute charge associated with a particular atom is somewhat arbitrary, it is still meaningful to investigate changes in charge with Li concentration over a range of radii up to 1.4 Å, which corresponds to spheres touching in the transition metal layer. At both Ni and Mn atoms there is a small increase in the charge density with delithiation. The larger radii will include electrons associated with O atoms, so interpretation of Fig. 3.10 is not so straightforward as for Fig. 3.9. Note that the pseudopotential accounts for an Ar core of 18 electrons, so the 8 extra electrons for Ni^{2+} would correspond to a radius of about 1 Å, which is half the Ni-O bond distance. Note that the charge density about the Ni atom in Fig. 3.10 is not consistent with the charge inferred from the spin density of Fig. 3.9.

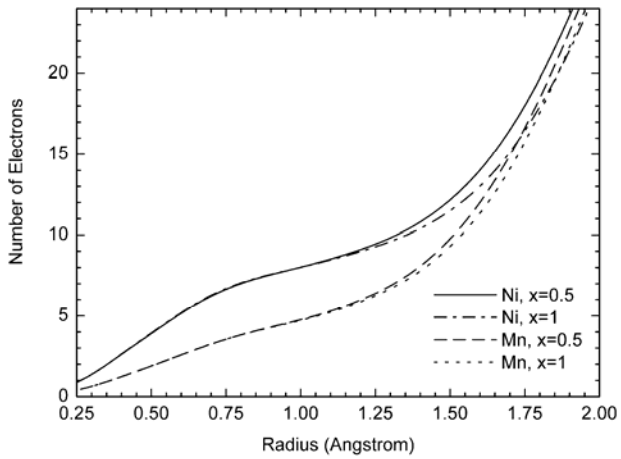

Fig. 3.10 Valence charge contained within spheres of radius about the Ni atom in $LiNi_{0.5}Mn_{0.5}O_2$ and $Li_{0.5}Ni_{0.5}Mn_{0.5}O_2$.

Electronic structure calculations performed with WIEN2K [37] gave similar results for the charge and spin density about the Ni and Mn atoms. A very small increase in the charge density at Ni and Mn atoms was found upon delithiation, corresponding to less than 0.1 electron. The magnetic moment at the Mn atom was the same value of 2.5 μ_B for both x=1.0 and x = 0.5, whereas the magnetic moment at the Ni atom decreased from 1.26 to 0.61 μ_B between x = 1.0 and x = 0.5.

Densities of states from VASP calculations for $LiNi_{0.5}Mn_{0.5}O_2$ were used to estimate a value of 1.6 eV for the crystal field parameter 10 Dq from the separation of the t_{2g} and e_g levels [35]. This was used in the crystal field multiplet calculations for Ni^{2+}, Ni^{3+}, and Ni^{4+}. The results are shown in Fig. 3.11. There is a mean shift of the white line to higher energies by 3 eV for Ni^{4+} that should be easily detectable in the experimental EELS measurements.

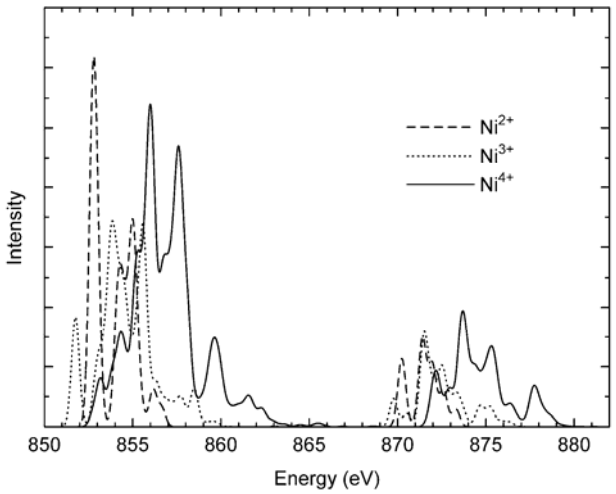

Fig. 3.11 Atomic multiplet calculation of Ni $L_{2,3}$ white lines using crystal field information from VASP. Compared to Ni^{2+}, the shift of the average L_3 white line is 3 eV for Ni^{4+}, inconsistent with the experimental result of Fig. 3.4.

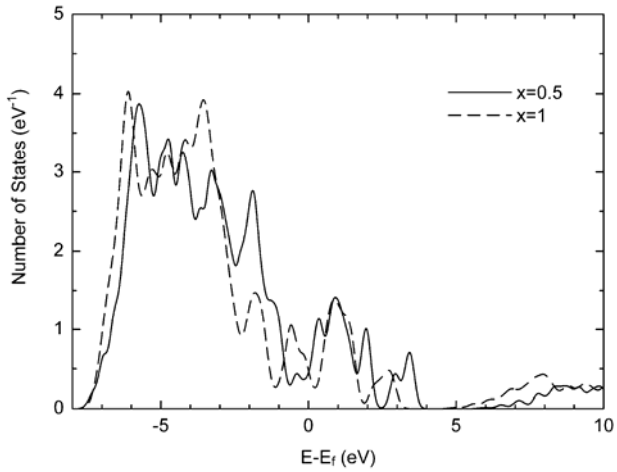

Fig. 3.12 VASP calculation of of oxygen p partial density of states of $Li_xNi_{0.5}Mn_{0.5}O_2$. The intensity from 0 to 4 eV above the Fermi level (E_f) corresponds to the intensity in the experimental pre-peak. The integrated DOS from the Fermi level is 30% more for x = 0.5.

Results calculated with VASP for the O K-edge pre-peak, presented in Fig. 3.12, are in good correspondence with the changes shown in the experimental data in Fig. 3.8. The calculated peak located from 0 to 4 eV above the Fermi level corresponds to the

experimental pre-peak at 528 eV. The integrated DOS in this region increases by 30% on delithiation, in agreement with the experimental measurement.

3.5 Discussion

No systematic trend was found in the change of the white line intensities of Mn and Co atoms during delithiation, consistent with previous results [23-27]. The variations of the white line intensities allow for some small changes in the numbers of 3d electrons at Mn and Co atoms, but these changes can be only ± 0.05 electrons at Mn and Co atoms per lithium atom inserted or extracted. We also have preliminary results from an investigation of lithium removal in $Li_3NiMnCoO_6$ (a three-formula unit cell) where the transition metals are ordered as rows in a single layer. Charge densities of Ni, Mn and Co as a function of radius show minimal change with removal of a single Li atom which gives a stoichiometry $Li_{2/3}Ni_{1/3}Mn_{1/3}Co_{1/3}O_2$. This result does not depend on which one of three Li atoms is removed from the fully lithiated model cell.

Observable changes in the measured Ni $L_{2,3}$ white lines upon delithiation are seen in Fig. 3.4. The upward shift shown in Fig. 3.5 is representative of some change in electronic structure, but it is small. Atomic multiplet calculations with an octahedral crystal field show (see Fig. 3.11) that for a change from Ni^{2+} to Ni^{4+}, this shift should be 3 eV, and the L_2 edge should grow at the expense of the L_3 edge. The upward shift of 3 eV obtained

for a Ni^{2+} to Ni^{4+} transition during lithium extraction is clearly inconsistent with the measured EELS spectrum of Fig. 3.4.

The normalized Ni white line intensities of the $Li_xNi_{1/3}Mn_{1/3}Co_{1/3}O_2$ samples are shown in Fig. 3.6. The intensities vary randomly within $\pm$ 7% of an average value. This variation corresponds approximately to a charge transfer only about 0.21 electron per Ni atom, assuming three empty 3d orbitals of Ni^{2+} in the lithiated material. Considering only 1/3Ni in one formula unit, this puts an upper bound on the total charge transfer from Ni of 0.07 electron per Li atom.

Fig. 3.11 indicates that a Ni^{2+} to Ni^{3+} transition should cause a shift of approximately 0.7 eV at the L_3 edge, and this seems consistent with the experimental results of Fig. 3.4 and Fig. 3.5. Nevertheless, a Ni^{2+} to Ni^{3+} transition caused by the extraction of a Li^+ ion is inconsistent with the bound of 0.07 electron per Li+ ion obtained from the change in intensity of the white lines of Fig. 3.6. An alternative explanation of the shift of the Ni L_3 edge with delithiation could be associated with Ni-Li interlayer mixing [38-43]. Eight percent of such Li/Ni exchange was reported [43], but we do not have data for this on our present materials. Nevertheless, the expected interlayer mixing of Li and Ni atoms would cause heterogeneity in the local environments of Ni atoms. This heterogeneity may change with the state of lithiation, so the observed shifts in Ni white lines could originate with interlayer mixing and not necessarily the formation of Ni^{3+}.

The oxygen pre-peak in Fig. 3.7 shows good correspondence with the calculated 2p DOS shown in Fig. 3.12. The trend with Li concentration (Fig. 3.8) is similar to that found for $LiCoO_2$ and $LiNi_{0.8}Co_{0.2}O_2$ [13,14]. With delithiation, there is a loss of 2p electrons at O atoms. For a specific Li concentration, the O pre-peak intensity is weaker for the material with the largest average atomic number of the transition metal, $LiNi_{0.8}Co_{0.2}O_2$, indicative of a larger transfer of charge from transition metal 3d states to O 2p states. The average intensities for $Li_xNi_{1/3}$ $Mn_{1/3}Co_{1/3}O_2$ and $LiCoO_2$ are similar, as are the average atomic numbers of their transition metals.

The pre-peak intensity for oxygen in the PDOS plot of Fig. 3.12 is indicative of about 2.05 holes in the oxygen 2p states electrons, based on prior work with $LiCoO_2$ [13,14]. Upon delithiation from x = 1 to x = 0.6, the measured pre-peak for $LiNi_{1/3}Mn_{1/3}Co_{1/3}O_2$ grows by about 32%. This is consistent with a loss of electrons about the O atom, and a simple linear interpolation would predict a loss of 0.66 electrons per O atom, or 1.32 electrons per formula unit. This is not accurate quantitatively, but it shows that the change in electron density about the O atoms is substantial and is able to account for much of the charge compensation around a Li^+ ion. The VASP and WIEN2K calculations indicate that the charge is built up as electron density in the interstitial regions between the atoms, consistent with a tendency for charge accumulation around the oxygen atoms.

Changes in the spin density at Ni atoms during delithiation are not necessarily representative of the change in charge density that provides the change in valence. For example, a simple transfer of electrons from 3d up states to 3d down states causes a change of spin, but no change of 3d charge. A comparison of Fig. 3.9 and Fig. 3.10 shows that, unlike the spin density, the charge density about the Ni atoms increases continuously with radius. Especially since the charge density is not isotropic, it is therefore more difficult to define a precise valence based on charge density plots as Fig. 3.10. Nevertheless, even accounting for small changes in lattice parameter upon delithiation, there is a small decrease in the electron density about Ni atoms when the material is delithiated. This is opposite from what is predicted by a Ni^{2+} to Ni^{4+} transition during delithiation.

3.6 Conclusion

Both experimental and computational evidence indicate that most of the compensation for charge during the removal of Li ions from $Li_xNi_{1/3}Mn_{1/3}Co_{1/3}O_2$ and $Li_xNi_{0.5}Mn_{0.5}O_2$ occurs at hybridized 2p-like levels with local weight near oxygen atoms, much as is the case in Li_xCoO_2. All experimental and computational results are inconsistent with the hypothesis of a Ni^{2+} to Ni^{4+} transition during lithium extraction. Although the results on L_3 edge shifts allow for a Ni^{2+} to Ni^{3+} transition, the intensity results do not, and the Ni^{2+} to Ni^{3+} transition is not supported by computational work.

Finally, the trends with lithiation in the spin density at Ni atoms are not representative of the trends in charge density.

References

[1] Mizushima, K.; Jones, P. C.; Wiseman, P. J.; Goodenough, J. B. *Mater. Res. Bull.* 1980, 15, 783.

[2] Nagaura, T. Prog. *Batteries Battery Mater.* 1991, 10, 218.

[3] Reimers, J. N.; Dahn, J. R. *J. Electrochem. Soc.* 1992, 139, 2091.

[4] Ohzuku, T.; Ueda, A. *J. Electrochem. Soc.* 1994, 141, 2972.

[5] Shao-Horn, Y.; Levasseur, S.; Weill, F.; Delmas, C. *J. Electrochem. Soc.* 2003, 150, A366.

[6] Delmas, C.; Saadoune, I. *Solid State Ionics* 1992, 53-56, 370.

[7] Lu, Z. H.; Beaulieu, L. Y.; Donaberger, R. A.; Thomas, C. L.; Dahn, J. R. *J. Electrochem. Soc.* 2002, 149, A778.

[8] Ohzuku, T.; Makimura, Y. *Chem. Lett.* 2001, 642.

[9] Ohzuku, T.; Makimura, Y. *Chem. Lett.* 2001, 744.

[10] Yabuuchi, N.; Ohzuku, T. *J. Power Sources* 2003, 119, 171.

[11] Van der Ven, A.; Aydinol, M. K.; Ceder, G.; Kresse, G.; Hafner, J. *Phys. Rev. B* 1998, 58, 2975.

[12] Wolverton, C.; Zunger, A. *Phys. Rev. Lett.* 1998, 81, 606.

[13] Graetz, J.; Hightower, A.; Ahn, C. C.; Yazami, R.; Rez, P.; Fultz, B. *J. Phys. Chem. B* 2002, 106, 1286.

[14] Graetz, J.; Ahn, C. C.; Yazami, R.; Fultz, B. *J. Phys. Chem. B* 2003, 107, 2887.

[15] Shaju, K. M.; Rao, G. V. S.; Chowdari, B. V. R. *Electrochim. Acta* 2003, 48, 1505.

[16] Reed, J.; Ceder, G. *Electrochem. Solid-State Lett.* 2002, 5, A145.

[17] Islam, M. S.; Davies, R. A.; Gale, J. D. *Chem. Mater.* 2003, 15, 4280.

[18] Yoon, W.-S.; Grey, C. P.; Balasubramanian, M.; Yang, X.-Q.; McBreen, J. *Chem. Mater.* 2003, 15, 3161.

[19] Johnson, C. S.; Kim, J.-S.; Kropf, A. J.; Kahaian, A. J.; Vaughey, J. T.; Fransson, L. M. L.; Edström, K.; Thackeray, M. M. *Chem. Mater.* 2003, 15, 2313.

[20] Nakano, H.; Nonaka, T.; Okuda, C.; Ukyo, Y. *J. Ceram. Soc. Jpn.* 2003, 111, 33.

[21] Pearson, D. H.; Ahn, C. C.; Fultz, B. *Phys. Rev. B* 1993, 47, 8471.

[22] Potapov, P. L.; Kulkova, S. E.; Schryvers, D.; Verbeeck, J. *Phys. Rev. B* 2001, 64, Art. No. 184110.

[23] Yoon, W.-S.; Balasubramanian, M.; Yang, X.-Q.; Fu, Z. G.; Fischer, D. A.; McBreen, J. *J. Electrochem. Soc.* 2004, 151, A246.

[24] Koyama, Y.; Mizoguchi, T.; Ikeno, H.; Tanaka, I. *J. Phys. Chem. B* 2005, 109, 10749.

[25] Shaju, K. M.; Rao, G. V. S.; Chowdari, B. V. R. *Electrochim. Acta* 2002, 48, 145.

[26] Koyama, Y.; Tanaka, I.; Adachi, H.; Makimura, Y.; Ohzuku, T. *J. Power Sources* 2003, 119-121, 644.

[27] Koyama, Y.; Yabuuchi, N.; Tanaka, I.; Adachi, H.; Ohzuku, T. *J. Electrochem. Soc.* 2004, 151, A1545.

[28] Graetz, J.; Ahn, C. C.; Ouyang, H.; Rez, P.; Fultz, B. *Phys. Rev. B* 2004, 69, Art. No. 235103.

[29] Fultz, B.; Howe, J. M. *Transmission Electron Microscopy and Diffractometry of Materials*; Springer: Berlin, 2002; p 192.

[30] Johnson, D. W.; Spence, J. C. H. *J. Phys. D* 1974, 7, 771.

[31] Egerton, R. F. *Electron Energy-Loss Spectroscopy in the Electron Microscope*; Plenum: New York, 1996.

[32] Kresse, G.; Furthmuller, J. *Phys. Rev. B* 1996, 54, 11169.

[33] Kresse, G.; Joubert, D. *Phys. Rev. B* 1999, 59, 1758.

[34] Van der Laan, G.; Kirkman, I. W. *J. Phys.*: *Condens. Matter* 1992, 4, 4189.

[35] de Groot, F. *Coord. Chem. Rev.* 2005, 249, 31.

[36] Marianetti, C. A.; Morgan, D.; Ceder, G. *Phys. Rev. B* 2001, 63, 224304.

[37] Blaha, P.; Schwarz, K.; Sorantin, P.; Trickey, S. B. *Comput. Phys. Commun.* 1990, 59, 399.

[38] Rossen, E.; Jones, C. D. W.; Dahn, J. R. *Solid State Ionics* 1992, 57, 311.

[39] Kanno, R.; Kubo, H.; Kawamoto, Y.; Kamiyama, T.; Izumi, F.; Takeda, Y.; Takano, M. *J. Solid State Chem.* 1994, 110, 216.

[40] Hirano, A.; Kanno, R.; Kawanoto, Y.; Takeda, Y.; Yamaura, K.;Takano, M.; Ohyama, K.; Ohashi, M.; Yamaguchi, Y. *Solid State Ionics* 1995, 78, 123.

[41] Delmas, C.; Ménétrier, M.; Croguennec, L.; Saadoune, I.; Rougier, A.; Pouillerie, C.; Prado, G.; Grüne, M.; Fournès, L. *Electrochim. Acta* 1999, 45, 243.

[42] Pouillerie, C.; Suard, E.; Delmas, C. *J. Solid State Chem.* 2001, 158, 187.

[43] Van der Ven, A.; Ceder, G. *Electrochem. Commun.* 2004, 6, 1045.

Chapter 4

Local Electronic Structure of the Olivine Phases of Li_xFePO_4

4.1 Introduction

The olivine phase of $LiFePO_4$ is drawing much interest as a promising cathode material for rechargeable lithium ion batteries. It is nontoxic, non-hygroscopic, chemically stable, environmentally friendly and inexpensive [1-3]. It has a discharge voltage of 3.5 V vs. Li/Li^+ and a high theoretical capacity of 170 mAh/g. The small volumetric expansion and structural changes during Li^+ insertion and extraction are believed beneficial to a high cycle life [4]. There are problems with its low electronic conductivity, but there are practical approaches to improving conductivity by doping with supervalent cations [5], carbon coating [6, 7], or by reducing the particle size [8].

$LiFePO_4$ occurs in nature as the mineral triphylite, and its delithiated counterpart, $FePO_4$, is known as heterosite. At room temperature, both phases are olivine-type orthorhombic structures. Lithium atoms are present as chains in the channels along the b-axis in $LiFePO_4$ [1, 2]. For intermediate compositions of lithium in Li_xFePO_4, where $0 < x < 1$, the material is a two-phase system consisting of both heterosite and triphylite in proportions consistent with the overall lithium content [1]. Recently Yamada *et al.*

suggested that Li_xFePO_4 is a mixture of $Li_{0.05}FePO_4$ and $Li_{0.89}FePO_4$ [9]. At temperatures around 350 ˚C, a new disordered phase appears, having the same olivine structure and lattice parameters intermediate between those of heterosite and triphylite [10]. The high temperature phase is not yet well understood, however.

Theoretical and experimental work has been done to understand the electronic structure and phase transitions in $LiFePO_4$ during lithium insertion and extraction. The charge compensation and phase separation in the electrochemical lithiation reaction is generally attributed to the reduction of Fe^{3+} to Fe^{2+} [1, 11, 12]. It has been suggested that the PO_4^{3-} polyanion lowers the Fermi level and hence raises the cell potential, and maintains a stable structural framework through strong P-O covalent bonds [2, 3, 13, 14]. Density functional theory (DFT) calculations show that Fe 3d states dominate the bottom of the conduction bands in both $LiFePO_4$ and $FePO_4$. The unoccupied Fe 3d states may have more mixing with O 2p states in $FePO_4$ than in $LiFePO_4$ [15]. Unfortunately, the two-phase region of the phase diagram is not predicted by standard DFT methods, although DFT+U methods give more accurate predictions of the phase diagram and electrochemical potentials [12, 16].

The shift of the Fe K-edge of up to 4.3 eV during delithiation, observed using in situ X-ray absorption spectroscopy (XAS), has been attributed to oxidation of Fe^{2+} to Fe^{3+} [17]. Mössbauer spectroscopy also provides evidence for transitions between Fe^{2+} and Fe^{3+} during lithiation and delithiation [18]. A study of the valence-related Fe 3d electronic states

was performed with soft X-ray absorption and emission spectroscopies [15]. An upward shift of about 2 eV at the Fe L_3 peak and a stronger bonding character of the Fe 3d and O 2p orbitals were detected after delithiation. These changes were attributed to the Fe^{2+} to Fe^{3+} oxidation and a large charge transfer from ligand O 2p to Fe 3d states. High resolution electron energy loss spectroscopy (EELS) measurements also showed a shift of Fe white lines and the presence of a new peak at the O K-edge after delithiation [19].

In the present work, we quantify the charge compensation during lithium extraction from $LiFePO_4$ by using electron energy loss spectroscopy (EELS) with computational support. A shift of 1.4 eV at Fe L-edges is detected after delithiation. Quantification of the near-edge structure at Fe L-edges and the O K-edge shows that the Fe and O atoms play equal roles in charge compensation upon delithiation. We also report features of the lithium distribution at both room and high temperature showing that the high-temperature disordered phase of $Li_{0.6}FePO_4$ is preserved at low temperature.

4.2 Experimental

Powders of $LiFePO_4$ were prepared by a solid-state reaction. Iron oxalate ($Fe(C_2O_4)\cdot 2H_2O$), ammonium dihydrogen phosphate ($NH_4H_2PO_4$) and lithium carbonate (Li_2CO_3) were mixed in the molar ratio 1:1:0.5, then ball milled in acetone for 12 hours. The paste was dried at 60 ˚C in vacuum. The mixture was then reground and heated in a nitrogen atmosphere at 700 ˚C for 24 hours. Aqueous potassium persulfate ($K_2S_2O_8$) solution was used to chemically delithiate $LiFePO_4$ to achieve $Li_{0.6}FePO_4$ and $FePO_4$. A

portion of the $Li_{0.6}FePO_4$ powder was prepared as a disordered solid solution by heating to 380 ˚C in an evacuated glass ampoule and quenching the sealed ampoule into water, as described elsewhere [20].

X-ray diffraction (XRD) patterns were measured with a Philips PW3040-Pro diffractometer using Cu Kα radiation (λ = 0.15046 nm). Silicon powder was mixed with the samples as a standard to ensure accuracy in peak position determination. Rietveld refinement was then used to determine the compositions and structures.

For transmission electron microscopy (TEM) analysis, the samples were crushed with a mortar and pestle in alcohol and the powder was dispersed on a holey carbon grid. Electron energy loss spectrometry (EELS) data were acquired using a post-column Gatan 666 parallel EELS spectrometer installed on a Philips EM420 electron microscope operating at 100 kV. The energy resolution is about 1.5 eV with an energy dispersion of 0.5 eV per channel. The experimental spectra were deconvoluted using a Fourier-log method to remove plural scattering [21]. A power-law fit was performed to the background just before the onset of each ionization edge, and the estimated background was then subtracted from the data [22].

4.3 Computational

Calculations of the electronic structure were performed for a four-formula unit cell for Li_xFePO_4 (x = 1 and 0). The VASP [23, 24] (Vienna ab-initio simulation program) code was used with projector augmented wave (PAW) potentials in the generalized gradient

approximation (GGA). Calculations were performed for both ferromagnetic and antiferromagnetic configurations of the iron atoms. Following Zhou, *et al.*, [16, 25] we also examined the effect of the self energy U, which was set to 4.3 eV. The initial coordinates were taken from Tang and Holzwarth [26] and a full relaxation of the unit cell and atomic positions was performed. A plane wave energy cutoff of 500 eV was used in conjunction with a $9\times2\times7$ k point grid (corresponding to 20 irreducible k points) to obtain an energy convergence to 0.001 eV/atom. For density of states (DOS) calculations, the atom positions were taken from a converged calculation and the number of bands calculated was increased to 130. The density of states was evaluated by convoluting appropriately weighted individual band energies at each k point with a Gaussian of width 1.5 eV, giving a resolution that matched the experimental data

To understand possible charge transfers it is useful to apportion the total charge among the different atoms in the unit cell. This can be done in various ways. One accepted technique is to calculate the charge in spheres centered at the atom positions. Since there is no rigorous procedure for selecting sphere size, the relative charge associated with each atom — or for that matter the division of charge between atoms and an interstitial region — can be arbitrary. Instead we have chosen to follow the procedure of Bader [27], where the division is made along contour lines following the interatomic peaks in the charge density. This gives an unambiguous division of charge among the unit cell constituent atoms.

Features in the EELS fine structures of transition metal compounds can be influenced by both atomic and solid-state electronic effects. The shapes of transition metal $L_{2,3}$-edges can be altered significantly by atomic multiplets arising from the overlap of the radial wave functions for the 2p hole, and holes in the partially-filled 3d band. Final states must be calculated by vector coupling of the 2p and 3d wave functions. This strong, purely atomic, effect is only partly screened in the solid state, meaning that features in spectra are comparable for solids and isolated atoms. The initial and final states are specified as a sum of terms in the LS coupling scheme. For example for Fe^{2+}, the initial state configuration would be $2p^6 3d^6$ and the final state $2p^5 3d^7$. The initial ground state $^5D_2$ is given by Hund's rule. Transitions calculated with a dipole selection rule give ΔJ as -1, 0, 1. In this case there are 110 terms allowed for the final state, giving 68 distinct transitions. The strengths of the various transitions are calculated from the appropriate matrix elements from the Hamiltonian

$$H = \sum_N \frac{p_i^2}{2m} + \sum_N \frac{-Ze^2}{r_i} + \sum_{pairs} \frac{e^2}{r_{ij}} + \sum_N \zeta(r_i) l_i s_i \ . \qquad (4.1)$$

The first two terms of this Hamiltonian, the kinetic energy and the electron-nuclear Coulombic interaction, are the same for all electrons in a configuration. Only the last two terms, the electron-electron interaction and the spin-orbit coupling need to be considered. In practice, for transition element ions, it has been found necessary to reduce the pd exchange integrals by 20% from the values calculated using the Hartree-Fock wave functions.

The oxygen atoms neighboring the Fe ion add a crystal field that is represented as a sum of spherical harmonics and can be treated as a perturbation to the atomic multiplet calculation. The main effect is to change the local symmetry from spherical to octahedral. The strength of this crystal field is specified by 10 Dq, the separation between the t_{2g} and e_g molecular orbitals. Since contributions from these orbitals could not be directly identified from the densities of states, we varied 10 Dq between 1eV and 3.5 eV to best match the experimental Fe $L_{2,3}$ spectrum. Calculations of some transition metal white line intensities in octahedral and tetrahedral symmetry are given by Van der Laan and Kirkman [28]. A detailed description of multiplet theory applied to inner shell spectroscopy can be found in the review by de Groot [29], whose codes were used in the present work.

4.4 Results

At room temperature, XRD patterns (Fig. 4.1) of $LiFePO_4$ and $FePO_4$ are readily indexed as single-phase triphylite and heterosite, while $Li_{0.6}FePO_4$ is a simple mixture of the two. At 380 ˚C, the two phases in $Li_{0.6}FePO_4$ merge to form a new single phase as expected from the phase diagram [20]. Fig. 4.1 also shows that the quenched material preserves its disordered structure well at room temperature, owing to the sluggish kinetics of the unmixing process at temperatures below 200 ˚C.

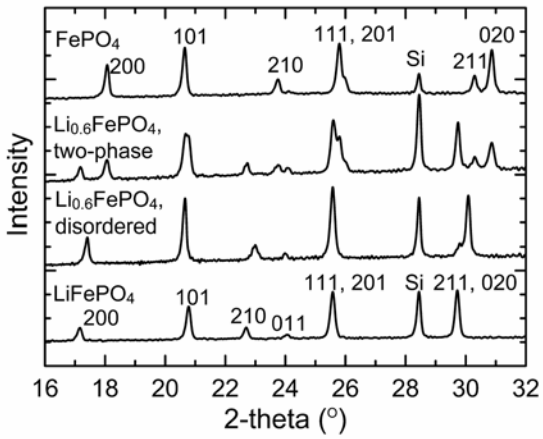

Fig. 4.1 Indexed X-ray powder diffraction patterns from samples of Li_xFePO_4 with different states of lithiation, with Si as an internal standard.

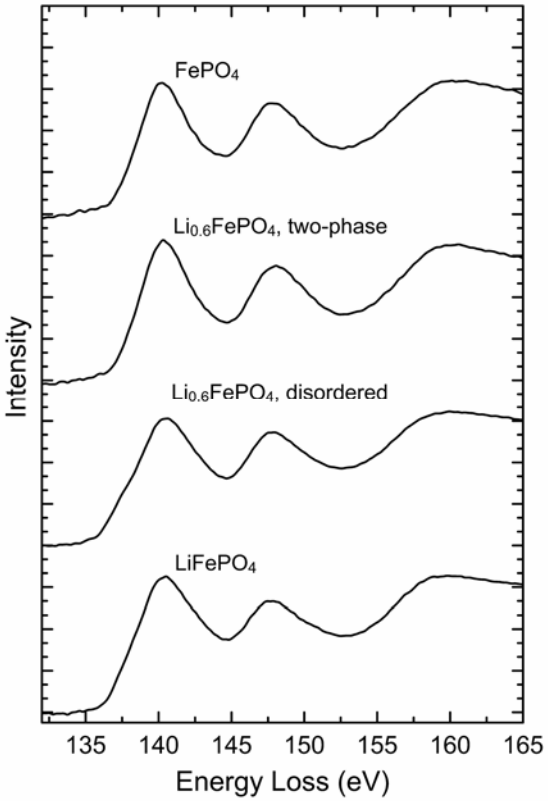

Fig. 4.2 P $L_{2,3}$-edge from Li_xFePO_4. The spectra were normalized with a 50 eV window after the L_2 peak.

Fig. 4.2 shows EELS measurements of P $L_{2,3}$-edges of the samples. The peak positions and fine structures are similar for all samples. No changes in these P spectra were observed during delithiation or thermal treatment. The low-loss EELS spectra in Fig. 4.3 are complicated by the overlap of the Li K-edge and Fe $M_{2,3}$-edge. Quantification is not possible, but qualitative features are visible. The peaks in this area (indicated as A, B and C) vary in their intensities and shapes. The peak A at 55 eV and peak C at 65 eV in the triphylite phase belong to the Li K-edge, so the intensities of these features give semiquantitative information about the Li content in the material. These features are less evident in the disordered sample, and vanish in the two-phase sample and heterosite sample. The peak B around 58 eV contains significant contributions from both the Li K-edge and the Fe $M_{2,3}$-edge. It is broad in the fully-lithiated $LiFePO_4$, and becomes sharper in samples containing less lithium. This peak actually grows during delithiation, indicating Fe $M_{2,3}$-edge may gain intensity when lithium is extracted from the materials.

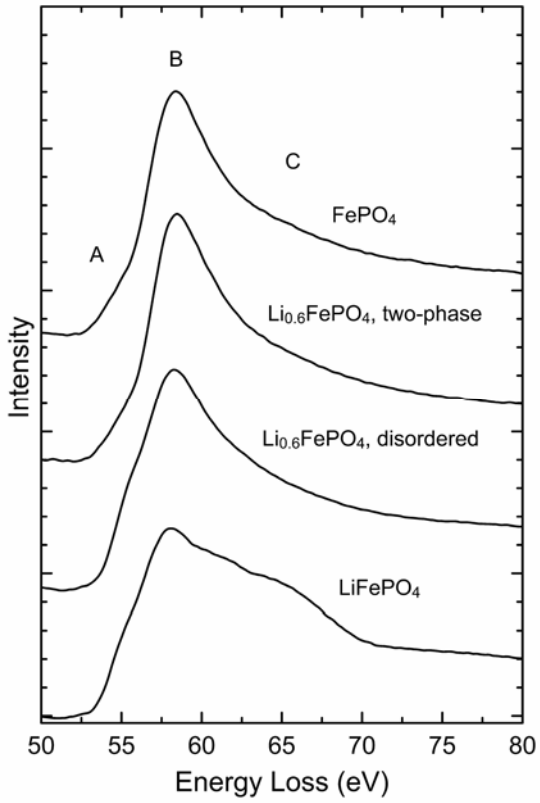

Fig. 4.3 Li K-edge and Fe $M_{2,3}$-edge from Li_xFePO_4. The spectra were normalized with a 50 eV window after the peak.

Fig. 4.4 shows a change in the O K-edge with delithiation. A pre-peak (labeled "A") at 528 eV is found in the delithiated material. It is nearly negligible in the triphylite ($LiFePO_4$) and the disordered sample, but is distinct in the two-phase and fully-delithiated samples. In the disordered sample with composition $Li_{0.6}FePO_4$, this pre-peak is also present but its intensity is only 27% of that in the heterosite phase. The main peak of the O K-edge (531-547 eV with a maximum at 535.6 eV) is similar for all samples.

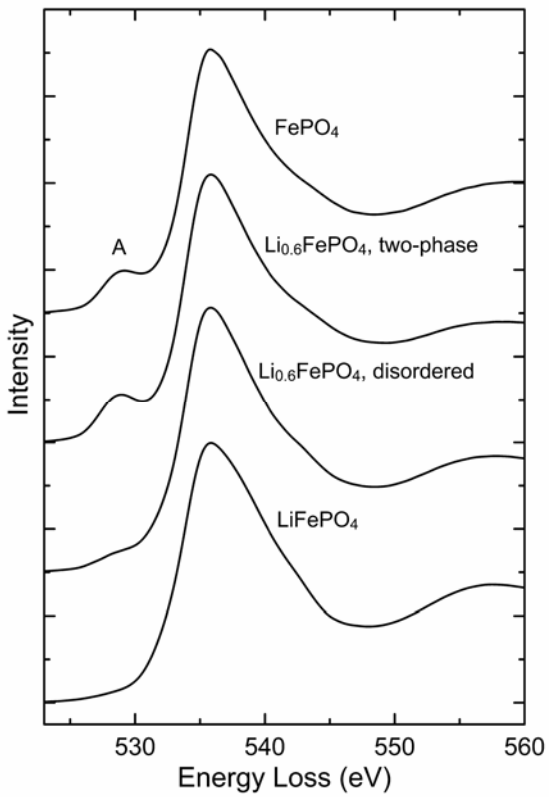

Fig. 4.4 O K-edge from Li_xFePO_4. The spectra were normalized with a 40 eV window after the main peak.

Fig. 4.5a shows changes in the Fe L-edges with delithiation. These intense sharp peaks from transition metals are called white lines, and originate from electronic transitions from occupied 2p core states to empty 3d states. The intensity under the white lines contains contributions from excitations to both bound and continuum states. The continuum contribution was determined by using a two-segment line model to extract the bound state contribution accurately [30]. With delithiation, the Fe white lines also undergo an upward shift in energy. The centroid of the L_3 peak is plotted in Fig. 4.5b. In the fully delithiated heterosite phase, the shift is 1.4 eV. A variation of Fe white line intensity is also observed (Fig. 4.5c). From x = 1 to x = 0, the total intensity of the L_2 and L_3 white lines

increases by 15%, indicating a depletion of Fe 3d electrons, while the increase is about 7% in the disordered sample of $Li_{0.6}FePO_4$.

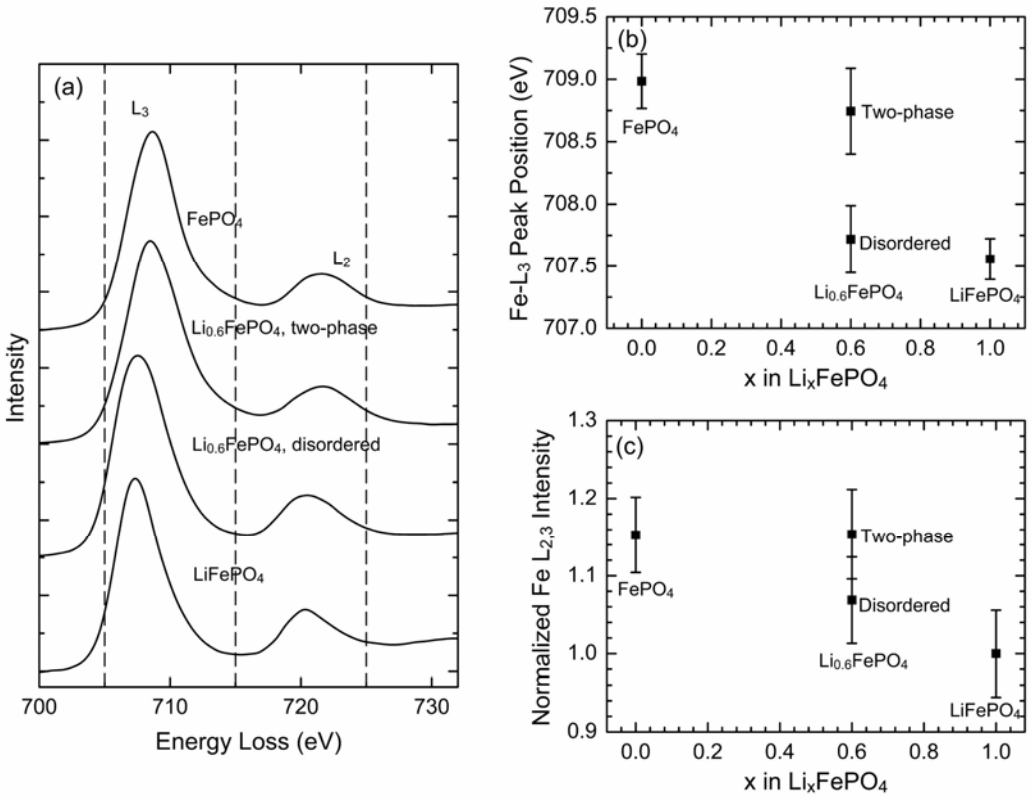

Fig. 4.5 (a) Fe $L_{2,3}$-edges from Li_xFePO_4. The spectra were normalized with a 40 eV window after the L_2 peak. The measured shift of the L_3 centroid and the normalized white line intensities are plotted in (b) and (c), respectively.

The calculated densities of Fe d-states and O p-states for $LiFePO_4$ and $FePO_4$ in antiferromagnetic configuration for U = 4.3 eV are shown in Fig. 4.6 and Fig. 4.7, respectively. At the resolution of the experimental data, which was matched in the calculations, no differences could be seen between densities of states for ferromagnetic and antiferromagnetic configurations, or for different values of U. Charges associated with the oxygen and iron atoms as given by the Bader analysis are presented in Table 1. There is a

loss of one electron from $LiFePO_4$ to $FePO_4$ per chemical formula, indicating that only Fe and O contribute to the charge compensation. Multiplet calculations for Fe^{2+} and Fe^{3+} are shown in Fig. 4.8. Setting 10 Dq to 3 eV gives the best fit to the experimental peak shape. The shift between the centroids of Fe^{2+} and Fe^{3+} L_3 peaks is then 1.87 eV.

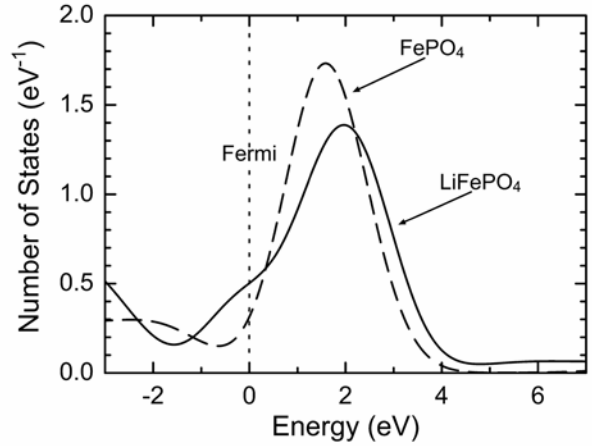

Fig. 4.6 The VASP calculation of Fe 3d partial density of states per formula unit. The intensity above the Fermi level corresponds to the intensity of white lines in EELS spectra. A 14% increase of the unoccupied states from $LiFePO_4$ to $FePO_4$ is predicted.

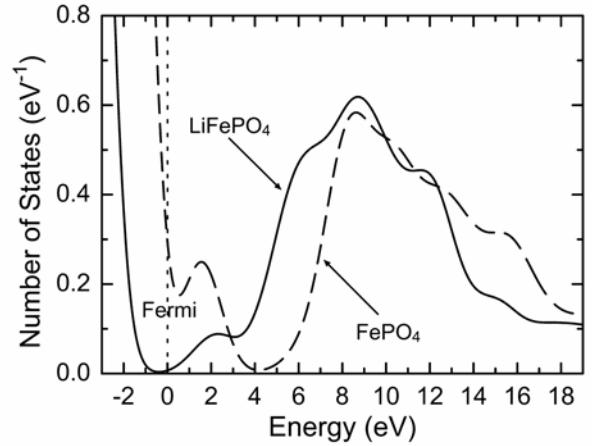

Fig. 4.7 The VASP calculation of the O 2p partial density of states per formula unit. The intensity from 0 to 3 eV above the Fermi level corresponds to the intensity of the experimental pre-peak.

Table 4.1 Bader analysis of the number of electrons surrounding O and Fe atoms per Li_xFePO_4 (x = 0, 1)

	O	Fe
LiFePO4	31.55	6.46
FePO4	31	6.01
Difference	0.55	0.45

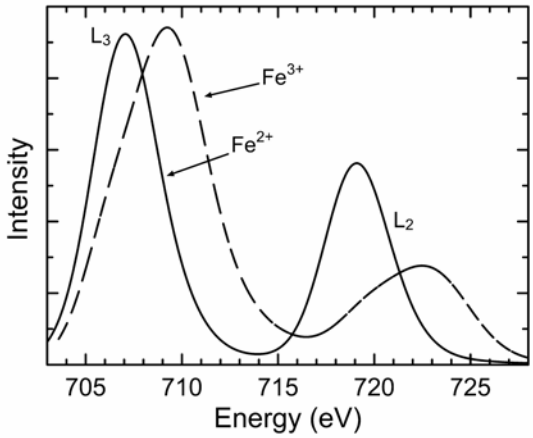

Fig. 4.8 Atomic multiplet calculation of Fe $L_{2,3}$ white lines.

4.5 Discussion

Significant changes were observed at the Fe L-edges after delithiation. The upward shift of about 1.4 eV after delithiation indicates an increase in the difference between the bonding energy of the localized Fe 2p levels and the outer delocalized Fe 3d levels in the solids. Such a shift can be caused by a valence change of the atom, although changes in the structural and chemical environment surrounding the atom can cause small shifts in white lines. The shift between the L_3 peaks for Fe^{2+} and Fe^{3+} is 1.87 eV when calculated using the

atomic multiplets codes with 10 Dq set at 3eV. This is in reasonable agreement with the experimental value of 1.4 eV (Fig. 4.8). The atomic multiplet approach is best suited to describing systems that are mainly ionic in character, with limited covalent bonding to nearest neighbors described by the crystal field. This might not apply to the $LiFePO_4$, $FePO_4$ system, as partly evidenced by the large value of 10 Dq needed to bring about some measure of agreement with experiment. We therefore expect less than a full electron transfer to Fe atom with lithiation. This may also be the cause of the discrepancy between the intensity of the L_2 peak of the experimental and calculated spectra.

More information about the electronic states of Fe atoms is available from the intensities of the normalized Fe white lines. The total white line intensity of the $FePO_4$ phase is 15% larger than that of the $LiFePO_4$ phase. This indicates that with delithiation, more electrons are removed from the Fe 3d levels, and Fe^{2+} is oxidized to a higher valence. This is in agreement with the VASP electronic structure calculations (Fig. 4.6) that show a 14% increase in the proportion of unoccupied d states when going from $LiFePO_4$ to $FePO_4$. There are 3.2 holes in the Fe 3d-states per formula unit in $LiFePO_4$ as indicated by the VASP calculations. A 15% increase of white line intensity corresponds to a depletion of 0.48 electrons per Li atom. From the pseudopotential computational work, the Bader analysis of the charge density from the VASP calculations shows that the iron is responsible for 45% of the charge compensation. Evidently, Fe atoms are not responsible for all of the charge compensation in $LiFePO_4$ during delithiation and lithiation.

In the disordered sample of $Li_{0.6}FePO_4$, the increase of the white line intensity is about 7%, corresponding to a removal of 0.22 electrons. Considering that 0.48 electrons are removed in fully-delithiated $FePO_4$, this value is consistent with the overall composition. In all the experimental results, the spectra from the delithiated (x = 0) sample and the two-phase (x = 0.6) sample were almost identical. This is an artifact of sample preparation. The electron-transparent parts of the two-phase sample tended to be the delithiated materials. Perhaps this is caused by the delithiation process, where delithiated thin layers are more likely to chip off the sample when it is crushed and ground with the mortar and pestle.

At the O K-edge, the most visible change with delithiation is the increase in the pre-peak intensity at 528 eV. This pre-peak originates from electron transitions from a 1s core state to states with 2p character at oxygen atoms. Since the number of available holes in these 2p states is determined by the extent of the orbital hybridization with adjacent atoms, this pre-peak provides information on the bonding of the oxygen atoms [31]. In $LiFePO_4$, the pre-peak is not present, indicating that all six 2p states of oxygen atoms are fully occupied. No 1s to 2p transition can occur. In the fully delithiated $FePO_4$ phase, the pre-peak intensity increases significantly, indicating more hybridization between oxygen and surrounding atoms, and more covalent bonding. The pre-peak is also visible in the VASP calculations of the oxygen p density of states (Fig. 4.7). The calculated ratio of pre-peak to integrated p DOS, from 3 eV to 14 eV above the Fermi level is 14%, which can

be compared directly to the experimental measurement of 8% in the same energy range, since the matrix element for the inelastic scattering is slowly varying over this small range of energy. These results also agree with results from soft XAS measurements [15]. The pre-peak in the disordered sample of $Li_{0.6}FePO_4$ is about 27% of that in the $FePO_4$ phase, showing a reasonable trend with lithiation as the extra electrons associated with the Li^+ are accommodated in part by O 2p states that are more covalently bonded to Fe. The oxygen atoms in $LiFePO_4$ and $FePO_4$ have three inequivalent sites [18]. EELS measurements cannot separate these three contributions. Nevertheless, since no changes are observed at the P K-edge and the P-O bonds have been shown to undergo minimal shrinking during lithium removal [18], we expect that the increase of the pre-peak intensity is contributed mainly by the oxygen atoms bonded to Fe. We hereby suggest that the electron removed with Li^+ during delithiation is donated by electronic states that are hybrids of the O 2p and Fe 3d states.

4.6 Conclusion

The olivine phases of triphylite $LiFePO_4$, heterosite $FePO_4$, two-phase $Li_{0.6}FePO_4$ and a disordered solid solution of $Li_{0.6}FePO_4$ were studied by electron energy loss spectroscopy (EELS) and electronic structure calculations. A shift of about 1.4 eV at Fe L-edges was detected after delithiation. A charge transfer up to 0.48 electrons from iron is observed from the variation in the experimental Fe white line intensity. Both experimental and theoretical data show oxidation of Fe after delithiation. Electronic structure

calculations and the presence of a pre-peak on the oxygen K-edge of $FePO_4$ indicate that only ~half of the charge compensation is taking place on the iron atoms while the remainder takes place on oxygen atoms. The 2p states at oxygen atoms are fully occupied in $LiFePO_4$, but there is some emptying of these states in the delithiated material. The oxygen atoms are more covalently bonded in $FePO_4$ than in $LiFePO_4$. Finally, we observed that the high temperature disordered phase of $Li_{0.6}FePO_4$ was kinetically stable at room temperature.

References

[1] Padhi, A. K.; Nanjundaswamy, K. S.; Goodenough, J. B. *J. Electrochem. Soc.* 1997, 144, 1188.

[2] Padhi, A. K.; Nanjundaswamy, K. S.; Masquelier, C.; Okada, S.; Goodenough, J. B. *J. Electrochem. Soc.* 1997, 144, 1609.

[3] Yamada, A.; Chung, S. C.; Hinokuma, K. *J. Electrochem. Soc.* 2001, 148, A224.

[4] Deb, A.; Bergmann, U.; Cramer, S. P.; Cairns, E. J. *Electrochimica Acta* 2005, 50, 5200.

[5] Chung, S. Y.; Bloking, J. T.; Chiang, Y. M. *Nat. Mater.* 2002, 1, 123.

[6] Huang, H.; Yin, S. C.; Nazar, L. F. *Electrochem. Solid-State Lett*. 2001, 4, A170.

[7] Chen, Z; Dahn, J. R. *J. Electrochem. Soc.* 2002, 149, A1184.

[8] Yamada, A; Chung, S. C.; Hinokuma, K. *J. Electrochem. Soc*. 2001, 148, A224.

[9] Yamada, A.; Koizumi, H.; Nishimura, S. I.; Sonoyama, N.; Kanno, R.; Yonemura, M.; Nakamura, T.; Kobayashi, Y. *Nat. Mater.* 2006, 5, 357.

[10] Delacourt, C.; Poizot, P.; Tarascon, J. M.; Masquelier, C.; *Nat. Mater.* 2005, 4, 254.

[11] Burba, C. M.; Frech, R. *J. Electrochem. Soc.* 2004, 151, A1032.

[12] Zhou, F.; Marianetti, C. A.; Cococcioni, M.; Morgan, D.; Ceder, G. *Phys. Rev. B* 2004, 69, 201101.

[13] Padhi, A. K.; Nanjundaswamy, K. S.; Masquelier, C.; Goodenough, J. B. *J. Electrochem. Soc.* 1997, 144, 2581.

[14] Masquelier, C.; Padhi, A. K.; Nanjundaswamy, K. S.; Goodenough, J. B. *J. Solid State Chem.* 1998, 135, 228.

[15] Augustsson, A.; Zhuang, G. V.; Butorin, S. M.; Osorio-Guillén, J. M.; Dong, C. L.; Ahuja, R.; Chang, C. L.; Ross, P. N.; Nordgren, J.; Guo, J. H. *J. Chem. Phys.* 2005, 123, 184717.

[16] Zhou, F.; Kang, K.; Maxisch, T.; Ceder, G.; Morgan, D. *Solid State Commun.* 2004, 132, 181.

[17] Haas, O.; Deb, A.; Cairns, E. J.; Wokaun, A. *J. Electrochem. Soc.* 2005, 152, A191.

[18] Andersson, A. S.; Kalska, B.; Häggström, L.; Thomas, J. O. *Solid State Ionics* 2000, 130, 41.

[19] Laffont, L.; Delacourt, C.; Gibot, P.; Wu, M. Yue; Kooyman, P.; Masquelier, C.; Tarascon, J. Marie *Chem. Mater.* 2006, 18, 5520.

[20] Dodd, J. L.; Yazami, R.; Fultz, B. *Electrochem. Solid-State Lett.* 2006, 9, A151.

[21] Johnson, D. W.; Spence, J. C. H. *J. Phys. D* 1974, 7, 771.

[22] Egerton, R. F. *Electron Energy-Loss Spectroscopy in the Electron Microscope*; Plenum: New York, 1996.

[23] Kresse, G.; Furthmuller, J. *Phys. Rev. B* 1996, 54, 11169.

[24] Kresse, G.; Joubert, D. *Phys. Rev. B* 1999, 59, 1758.

[25] Zhou, F.; Cococcioni, M.; Marianetti, C. A.; Morgan, D.; Ceder, G. *Phys. Rev. B* 2004, 70, 235121.

[26] Tang, P.; Holzwarth, N. A. W. *Phys. Rev. B* 2003, 68, 165107.

[27] Bader, R. F. W. *Atoms in Molecules: A Quantum Theory*; Oxford University Press: New York, 1994.

[28] Van der Laan, G.; Kirkman, I. W. *J. Phys.: Condens. Matter* 1992, 4, 4189.

[29] de Groot, F. *Coord. Chem. Rev.* 2005, 249, 31.

[30] Pearson, D. H.; Fultz, B.; Ahn, C. C. *Appl. Phys. Lett.* 1988, 53, 1405.

[31] de Groot, F.; Grioni, M.; Fuggle, J. C.; Ghijsen, J.; Sawatzky, G. A.; Petersen, H. *Phys. Rev. B* 1989, 40, 5715.

Chapter 5

Bonding in Mg_2Si

5.1 Introduction

As the most widely used anode material in Li-ion batteries, graphite only has a limited capacity of 372 mAh/g [1]. Intensive researches have been conduced to find the new generation anode to replace graphite [2-5]. Mg_2Si gained attention because it has several advantages. Both Mg and Si are inexpensive, lightweight and naturally abundant. This material has a voltage plateau of 0.26 V vs. Li/Li^+ [6], which is comparable to graphite. A capacity of 830 mAh/g was obtained for bulk material, and Mg_2Si thin film even showed a capacity more than 2000 mAh/g [7, 8].

Mg_2Si is also drawing attentions as a hydrogen storage material [9]. Storing hydrogen as a liquid or compressed gas consumes considerable energy and it is difficult to maintain hydrogen in these states for extended times without significant losses. An alternative approach is to store hydrogen chemically in the form of hydrides which are stable at room temperature. In the presence of a catalyst or at elevated temperature, the hydrides decompose and release hydrogen. The dehydrogenation process can be understood through thermodynamics [9]. Mg_2Si can react with H_2 and form MgH_2/Si

mixture. The enthalpy is -75.3 kJ/mol for (MgH_2 + 0.5 Si), and is -38.9 kJ/mol for (0.5 Mg_2Si + H_2). The state (MgH_2 + 0.5 Si) is stable at room temperature [9]. When the temperature is increased, an endothermic reaction occurs. Some MgH_2 in the MgH_2/Si mixture decomposes and forms Mg_2Si to reach new equilibrium. This system has a theoretical hydrogen storage capacity of 5 wt %, which is acceptable for practical applications. Observable dehydrogenation starts below 300 ˚C, which is relatively low compared to other systems [9]. Hence, Mg_2Si is considered to be practical material for hydrogen storage at reduced temperature.

Despite this recent progress in applications, fundamental studies on Mg_2Si can be traced back to more than half century ago. Mg_2Si has an antifluorite structure [10] with space group $Fm\bar{3}m$ (#225) as shown in Fig. 5.1. Si atoms form an FCC frame and Mg atoms occupy the eight tetrahedral interstitial sites. Extensive studies, both experimental and theoretical, have been conducted on the electronic structure of Mg_2Si. However, controversy exists on the degree of the ionicity and the associated charge transfer in the Mg-Si bond. The strong reststrahl peak in infrared reflectivity measurement was though to indicate an ionic bonding in Mg_2Si [11]. Eldridge *et al.* concluded the Mg-Si bond was strongly covalent with only 10% ionic character based on their study on the atomic radii [12]. From the Mg binding energy, Whitten estimated that the ionicity in Mg_2Si was less than 33% [13]. Meloni *et al.* performed hard-core pseudopotential calculations which

showed the upper three valence bands were dominated by Si 3p states with only a little Mg participation, and they concluded the Mg-Si bond was quite ionic with a small covalent component [14]. The presence of some covalent character in the Mg-Si bond was also supported by Auger spectrometry measurement where occupancies in Mg 3s and 3p states were detected [15]. All-electron calculations by Baranek *et al.* showed a mixed covalent-ionic nature in the Mg-Si bond [10]. From their Mulliken-population analysis, they estimated 0.9 electron per Mg were transferred to Si. However, an in-situ XPS study by van Buuren *et al.* concluded the Mg-Si bond was strongly covalent [16]. From the chemical shifts, they derived an ionicity of 8%.

In the present work, we investigate the ionicity of the Mg-Si bond in Mg_2Si by electron energy loss spectrometry (EELS) and first-principles calculations. The results are compared with those of MgO and Si which are used as references for typical ionic and covalent bonding compounds, respectively. Our results indicate that the Mg-Si bond is strongly ionic, although the charge transfer is not complete.

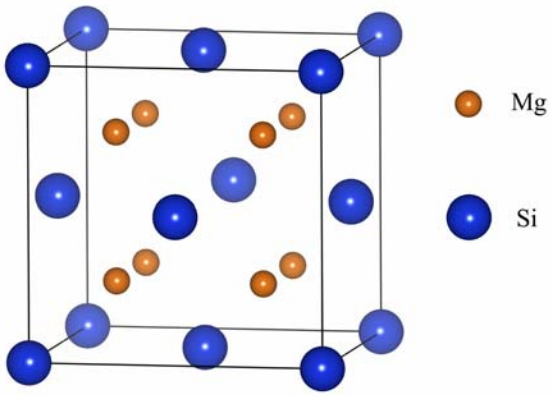

Fig. 5.1 The antifluorite structure of Mg_2Si unit cell.

5.2 Experimental

In this study, commercial powders Mg_2Si (99.5%, Alfa) and MgO (99.95%, Alfa) were used. Crystalline Si, denoted as c-Si to distinguish from the Si atoms, was cut from a silicon wafer. To prepare the samples for EELS measurements, these materials were crushed with a mortar and pestle in alcohol and fine particles were dispersed on holey carbon grids. All operations were done in a glove-box filled with Ar to eliminate contact with water or oxygen. The EELS spectra were acquired with a Gatan 666 parallel EELS spectrometer installed on a Philips EM420 transmission electron microscope (TEM) operating at 100 kV. An energy dispersion of 0.2 eV/channel was used and the energy resolution was about 1.5 eV. Plural scatterings were removed from the experimental spectra by the Fourier-log method [17]. The background under each ionization edge was fitted to a power-law model, and then was removed from the experimental data [18].

5.3 Computational

The calculations of electronic structure were performed by using the full potential linearized augmented plane wave method within the local density functional approximation, as implemented in the WIEN2K code [19]. In this method, the unit cell is divided into non-overlapping muffin-tin (MT) spheres centered at the atomic sites, which separate the interstitial region. The wavefunctions are expanded in spherical harmonics inside the MT spheres, and in plane waves in the interstitial region. Relaxation of the unit

cells was performed and the equilibrium structures are listed in Table 5.1. A $9\times9\times9$ k-points mesh in the irreducible wedge of the Brillouin zone was used for k sampling. In these calculations, Rk_{max}=7.0 (the product of the smallest MT radius by the largest wave vector used in the plane wave expansion) and l_{max}=10 (maximum l for partial waves used inside MT spheres) were used to control the size of the basis set for the wavefunctions. For the exchange-correlation functional, the Perdew-Burke-Ernzerhof generalized gradient approximation [20] was used. The self-consistent calculations were considered to be converged only when the integrated charge difference between last the 2 iterations, $\int|\rho_n-\rho_{n-1}|d\boldsymbol{r}$, was less than 0.00002. To evaluate possible charge transfer involved in bonding, the total charge associated with each atom was determined by integrating the charge density surrounding the atom. The integration volume was defined by the procedure of Bader [21], where the boundaries of the volume are along contour lines following the interatomic peaks of the charge density.

Table 5.1 The equilibrium structures for c-Si, MgO and Mg_2Si

	c-Si	MgO	Mg_2Si
Space group	$Fd\bar{3}m$	$Fm\bar{3}m$	$Fm\bar{3}m$
a (nm)	0.548198	0.425730	0.637036

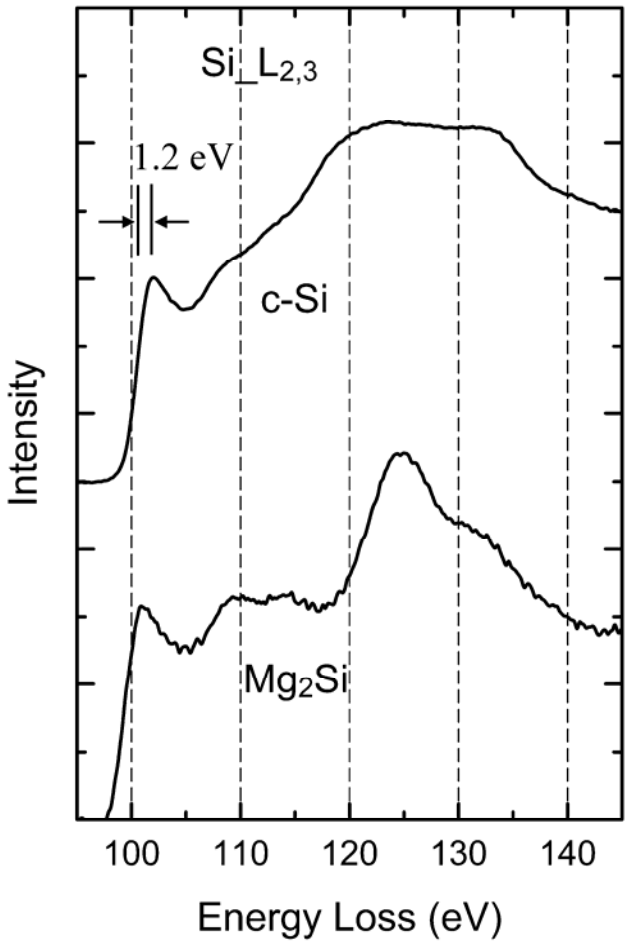

Fig. 5.2 The Si $L_{2,3}$-edge of c-Si and Mg_2Si, respectively. The spectra were normalized with a 30 eV window 50 eV after the edge threshold.

5.4 Results and discussion

The $L_{2,3}$-edge of Si is shown in Fig. 5.2. An upward shift of 1.2 eV is observed in c-Si. The direction of this shift agrees with the result of XPS measurement [16], where an upward shift of 0.95 eV was observed at the 2p level for pure Si. For the size of the shift, results from EELS and XPS are not directly comparable. XPS directly probes the energy of the core level, and the shift of peak position reflects the change in the energy of

corresponding core states. In an EELS spectrum, however, the shift of an ionization edge can be a combination of changes in energies of both the initial core state and the unoccupied final state. The $L_{2,3}$-edge in EELS originates from the 2p→3d-like transitions at Si atoms. The initial 2p level is 0.95 eV deeper in c-Si than in Mg_2Si as already detected by XPS. However, the difference between the EELS and XPS data, 0.25 eV, is approaching the energy dispersion which sets the energy sensitivity of the spectrometer in this study. We cannot assert that the extra shift observed in EELS reveals the difference between the energies of Si 3d-like empty states in c-Si and in Mg_2Si.

The Mg $L_{2,3}$-edges for Mg_2Si and MgO are shown in Fig. 5.3. The intensity under the edge originates form transitions from Mg 2p states. The final states of the transitions are determined by the dipole selection rule $\Delta l = \pm 1$, where Δl is the difference between the angular momentum of the original and final states. In a free Mg atom, the 3s states are fully occupied, hence the $L_{2,3}$-edge only represents the 2p→3d transitions. In solids, however, holes may appear in Mg 3s states because Mg may donate part of its 3s valence electrons to neighboring atoms to form bonds. These 3s holes can accommodate the excited 2p electrons, and the $L_{2,3}$-edge will represent both 2p→3s-like and 2p→3d-like transitions. Variations in the intensities of Mg $L_{2,3}$-edges can therefore provide information on the Mg 3s occupancy.

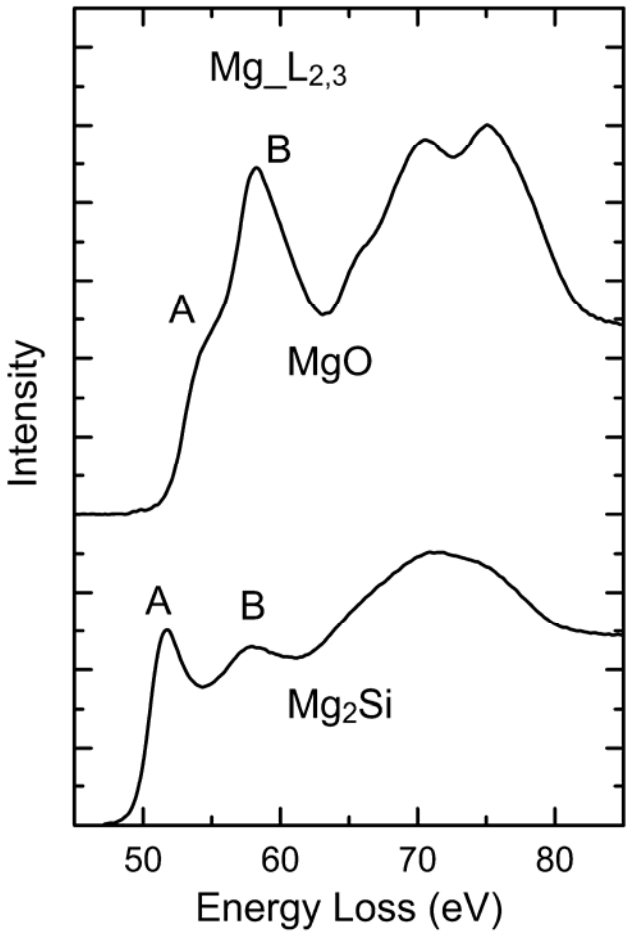

Fig. 5.3 The Mg $L_{2,3}$-edge of MgO and Mg_2Si, respectively. The spectra were normalized with a window from 80 - 100eV.

The multiple peaks of Mg $L_{2,3}$-edge are due to the hybridization of Mg 3s, 3p and 3d states [22]. The origin of each peak is documented by Mizoguchi *et al* [22]. Peak A corresponds to the transitions to Mg 3s-like bonding orbitals. Peak B actually contains twin peaks which correspond to transitions to Mg 3s-like antibonding orbitals and to Mg 3d-like bonding orbitals, respectively. With our experimental energy resolution, these twin peaks merge as peak B. The intensity including all 2p→3s-like contributions is obtained by integrating the spectrum from the onset of peak A to the first minimum after peak B. The

ratio of this integrated intensity for Mg_2Si and MgO is $I_{Mg2Si}/I_{MgO} = 0.73$. The lower integrated intensity of Mg $L_{2,3}$-edge for Mg_2Si is a signal that the charge transferred from Mg during bonding may be less in Mg_2Si than in MgO. However, quantification of the transferred charge and explicit conclusions are hindered by the presence of the 2p→3d-like component in peak B, because the fraction of this component is unknown.

To find out the valence charge associated to each atom, electronic structure calculations were performed. The valence electron distributions in c-Si, MgO and Mg_2Si are shown in Fig. 5.4 - 5.6, respectively. In c-Si, the Si-Si bond is 100% covalent. The sharing of a pair of electrons among Si atoms produces a high electron density in the outer-shell area where the bonding orbitals are formed. In Fig. 5.4, these bonds appear as protruding ridges at the midway between the two adjacent Si atoms. Because of the tetrahedral coordinating environment, sp^3 hybridization occurs among Si 3s and 3p atomic states and produces four identical bonding orbitals extending along <111> directions.

In the typical ionic compound MgO (Fig. 5.5), there is a valley of electron density between Mg and O, in contrast to the ridge-like feature in c-Si. The minima of electron density in the intermediate area indicate that no obvious electron-sharing happens. Furthermore, both Mg and O have a nearly spherical electron cloud which is a representative feature of atoms in ionic compounds. The small nonspherical distortion of the outer contours around O is caused by weak O-O covalent bonds. The presence of local

minima of charge in between atoms and isotropic distribution of electron density are good evidence for a strong ionic character in bonding.

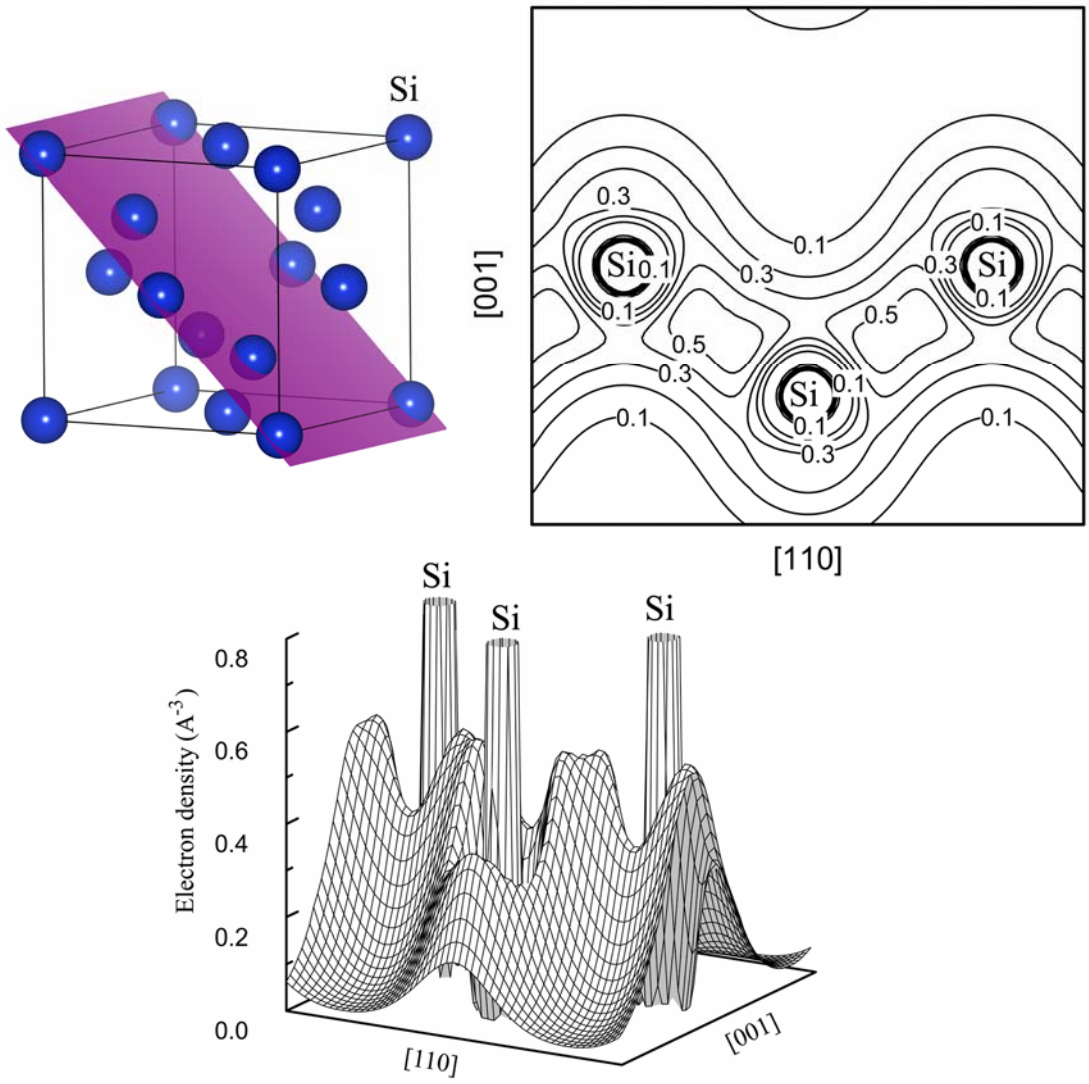

Fig. 5.4 The calculated 2-D and 3-D valence electron density of c-Si on {110} type plane. The corresponding lattice plane is shown.

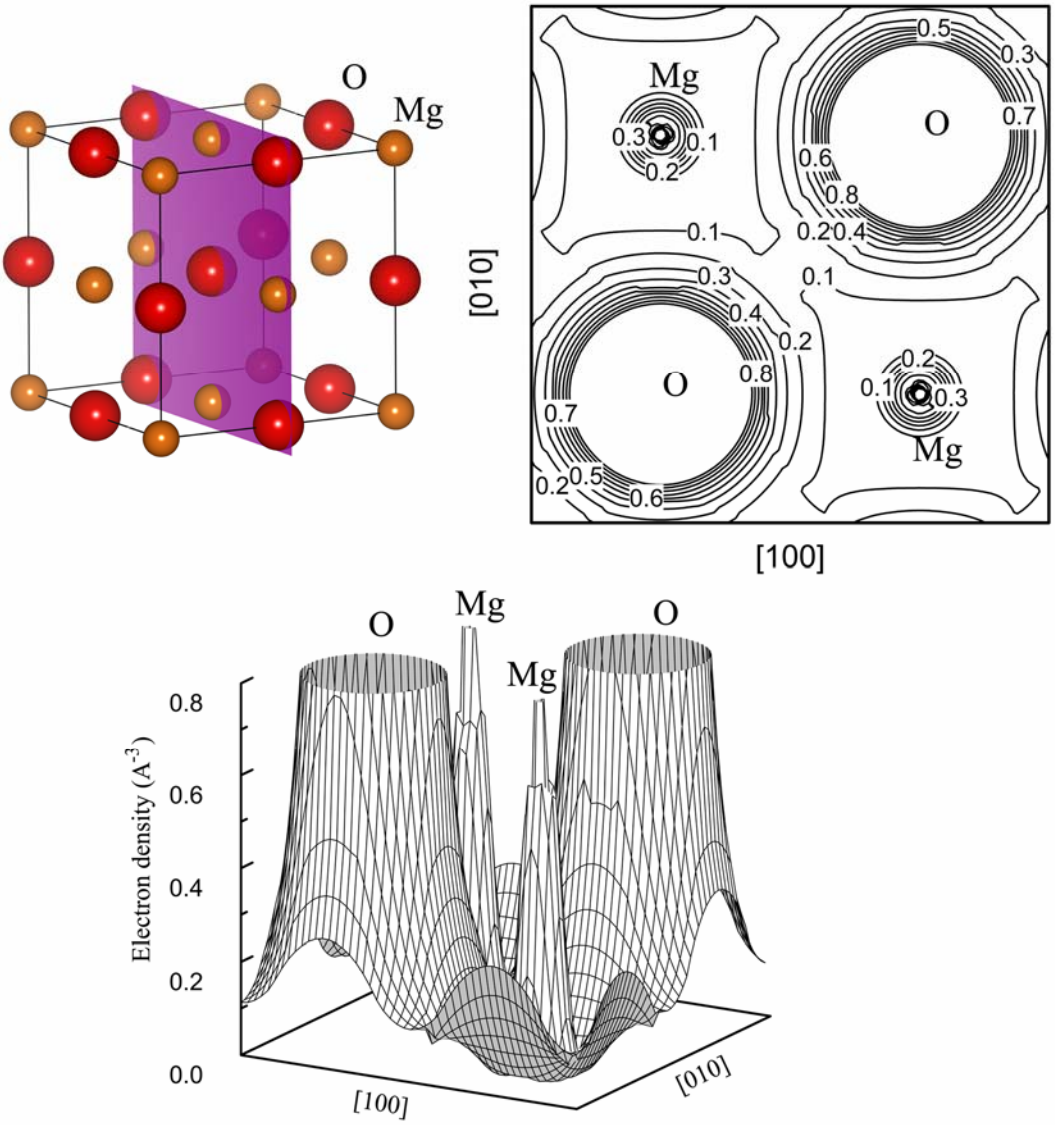

Fig. 5.5 The calculated 2-D and 3-D valence electron density of MgO on {100} type plane. The corresponding lattice plane is shown.

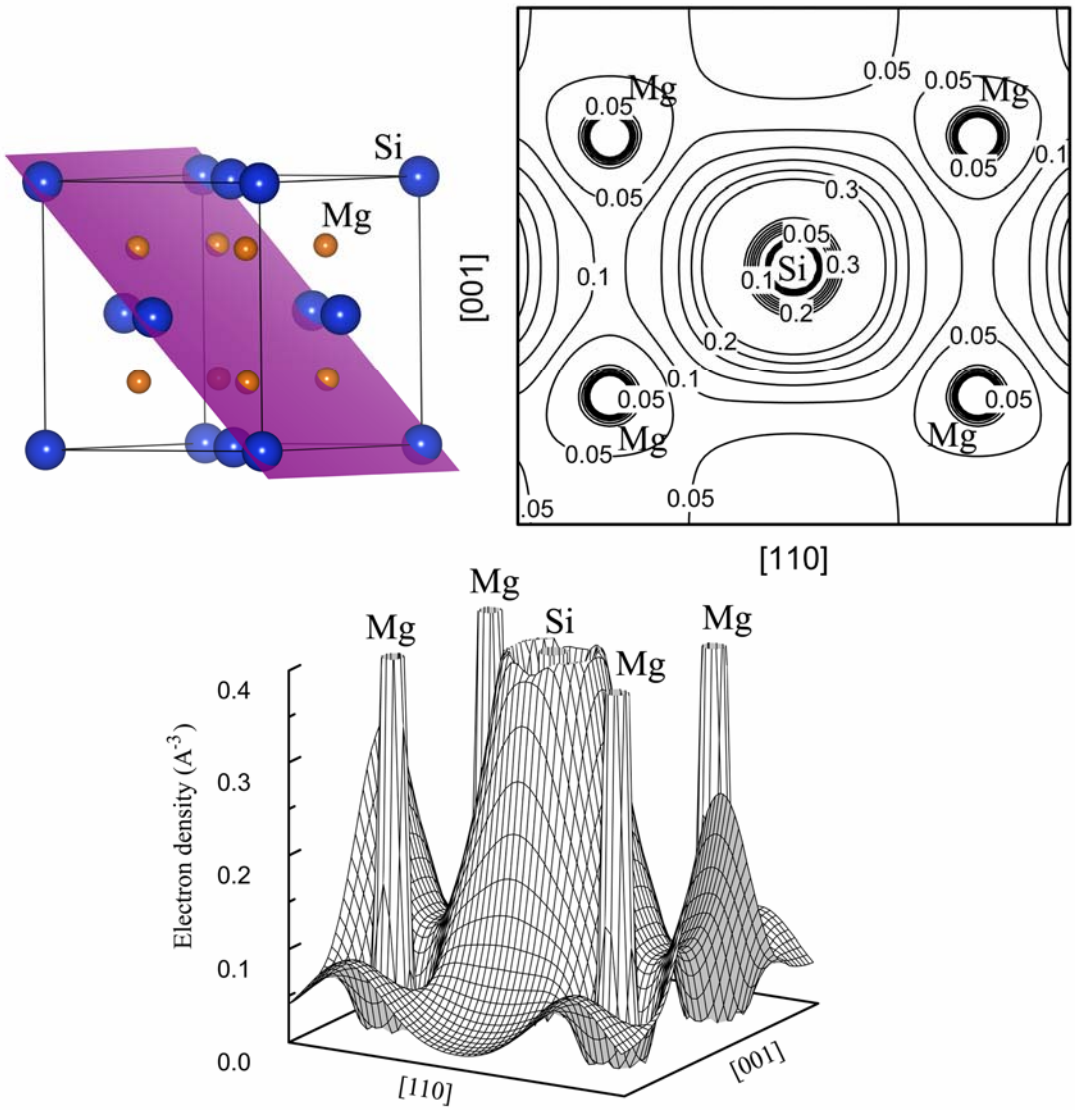

Fig. 5.6 The calculated 2-D and 3-D valence electron density of Mg_2Si on {110} type plane. The corresponding lattice plane is shown.

In Fig. 5.6, the electron density decreases monotonically from Si toward Mg and reaches a minimum closely surrounding Mg. The outer contour around Si has a pseudohexagonal distortion from spherical symmetry. The vertexes of the contour point to <110> type directions, indicating that the distortion is caused by the Si-Si covalent bonding.

In the region around the midpoint between Mg and Si, however, the contours stretch along <111> directions showing a slight rectangular distortion. This is a result of the polarization effect from the eight Mg ions surrounding the Si atom. These positively charged Mg ions attract the loose-bound electrons in Si outer orbitals leading to some covalency. Hence, we can conclude that the Mg-Si bond is largely ionic with small covalent character.

Table 5.2 Bader analysis of the number of electrons surrounding each atom

	Mg	O	Si
c-Si			14
MgO	10.28	9.72	
Mg_2Si	10.52		16.96

Charges associated with atoms in Mg_2Si, c-Si and MgO are obtained via Bader analysis and are presented in Table 5.2 for comparison. Si in c-Si has all 14 electrons bound to the nucleus because of the pure covalent Si-Si bonds. In MgO, 1.72 out of the 2 Mg 3s valence electrons are transferred to O, corresponding to an ionicity of 86%. This value is same as the results published by other groups [23, 24]. In Mg_2Si, each Mg atom donates 1.48 electrons to Si. The Mg-Si bond therefore has an ionic component of 74%. The remaining 0.52 Mg 3s valence electrons are shared with Si. It is worth noting that the ratio of the transferred charge in Mg_2Si and MgO is 1.48/1.72=0.86. This is reasonably close to the ratio of Mg 3s holes, 0.73, obtained from EELS measurements. Hence, the intensity of

the Mg $L_{2,3}$-edge is a useful tool to study the bonding nature of Mg-containing compounds, though the availability of quantitative information depends on the spectral resolution.

5.5 Conclusion

The nature of the Mg-Si bond in Mg_2Si was studied by both EELS measurements and theoretical calculations. The results are compared with those of MgO and crystalline Si. Plots of calculated electron density show that the Mg-Si is largely ionic in nature. A small covalent component is observed from the distortion of electron density contours, however. A charge transfer of 1.48 electrons per Mg atom is found out via Bader analysis. A comparison between the EELS data and the calculational results shows that the intensity of Mg $L_{2,3}$-edge is indicative of Mg 3s occupancy.

References

[1] Fauteux, D.; Koksbang, R. *J. Appl. Electrochem.* 1993, 23, 1.

[2] Vaughey, J. T.; Kepler, K. D.; Benedek, R.; Thackeray, M. M. *Electrochem. Commun.* 1999, 1, 517.

[3] Graetz, J.; Ahn, C. C.; Yazami, R.; Fultz, B. *J. Electrochem. Soc.* 2004, 151, A698.

[4] Graetz, J.; Ahn, C. C.; Yazami, R.; Fultz, B. *Electrochem. Solid State Lett.* 2003, 6, A194.

[5] Kim, H.; Choi, J.; Sohn, H. J.; Kang, T. *J. Electrochem. Soc.* 1999, 146, 4401.

[6] Huang, C. K.; Surampudi, S.; Attia, A. I.; Halpert, G. U. S. Pat. 1994, 5, 294, 503.

[7] Roberts, G. A.; Cairns, E. J.; Reimer, J. A. *J. Power Sources* 2002, 110, 424.

[8] Song, S. W.; Striebel, K. A.; Reade, R. P.; Roberts, G. A.; Cairns, E. J. *J. Electrochem. Soc.* 2003, 150, A121.

[9] Vajo, J. J.; Mertens, F.; Ahn, C. C.; Bowman, R. C.; Fultz, B. *J. Phys. Chem. B* 2004, 108, 13977.

[10] Baranek, P.; Schamps, J.; Noiret, I. *J. Phys. Chem. B* 1997, 101, 9147.

[11] McWilliams, D.; Lynch, D. W. *Phys. Rev.* 1963, 130, 2248.

[12] Eldridge, J. M.; Miller, E.; Komarek, K. L. *Trans. Metall. Soc.* 1967, 239, 775.

[13] Whitten, W. B.; Chung, P. L.; Danielson, G. C. *J. Phys. Chem. Solids* 1965, 26, 49.

[14] Meloni, F.; Mooser, E.; Baldereschi, A. *Physica* 1983, 117B&118B, 72.

[15] Bevolo, A. J.; Shanks, H. R. *J. Vac. Sci. Technol. A* 1983, 1, 574.

[16] van Buuren, M. R. J.; Voermans, F.; van Kempen, H. *J. Phys. Chem.* 1995, 99, 9519.

[17] Johnson, D. W.; Spence, J. C. H. *J. Phys. D* 1974, 7, 771.

[18] Egerton, R. F. *Electron Energy-Loss Spectroscopy in the Electron Microscope*; Plenum: New York, 1996.

[19] Blaha, P.; Schwarz, K.; Sorantin, P.; Trickey, S. B. *Comput. Phys. Commun.* 1990, 59, 399.

[20] Perdew, J. P.; Kurth, S.; Zupan, A.; Blaha, P. *Phys. Rev. Lett.* 1999, 82, 2544.

[21] Bader, R. F. W. *Atoms in Molecules: A Quantum Theory*; Oxford University Press: New York, 1994.

[22] Mizoguchi, T.; Tanaka, I.; Yoshiya, M.; Oba, F.; Ogasawara, K.; Adachi, H. *Phys. Rev. B* 2000, 61, 2180.

[23] Noguera, C.; Pojani, A.; Casek, P.; Finocchi, F. *Surf. Sci.* 2002, 245, 507.

[24] Uberuaga, B. P.; Smith, R.; Cleave, A. R.; Henkelman, G.; Grimes, R. W.; Voter, A. F.; Sickafus, K. E. *Phys. Rev. B* 2005, 71, 104102.

Chapter 6

Future Work

6.1 Electronic structure of CF_x

Carbon fluorides were first used as anode materials in primary lithium batteries in 1970 [1]. For graphite-based CF_x, the F atoms enter the graphene layers, and the periodicity of the new layered structure is determined by the F content [2, 3]. The structures of C_2F and CF prepared from graphite are shown in Fig. 6.1.

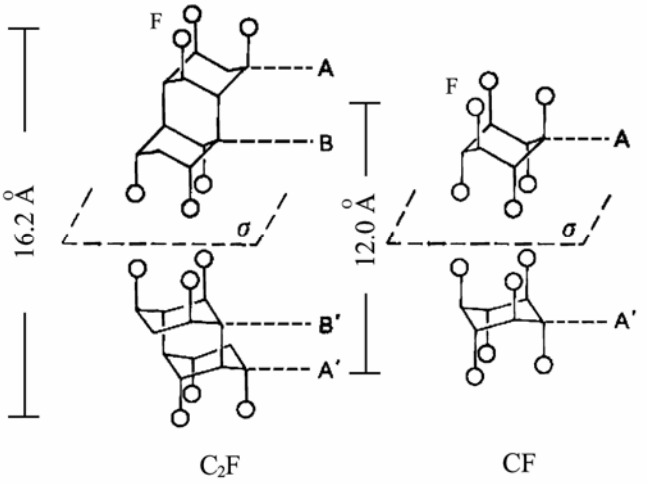

Fig. 6.1 The layered structure of C_2F and CF prepared by using graphite as precursor.

The C-C bonds in graphite are greatly modified by fluoridation as observed by EELS measurements (Fig. 6.2). The intercalation of F atoms breaks the σ-type C-C interlayer bonds and alters the hybridization of the valence states of C atoms from sp^2 to

sp^3. As a result, the σ^* peak increases at the expense of π^* peak with fluoridation. However, due to the diversity of the available carbonous precursors [4, 5], the crystallographic structure of CF_x can vary considerably, and details of bondings in those materials are unknown. The application of CF_x as an anode in battery is currently limited by its low electrical conductivity. A systematic study of the chemical bonds in CF_x prepared from various carbonous materials can provide a better understanding of the electronic structure which essentially determines the charge transportation mechanism, and therefore will be helpful to overcome this shortcoming.

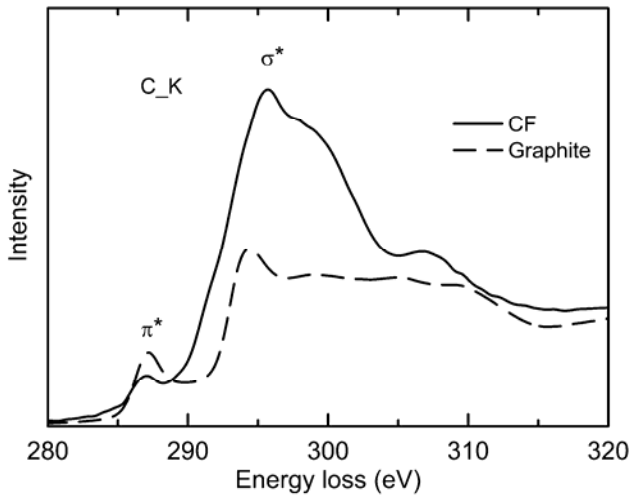

Fig. 6.2 The C K-edge of graphite-based CF and pristine graphite. The spectra are normalized with a 50 eV window 40 eV beyond the σ^* peak.

6.2 Phase distribution in cathode and anode materials

6.2.1 Introduction

The insertion and extraction of Li are diffusion controlled processes. A core-shell model has been proposed to describe the phase distribution [6]. In this model, the lithiated phase is surrounded by a shell of the delithiated phase during delithiation. However, high spatial resolution EELS study of $LiFePO_4$ showed that the diffusion might proceed from one side to the other side across the particle, instead of from the surface to the core [7]. Since the diffusion process is closely related to the crystallographic symmetry of the material, it is of interest to know how the lithiated and delithiated phases are distributed in those cathode and anode materials for Li-ion batteries with different structures. Two types of EELS-based techniques, as introduced in following sections, are available to accomplish this mission.

6.2.2 Elemental mapping

Elemental mapping by EELS can provide the two-dimensional distribution of a specific element in the sample, either via the spectrum imaging method or via the electron spectroscopic imaging method. The small atomic number ($Z = 3$) makes lithium very difficult to be detected by X-ray techniques. However, lithium can be readily detected in EELS because of its strong K-edge around 55 eV.

The spectrum imaging method rasters the electron beam across the specimen and records an EELS spectrum at every point. The corresponding ionization edge in each spectrum is then quantified to construct a two-dimensional distribution of lithium, i.e., the distribution of the delithiated and lithiated phases. This method requires a very small beam probe size and is usually conducted on a scanning transmission electron microscope (STEM). In the electron spectroscopic imaging method, an energy-selecting slit is used to allow electrons only within a certain energy window, e.g., the Li K-edge, to be collected by the spectrometer, which is capable of producing a two-dimensional image. Hence, an image with contrast proportional to the concentration of the element is obtained. If a sufficiently fine spatial resolution is obtainable, the elemental mapping can even resolve the concentration gradient between the bulk and the grain boundaries which may be critical to the performance of nano-sized materials [8, 9]. An example of EELS elemental mapping is shown in Fig. 6.3 [10].

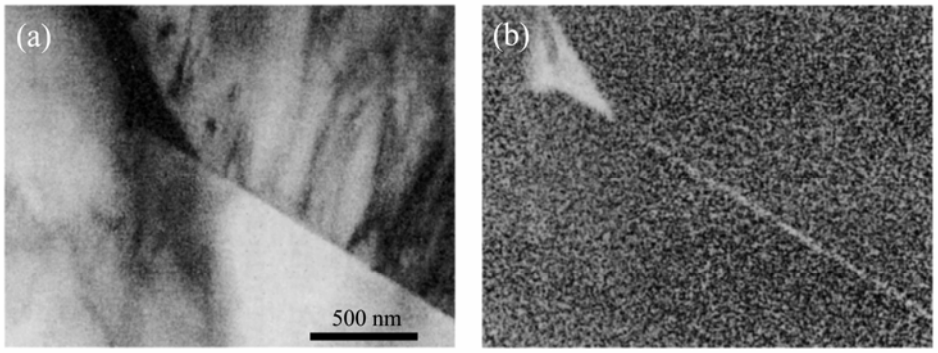

Fig. 6.3 (a) TEM bright field image of alumina with additions of barium silicate. (b) Elemental map using Ba $M_{4,5}$-edge shows the high concentration of Ba at grain boundary and triple pocket.

6.2.3 Valence electron density analysis

The strongest signal (except the ZLP) in an EELS spectrum is the plasmon peak, which originates from the resonant oscillation of the valence electron gas of the solid in response to the incident electron. Within the free-electron model, the plasmon energy, *Ep*, is expressed as

$$E_p = \frac{h}{2\pi}\left(\frac{Ne^2}{m\varepsilon_0}\right)^{\frac{1}{2}}, \tag{6.1}$$

where N is the valence electron density and m the rest mass of electron. In insulators and semiconductors where the valence electrons are no longer free, this expression can still be used by including a relaxation time

$$\tau = \frac{1}{\Gamma}\ , \tag{6.2}$$

where Γ is called the damping constant describing the damping of the plasmon oscillation. As the plasmon energy, and hence the plasmon peak, is sensitive to the valence electron density, any changes in this quantity (e.g. decrease due to lithium removal) can be detected from the shift of plasmon energy. Hence, analysis of the plasmon peak position can be used for phase identification. As it directly concerns the density of valence electrons, this technique will be particularly useful in studying the lithiation and delithiation processes during charging and discharging, where the charge density varies continuously. An

example of the application of this analysis in studying the Al-Li alloy is shown in Fig. 6.4 [11].

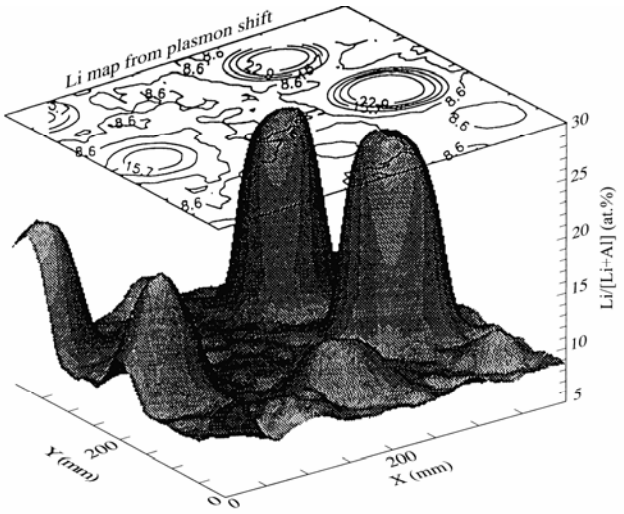

Fig. 6.4 Contour and surface plot of lithium concentration in an Al-10.5at% alloy determined by shifts in the plasmon peak position.

Reference

[1] Watanabe, N.; Fukuda, M. *U. S. Pat.* 1970, 3,536,532.

[2] Watanabe, N.; Nakajima, T.; Touhara, H. *Graphite Fluoride*; Elsevier: New York, 1988.

[3] Kita, Y.; Watanabe, N.; Fujii, Y. *J. Am. Chem. Soc.* 1979, 101, 3832.

[4] Li, J.; Naga, K.; Ohzawa, Y.; Nakajima, T.; Shames, A. I.; Panich, A. M. *J. Fluorine Chem.* 2005, 126, 265.

[5] Nakajima, T.; Touhara, H.; Okino, F. *Actual. Chimique* 2006, 119-122, 301.

[6] Padhi, A. K.; Nanjundaswamy, K. S.; Goodenough, J. B. *J. Electrochem. Soc.* 1997, 144, A1188.

[7] Laffont, L.; Delacourt, C.; Gibot, P.; Wu, M. Yue; Kooyman, P.; Masquelier, C.; Tarascon, J. M. *Chem. Mater.* 2006, 18, 5520.

[8] Graetz, J.; Ahn, C. C.; Yazami, R.; Fultz, B. *J. Electrochem. Soc.* 2004, 151, A698.

[9] Graetz, J.; Ahn, C. C.; Yazami, R.; Fultz, B. *Electrochem. Solid State Lett.* 2003, 6, A194.

[10] Brydson, R. *Electron Energy Loss Spectroscopy*; BIOS Scientific: Oxford, 2001.

[11] Disko, M. M.; Ahn, C. C.; Fultz, B. *TMS*: Warrendale, 1992.

Appendix I

Electron Density Plots for $LiFePO_4$ and $FePO_4$

Distributions of valence electrons (Li 2s, Fe 3d and 4s, P 3s and 3p and O 2p) for $LiFePO_4$ and $FePO_4$ are obtained by using WIEN2K code. The atomic coordinates are same as those used in the VASP calculations in chapter 4. Fig. I.1 shows the plots of the electron densities on the {010}-type lattice plane cutting through (0, 1/4, 0) for $LiFePO_4$ and $FePO_4$, respectively. The vertices of the contours of Fe atoms extend to O atoms after delithiation, indicating more covalent Fe-O bonds. The outer contours surrounding both Fe and O atoms also increase slightly in their intensities. There are atomic displacements of the PO_4^{3-} polyanion, but the contours surrounding P atoms do not show observable changes. Fig. I.2 shows the plots of the electron densities on the (110) lattice plane. O_1 and O_3 are O atoms occupying inequivalent crystallographic sites, which are slightly out of the plane. The O_1 atoms move closer to the plane after delithiation, hence cause a seeming increase in the associated electron density. The vertices of contours surrounding Fe atoms and the outer contours surrounding O atoms show behaviors similar to those in Fig. I.1. In Fig. I.3, the plots of the electron densities on the $\{01\bar{1}\}$-type lattice plane do not show significant

difference between $LiFePO_4$ and $FePO_4$, indicating the delithiation has little effects on the O-O bonds. These plots of electron densities confirm our conclusions drawn from the EELS measurements and the VASP calculations — there is no charge transfer from P atoms during delithiation, and Fe and O atoms both make contributions to the charge compensation. The O atoms are more covalently bonded in $FePO_4$ than in $LiFePO_4$.

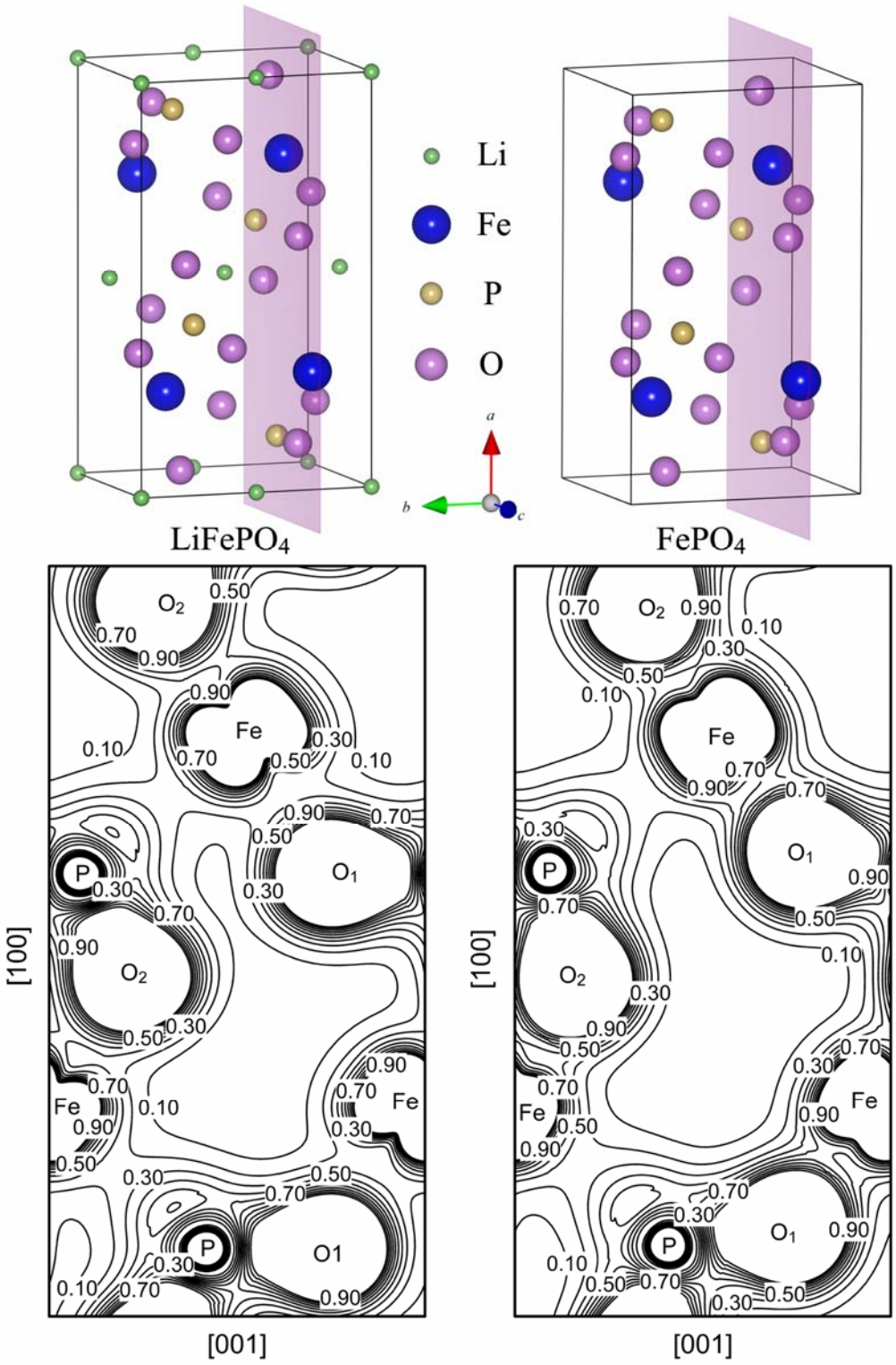

Fig. I.1 Electron densities on the {010}-type lattice plane cutting through (0, 1/4, 0) for $LiFePO_4$ and $FePO_4$, respectively.

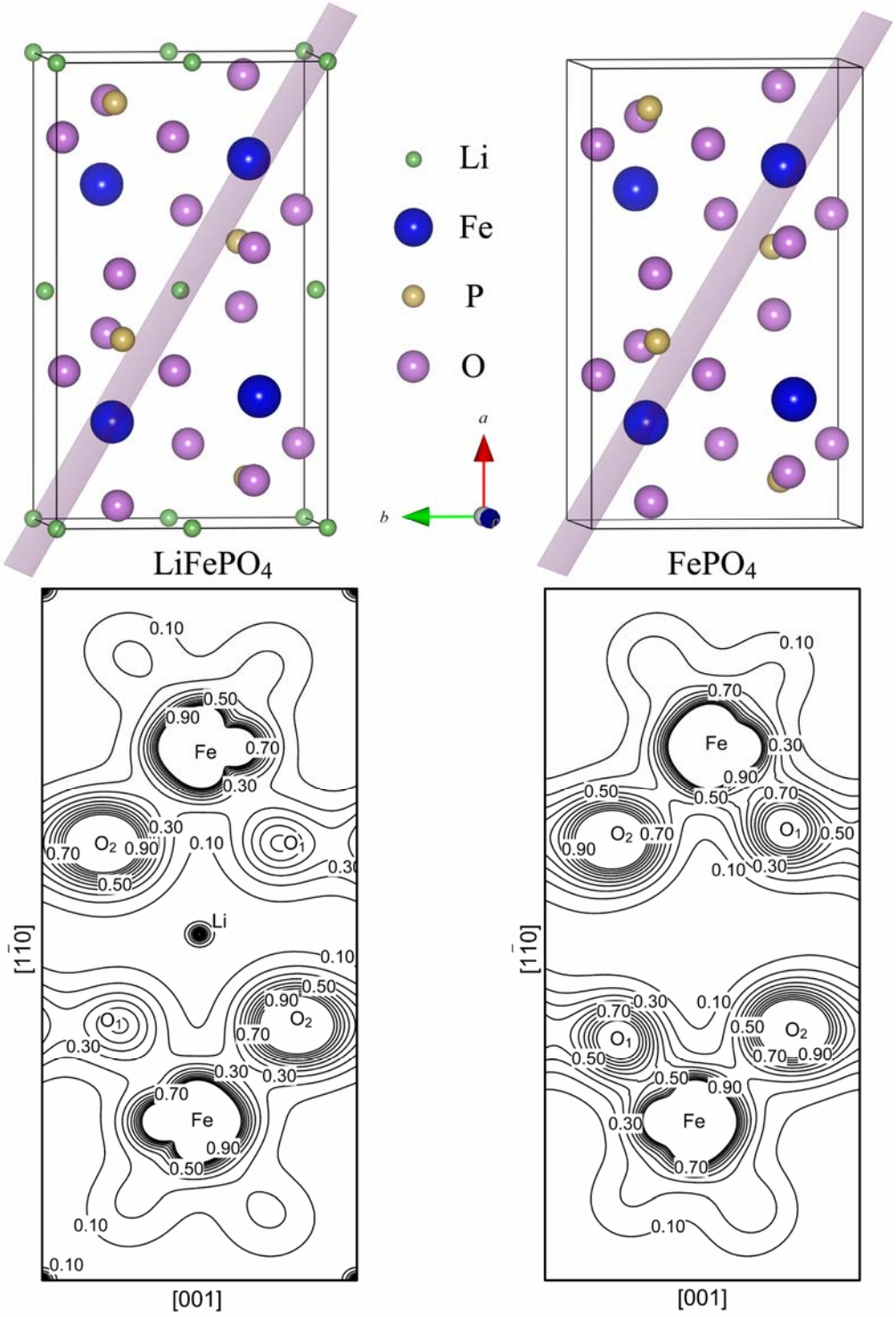

Fig. I.2 Electron densities on the (110) lattice plane for $LiFePO_4$ and $FePO_4$, respectively.

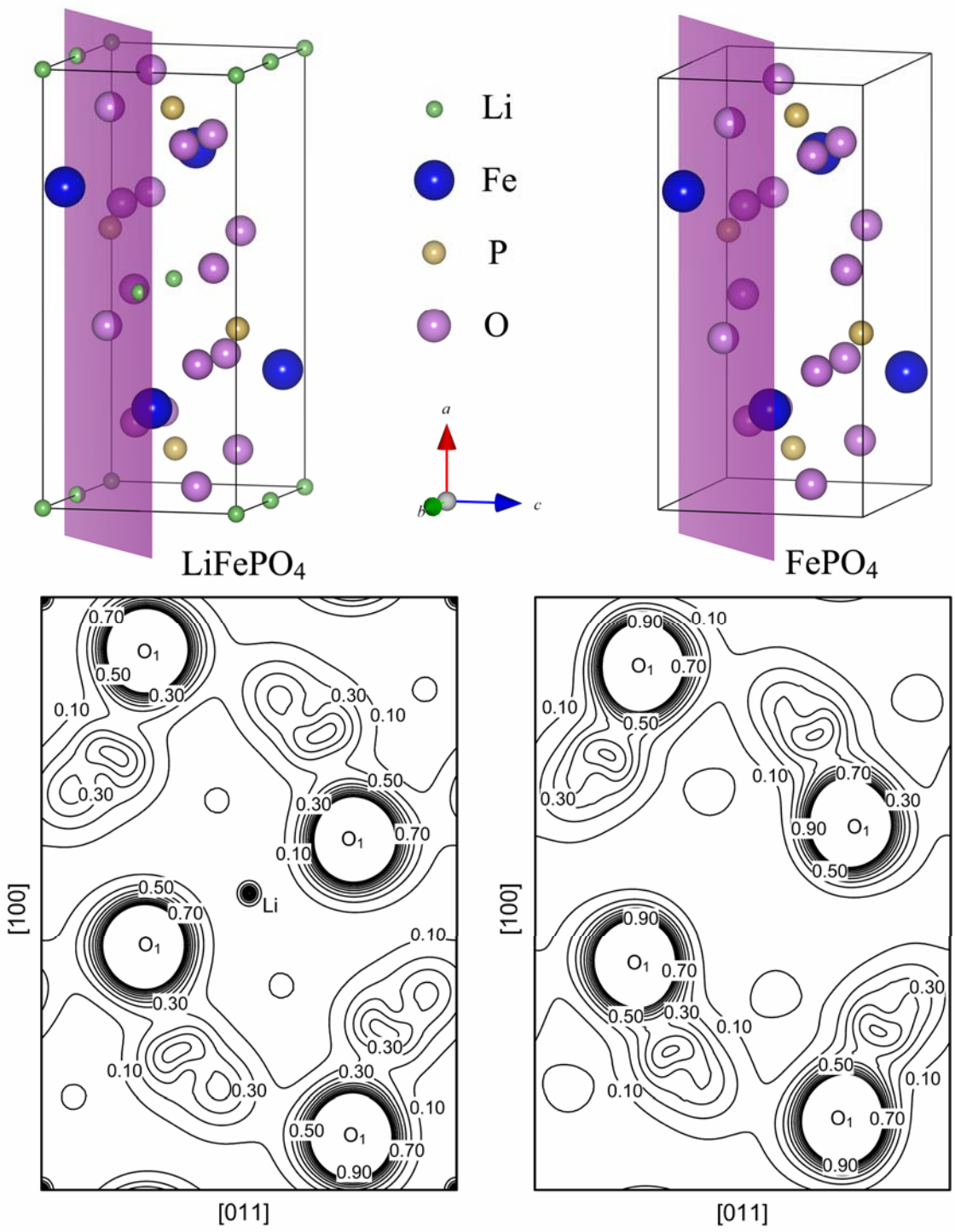

Fig. I.3 Electron densities on the $\{01\bar{1}\}$-type lattice plane cutting through (0, 1/2, 0) for $LiFePO_4$ and $FePO_4$, respectively.